REPORT DOCUMENTATION PAGE

Form Approved
OMB No. 0704-0188

1. REPORT DATE *(DD-MM-YYYY)*	2. REPORT TYPE	3. DATES COVERED *(From - To)*
19-07-2019	Final Technical	01/01/2016 - 12/31/2018

4. TITLE AND SUBTITLE
Electrolyte Materials and Physical Chemistry for Electrochemical Devices

5a. CONTRACT NUMBER
N00014-16-1-2095

5b. GRANT NUMBER

5c. PROGRAM ELEMENT NUMBER

6. AUTHOR(S)
Dr. Thomas Zawodzinski

5d. PROJECT NUMBER

5e. TASK NUMBER

5f. WORK UNIT NUMBER

7. PERFORMING ORGANIZATION NAME(S) AND ADDRESS(ES)
The University of Tennessee
1331 Circle Park Dr.
Knoxville, TN 37916-3801

8. PERFORMING ORGANIZATION REPORT NUMBER

9. SPONSORING/MONITORING AGENCY NAME(S) AND ADDRESS(ES)
ONR NAVAL MATERIALS DIV
875 N. Randolph Street
Arlington VA 22203-1995

10. SPONSOR/MONITOR'S ACRONYM(S)
ONR

11. SPONSOR/MONITOR'S REPORT NUMBER(S)

12. DISTRIBUTION/AVAILABILITY STATEMENT
Approved for Public Release; Distribution is Unlimited

13. SUPPLEMENTARY NOTES

14. ABSTRACT
In this effort, we studied several series of electrolyte materials, including preparing several new conductors. While emphasizing the electrolyte behavior, we probed the physical chemistry and transport in several types of systems (polymer/ concentrated electrolyte, organic proton conductors, composite electrodes). Our electrode work also continued some activity aimed at using electroactive mediators present in the electrolyte to explore the possibility of carrying out mediated oxidation of bio-derived materials to liberate hydrogen. This work results in a collection of data on the behavior of electrolytes of substantial scope, leading to the development of n

15. SUBJECT TERMS
Energy Storage, Redox Flow Battery, Fuel Cell Electrodes, Solid Acid Fuel Cells, Redox Mediators

16. SECURITY CLASSIFICATION OF:			17. LIMITATION OF ABSTRACT	18. NUMBER OF PAGES	19a. NAME OF RESPONSIBLE PERSON
a. REPORT	b. ABSTRACT	c. THIS PAGE			Dr. Thomas Zawodzinski
U	U	U	UU	126	19b. TELEPHONE NUMBER *(Include area code)* 865-974-2421 974 5137

INSTRUCTIONS FOR COMPLETING SF 298

1. REPORT DATE. Full publication date, including day, month, if available. Must cite at least the year and be Year 2000 compliant, e.g. 30-06-1998; xx-06-1998; xx-xx-1998.

2. REPORT TYPE. State the type of report, such as final, technical, interim, memorandum, master's thesis, progress, quarterly, research, special, group study, etc.

3. DATE COVERED. Indicate the time during which the work was performed and the report was written, e.g., Jun 1997 - Jun 1998; 1-10 Jun 1996; May - Nov 1998; Nov 1998.

4. TITLE. Enter title and subtitle with volume number and part number, if applicable. On classified documents, enter the title classification in parentheses.

5a. CONTRACT NUMBER. Enter all contract numbers as they appear in the report, e.g. F33315-86-C-5169.

5b. GRANT NUMBER. Enter all grant numbers as they appear in the report. e.g. AFOSR-82-1234.

5c. PROGRAM ELEMENT NUMBER. Enter all program element numbers as they appear in the report, e.g. 61101A.

5e. TASK NUMBER. Enter all task numbers as they appear in the report, e.g. 05; RF0330201; T4112.

5f. WORK UNIT NUMBER. Enter all work unit numbers as they appear in the report, e.g. 001; AFAPL30480105.

6. AUTHOR(S). Enter name(s) of person(s) responsible for writing the report, performing the research, or credited with the content of the report. The form of entry is the last name, first name, middle initial, and additional qualifiers separated by commas, e.g. Smith, Richard, J, Jr.

7. PERFORMING ORGANIZATION NAME(S) AND ADDRESS(ES). Self-explanatory.

8. PERFORMING ORGANIZATION REPORT NUMBER. Enter all unique alphanumeric report numbers assigned by the performing organization, e.g. BRL-1234; AFWL-TR-85-4017-Vol-21-PT-2.

9. SPONSORING/MONITORING AGENCY NAME(S) AND ADDRESS(ES). Enter the name and address of the organization(s) financially responsible for and monitoring the work.

10. SPONSOR/MONITOR'S ACRONYM(S). Enter, if available, e.g. BRL, ARDEC, NADC.

11. SPONSOR/MONITOR'S REPORT NUMBER(S). Enter report number as assigned by the sponsoring/ monitoring agency, if available, e.g. BRL-TR-829; -215.

12. DISTRIBUTION/AVAILABILITY STATEMENT. Use agency-mandated availability statements to indicate the public availability or distribution limitations of the report. If additional limitations/ restrictions or special markings are indicated, follow agency authorization procedures, e.g. RD/FRD, PROPIN, ITAR, etc. Include copyright information.

13. SUPPLEMENTARY NOTES. Enter information not included elsewhere such as: prepared in cooperation with; translation of; report supersedes; old edition number, etc.

14. ABSTRACT. A brief (approximately 200 words) factual summary of the most significant information.

15. SUBJECT TERMS. Key words or phrases identifying major concepts in the report.

16. SECURITY CLASSIFICATION. Enter security classification in accordance with security classification regulations, e.g. U, C, S, etc. If this form contains classified information, stamp classification level on the top and bottom of this page.

17. LIMITATION OF ABSTRACT. This block must be completed to assign a distribution limitation to the abstract. Enter UU (Unclassified Unlimited) or SAR (Same as Report). An entry in this block is necessary if the abstract is to be limited.

Final Report for N00014-16-1-2095.

PI: Thomas Zawodzinski, University of Tennessee-Knoxville

Electrolyte Materials and Physical Chemistry for Electrochemical Devices

Overview

In this effort, we studied several series of electrolyte materials, including preparing several new conductors. While emphasizing the electrolyte behavior, we probed the physical chemistry and transport in several types of systems (polymer/concentrated electrolyte, organic proton conductors, composite electrodes). Our electrode work also continued some activity aimed at using electroactive mediators present in the electrolyte to explore the possibility of carrying out mediated oxidation of bio-derived materials to liberate hydrogen.

This work results in a collection of data on the behavior of electrolytes of substantial scope, leading to the development of new understanding in an area of physical chemistry that was previously neglected.

Accomplishments

Membranes and Separators

Key targets for improvement of membranes for RFB applications are the membrane resistance and reagent cross-over. We addressed these aspects by building our fundamental understanding of membrane behavior and by developing a database of membrane operational properties, including the testing and deployment of new membrane materials. We developed a new theoretical framework for the interpretation of fundamental electrolyte uptake behavior for membranes exposed to bathing solutions of high concentration. We studied both anion and cation conducting membranes from external sources and via our own internal preparation. Both perfluorinated and hydrocarbon ion exchange materials were studied, as will our cross-linked gels.

Experimental Physical Chemistry

Perhaps the most important limitation in flow batteries is the tendency of ions and water to be transported across the membrane or separator. Our work has focused on the underlying aspects of this process. Membranes for RFBs serve as one motivator for this type of work. We probed

chemistry of membranes in contact with solutions appropriate to a range of applications. Our goals are extending our knowledge of the behavior of membranes in these situations while also developing some physical generalizations to explain the observed behavior. Given the diversity of possible situations relevant to RFBs and other membrane applications, we studied several different situations, including equilibrated solutions ions other than protons and also concentrated solutions of acid with membranes. In the latter case, we sought to put the description of ion exchange membrane behavior on firm footing.

II.1 Physical Chemistry of Membranes in the Flow Battery Environment

In one study, we compared the behavior of ion exchange membranes loaded with potassium and sodium ions. Ion exchange membranes are in use in a range of situations in which they are exposed to solutions of electrolytes, sometimes quite concentrated solutions. Applications include a variety of electrochemical reactor systems employing continuous flow such as redox flow batteries, desalination units, electrosynthesis reactors and so on. These use several different types of membranes to maintain or achieve separation of incompatible solutions. The most widely used membranes, the perfluorinated sulfonic acid (PFSA) membranes employ perfluorinated backbones, which ensures good mechanical and chemical durability of the polymer structure, and sulfonate-terminated side chains with exchangeable counterions. Over the past few decades, the archetypal PFSA membrane, Nafion®, commercialized by Du Pont, has been extensively studied. In many applications, Nafion® exhibits excellent thermal and chemical stability[1], water management[2-4], as well as good ionic conductivity[5]. The hydrophilic sidechains with absorbed water form ion clusters and aggregates distributed through the whole polymer membranes. These hydrophilic clusters are phase-separated from fluorocarbon backbones and have estimated average diameters in the range of 30~50 Å for H^+ form Nafion®. The ion exchange character of the material promotes cation and water uptake and transfer across the membrane but hinders the transport of anions[6].

The most intensively analyzed application of PFSA membrane is in fuel cells, in which the polymer membranes functions as a separator for reactants H_2 and O_2 and as an electrolyte allowing H^+ ion transport through the membrane to accomplish electrochemical reaction[7]. Therefore, the studies have been primarily focused on the H^+ form PFSA membranes[8-15]. As emphasis on other electrochemical applications such as redox flow batteries[16, 17], desalination[18] or electrochemical reactors[19] increases in response to the availability of

'renewable electrons' on the grid, it is important to take account of membrane behavior at a broader and deeper level than previously studied[20, 21]. With this wider array of devices, we are beginning to focus more intently on the behavior of cations other than protons. In the following, we discuss behavior in several different PFSAs. We add literature conclusions regarding some other membranes, but the discussion is dominated by results from studies of Nafion®.

Among important situations to consider are those in which multiple ions are present. This situation might occur in membrane processes, for example, involving natural waters in contact with membranes used in wastewater treatment and desalination processes or in membranes in redox flow batteries in contact with electrolytes in which multiple cations are present. In such cases, membranes interact with multiple cations, possibly with various valence states. Partitioning of ions, such as alkali metal, alkaline earth metal and quaternary ammonium ions, into the Nafion® perfluorosulfonate membrane was studied extensively by Pintauro, Yeager and others[22-30]. Yeager[26] found that the cations with smaller hydration energies release more energy from electrostatic interactions, thereby driving preferential interactions with the sulfonate side chains and exchange into polymer membranes. The order of ionic selectivity for univalent ions is $Cs^+>Rb^+>Tl^+>K^+>Na^+>Ag^+>Li^+$; the order for some divalent ions is $Ba^{2+}>Sr^{2+}>Ca^{2+}>Ma^{2+}>Co^{2+}>Zn^{2+}$[26]. In addition, selectivity between the univalent and bivalent ions has also been investigated[23, 27, 28]. Selectivity is in the same order as in univalent mixtures. The divalent cation concentration absorption does not follow a size-dependent absorption sequence, but it is a function of the type and membrane phase concentration of co-absorbed monovalent ions[23]. For example, between 10% and 85% of the sulfonate exchange sites are found to be neutralized by bound Pb^{2+} or Cd^{2+}, with the extent of binding increasing with the surface charge density of co-absorbed univalent cations and decreasing with increasing of total external salt concentration[27].

The transport of water and charger carriers in PFSA membrane is technically important since the current through the device employing polymer membranes depends on these parameters. Understanding transport of cations and water in the membrane may give insight into some practical problems in devices. Multiple factors contribute to the observed transport properties. Intrinsic cation mobility differences, driven by size and valence effects are of course important. Water uptake is variable in different ionic forms and low water uptake in the membrane results in

increasing ionic resistance in a device since the ionic conductivity of polymer membrane dramatically decreases when the membrane water is low. There is some literature focusing on the study of water uptake, ion and water transport of the non-H^+ form Nafion®. The water uptake λ, i.e. the number of water molecules per sulfonate ion exchange site, usually decreases with increasing radius of univalent counterions in the membrane or decreasing of hydration energy. The only exception is: in some report[31-34], the water uptake of Li^+ form Nafion® is comparable to the one of H^+ form Nafion® at higher water activity but lower at low water activity due to the small effect of cationic interactions while the membrane equilibrated at high water activity environment (>0.7). The λ of sodium ion form Nafion® 120 is 11.9, while the cesium ion form has a water uptake of 6.6[35]. In another report[2], H^+ form Nafion® 117 showed the highest water uptake, 19.5 wt%, compared with membranes exchanged with other univalent ions such as Li^+, Na^+, K^+, Rb^+. The Rb^+ form Nafion® 117 has only 6.3 wt% water uptake. Divalent ions, such as Mg^{2+}, Ca^{2+}, Sr^{2+} and Ba^{2+}, Nafion® 117 typically have 15 wt% water uptake.

The effect of the cations themselves on conductivity is also a critical factor in which we are interested. As reported by Hongsirikarn et al.[36], the Na^+, Ca^{2+} and Fe^{3+} form Nafion® 211 membrane have very similar conductivity under similar conditions, i.e. in deionized water at 25°C or in the gas phase at 80°C, but slightly lower conductivity than the NH_4^+ form membrane. The conductivity of H^+ form Nafion® 211 membrane is more than 12 times higher than metal ion form membranes at 25°C in deionized water, and 6 times and 125 times greater in the gas phase at 100% RH or at 20% RH, 80°C[36].

Volkov et al.[37] reported some conductivity data for alkali metal form perfluorinated sulfocation membrane MF-4SC membrane. The fully hydrated MF-4SC has a conductivity of 0.028 S cm^{-1} for H^+ form membrane with λ=15.8, 0.0061 S cm^{-1} for Li^+ form membrane with λ=13.3, 0.0062 S cm^{-1} for Na^+ form membrane with λ=9.2 and 0.0003 S cm^{-1} for Cs^+ form membrane with λ=9.7. Even though it contains much less water than a Li^+ form membrane, the Na^+ form membrane still shows a slightly higher conductivity. When compared to Cs^+ form membrane, the Na^+ form membrane exhibits lower water uptake but much higher conductivity. These data show that water uptake and ionic conductivity of alkali metal form MF-4SC do not follow a simple sequence of water uptake as a function of ion diameter.

The apparent water diffusion coefficient in PFSA membranes also changes with the cation form. As reported by Yeager and co-workers, Na^+, K^+ and Cs^+ form Nafion® 120 show a water diffusion coefficient of 2.65×10^{-10} m^2 s^{-1}, 2.15×10^{-10} m^2 s^{-1} and 1.32×10^{-11} m^2 s^{-1} respectively, while the membranes were equilibrated in liquid water at 25°C[35]. When the Nafion® 115 is fully hydrated at 25°C, the water diffusion coefficient of H^+ form membrane is about twice of the value in Na^+ form membrane but only about 1/3 of the value in bulk water[38]. Again, both cation properties and total water uptake affect these values.

For both competitive partitioning and transport, all of the aforementioned studies were carried under conditions of complete hydration, i.e. with the membrane exposed to liquid water at near unity activity (on a mole fraction basis). However, the use of these materials in many applications entails a regime that is quite different from this simple case. The behavior of membranes in contact with concentrated solutions of salts is not widely reported. We have begun a program of systematic study of such situations, focusing to date on the vanadium redox flow battery[39]. The water and ion uptake and transport in the membrane-concentrated electrolyte system is significantly more complex than that of a simple one for one ion exchange situation studied above. The water content of membranes under such circumstances can be significantly lower than it is in the absence of imbibed salt and high water activity. It is therefore important to assess aspects of the behavior as a function of water content as a baseline for such studies.

Over the course of several decades, the materials used as cation exchange membranes have evolved since the early work on exchanged Nafion®. As we embark on the study of multiple situations with different membranes and ions, we need to establish similarities and differences between Nafion® and other PFSAs. PFSA membranes studied in this work are the 3M ionomer, which is a PFSA polymer membrane with equivalent weight (EW) 825. Similar to Nafion®, the 3M PFSA membrane also contains fluorocarbon backbones and sulfonate exchange sites but the sidechain structure is different, leading to different properties[15, 40, 41].

In this work, we present a study of the partitioning and transport of simple monovalent cations K^+ and Na^+ for membranes in various hydration states by contact with the vapor phase of different LiCl solutions. The latter allows us to understand some of the implications of lowered water content on ions in membranes. Cases in which only one ion is present and those in which there is a mixture of ions are both of interest since these ions are the most common cations used

in salts in various applications. We describe the water uptake, conductivity and water transport in membranes which we have exposed to KOH/NaOH solutions containing different mole fractions of the ions. We report the morphology difference between K^+ form and Na^+ form membranes by transmission electron microscopy (TEM). Fourier transform infrared spectroscopy (FT-IR) was applied to analyze the interactions between cation, sulfonate and water molecules in the membranes. The information obtained from these studies helps to better understand the fundamental properties of alkali metal form membranes and provides guidance for the application of PFSA membranes in electrochemical devices. One important finding is that the simple interpretation of the ion interactions in terms of a single parameter (ion hydration energy) only tells part of the story.

The water uptake, density and conductivity of membranes were determined at various hydration states of K^+, Na^+ and K^+/Na^+ mixed form perfluorosulfonate membranes. Water uptake decreases with increasing K^+ content in the membrane, consistent with increasing average cation size and decreasing hydration energy. However, for membranes at the same water content, the conductivity *increased* with increasing K^+ fraction, in spite of the fact that the size of K^+ is larger than that of Na^+. Analysis of data on the basis of percentage conducting volume reveals that the membranes with higher K^+ content show a much higher conductivity (with higher cation mobility) at percentage conducting volumes higher than 10%. One reason for this behavior may be due to a higher extent of dissociation for K^+ from the fixed anion site. TEM results show a larger cluster size in K^+ form membranes, another possible reason for faster K^+ transport. Pulsed field gradient (PFG) Nuclear Magnetic Resonance (NMR) shows that the water diffusion coefficient in the membranes with higher K^+ fraction is higher than for samples with lower K^+ fraction. FT-IR bands shift with the change of cation content, supporting the suggestion of a higher degree of cation-sulfonate dissociation and weaker hydrogen bonding interactions between cation and water molecules for membranes with higher K^+ content.

The water uptake by PFSA membranes is plotted as a function of water vapor activity in Figure 1. The typical error of repeat water uptake measurements is within $\pm$ 0.7 in the worst case. The error bars for data for a Na^+ form membrane is plotted in the figure as an example. As expected, the water uptake of K^+ and Na^+ form membranes is much less than the one of H^+ form membrane, and it decreases as the water vapor activity is decreased from 1 to 0.14. Generally, the water uptake of the membranes equilibrated at the same water vapor activity decreases with

the increase of K^+ content in the membranes. The sorption isotherms of Na^+ form membrane show a slight difference in shape relative to the other membranes, with a somewhat flatter rise in the curve between a_w of 0.6 to 0.8. We believe the disparity of sorption isotherms simply reflects measurement variance for the pure sodium form behavior. Following Yeager, we suggest that the lower water uptake by membranes with K^+ and Na^+ may be due to a smaller extent of ionic hydration (hydration energy: K^+: -348.53 kJ mol^{-1}; Na^+: -428.02 kJ mol^{-1}), and lower swelling due to increases in Young's modulus upon ion exchange [33]. Compared to the H^+ form 3M825 PFSA membrane with highest water uptake $\lambda \approx 14$ at $a_w=1$[42] the K^+ form, Na^+ form and K^+/Na^+ mixed form membranes show much lower water uptake. Again, this is because of the much smaller hydration energy for the K^+ and Na^+ forms than for the H^+ form membrane[46]. We have observed similar trends for many different cation-form membranes[42]. The maximum water uptake drops from 6.9 for Na^+ form membrane to 3.0 for K^+ form membrane, while the three mixed form membranes have λ = 5.9, 5.4 and 5.1 respectively, as the K^+ content increases in the membranes at $a_w=1$. Again, the decrease in water uptake as K^+ content increases is explained by the hydration energy of cation. As reported previously, the amount of loosely bound water in the high a_w region in the PFSA membrane dramatically decreases with the decrease in the hydration energy of the cation[46, 47] since the driving force for water uptake is significantly provided by cation hydration.

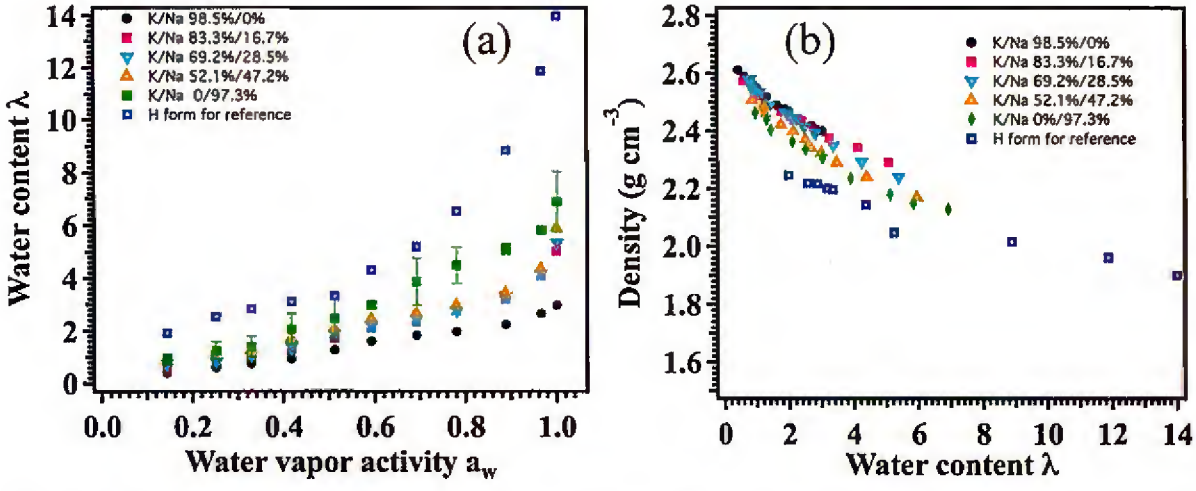

Figure 1. (a) Water uptake of 3M PFSA membranes as a function of water vapor activity a_w at 25 °C; (b) Density of 3M PFSA membranes as a function of water content at 25 °C.

The density of membrane was measured after the membrane was equilibrated at different water vapor activity and the results are shown in Figure 1(b). The density decreases as the water uptake

increases, which has been observed for H^+, Li^+, NH_4^+ and TEA^+ forms 3M membrane[42]. This is attributed to membrane swelling after the absorption of water and the addition of less dense water into the more dense PFSA membrane. Membrane densities varies between 2.12 g cm^{-3} and 2.62 g cm^{-3}. It appears that the membranes with higher K^+ content show a slightly higher density when compared at the same water content, and the density of all alkali metal form membrane in this report is about 10% higher than the one of H^+ form membrane. The most likely reason for the discrepancy is the weight difference of cations in these membranes, i.e. $EW_{K^+} > EW_{Na^+} > EW_{H^+}$[48-51].

The membrane conductivity data measured for various membranes with different cation content is plotted versus the water content λ in Figure 2(a). The membrane conductivity increases as the K^+ percentage increases at the same water content. Even though the highest water uptake of K^+ form membrane (K^+/Na^+ 98.5%/0%) is only about 3, its conductivity is as high as 0.031 S cm^{-1}. The Na^+ form membrane (K^+/Na^+ 0%/97.3%) with the highest water uptake λ=6.9 only show a conductivity of 0.021 S cm^{-1}. Some aspects of all PFSA-type membranes are conserved. Similar results of higher conductivity for membranes with larger cations and less water uptake was reported previously. Volkov, et al[37] described a perfluorinated sulfocation membrane MF-4SC and a perfluorocarboxylate membrane F-4CF prepared in H^+, Li^+, Na^+, K^+ and Cs^+ forms. The order of water uptake of F-4CF is $H^+>Li^+>Na^+>Cs^+$, which follows the opposite order of their ionic size, but the order of the conductivity for sulfonated MF-4SC membrane is $H^+>Na^+>Li^+>Cs^+$. For the F-4CF membrane, except for their finding that H^+ form membrane shows a smallest water uptake, the other three cation forms follow the same trend as the MF-4SC membrane for water uptake, and the order of conductivity for them is $Cs^+>Na^+>Li^+>H^+$ at the same water uptake. Moreover, their fully hydrated polymers show conductivity in the order as $K^+\approx Na^+>Li^+$ for similar sulfonate group concentration/ion exchange capacity[37].

The molar conductivity of these PFSA membrane electrolytes can provide some insight into the behavior of the ions. The molar conductivity normalizes the ionic conductivity by the total salt concentration in the polymer membranes. Generally, more dilute electrolytes have higher molar conductivity, reflecting the increased tendency toward ion pairing and aggregation as concentration increases. The molar conductivity increases slowly with dilution and approaches a limiting value as the concentration of electrolyte approaches zero. The molar conductivity of

weak electrolytes (incompletely dissociated) depends more strongly on concentration. The molar conductivity of K^+ and Na^+ form membranes was calculated using Equation 4.

$$\Lambda_M = \frac{1000*\sigma}{C} \qquad (4)$$

Where C (in units of mol L^{-1}) is the concentration of charge carrier in the PFSA polymer membranes.

Following some of our recent analyses, the definition of C here has possible two forms. First, the concentration C can be considered as the cation concentration in the whole membrane + water system. In this case, the cation concentration in membrane basis C_{m+w} can be calculated from Equation 5:

$$C_{m+w} = \frac{n_{cation}}{V_{m+w}} = \frac{1}{\frac{MW_m + \lambda * MW_w}{\rho_{m+w}}} \qquad (5)$$

Where ρ_{m+w} is the hydrated membrane density that we measured through pyconometry; MW_m is the equivalent weight of ionomer, n_{cation} is the number of moles of cations. For 1 unit of hydrated membrane, the mass is the sum of MW_m and associated water; MW_w is the molar mass of water.

For a second possible definition, the concentration C is calculated as the cation concentration in the water phase of PFSA membrane, C_w.

$$C_w = \frac{n_{cation}}{V_w} = \frac{1}{\frac{\lambda * MW_w}{\rho_w}} \qquad (6)$$

At high water content, water molecules solvate the cation and promote the dissociation of cation-sulfonate groups, decreasing the influence of the bound sulfonates on cation transport. These cations move through water in the polymer as if they are moving in a liquid environment[52]. Therefore the cation concentration in the water phase alone might be considered. In two previous papers[52, 53], we investigated the transition from membrane basis and water basis by discussing the applicability of Nernst-Einstein equation using the cation diffusion coefficient data and conductivity data for NH_4^+ form and Li^+ form PFSA membrane[52] and by carrying out a similar analysis in an AEM for bicarbonate[53]. Frankly, in this work, we are not able to give a clear interpretation about how to choose the basis for the concentration discussion due to the difficulty of measuring K^+ or Na^+ diffusivity. Therefore, we calculated molar conductivity using both C_{m+w} and C_m. This discussion will be mainly focused on the comparison of the transport properties of K^+ form and Na^+ form. The molar conductivity data calculated from Equation 4-6 is

plotted in Figure 2(b). As shown in Figure 2(b), the molar conductivity of K^+ form membrane decreases from 11.0 S cm^2 mol^{-1} to 0.007 S cm^2 mol^{-1} as the concentration increases, while that of Na^+ form membrane decreases from 9.9 S cm^2 mol^{-1} to 0.001 S cm^2 mol^{-1}. Regardless of whether we use the membrane basis or the water basis, the molar conductivity of K^+ form membrane is higher than that of Na^+ form membrane. The molar conductivity of both K^+ form and Na^+ form membrane dramatically decreases as the cation concentration increases, which evidences that these polymer membranes should be defined as weak electrolytes with partially dissociated K^+ and Na^+.

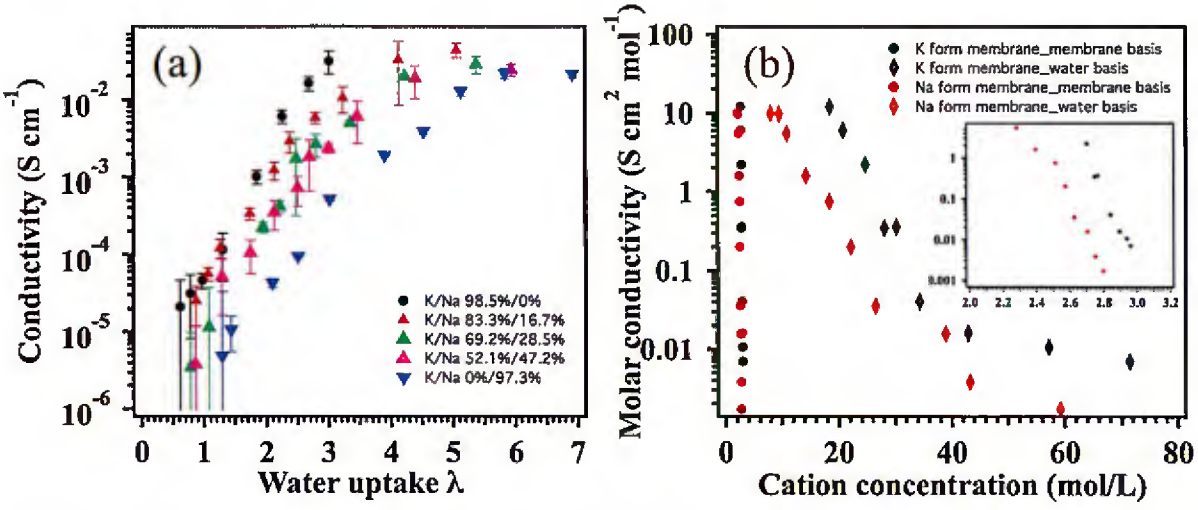

Figure 2 (a) Measured membranes conductivity as a function of water content; (b) The comparison of molar conductivity of K^+ and Na^+ in various environments (Insert: magnified figure of molar conductivity on the membrane basis of K^+ form and Na^+ form membrane).

Based on the PMV discussion, we are able to provide some discussion of volume-based parameters, such as percentage conducting volume (PCV). Actually, Kim and Pivovar [54, 55] reported the calculation of the PCV of PFSA membranes without taking into account the variation of $V_{PM,m}$ and $V_{PM,w}$ at various hydration states. Therefore, we introduced another expression for PCV' in Equation 7, which is a more appropriate method.

$$PCV' = \frac{V_{H_2O\ in\ the\ membrane}}{V_{Hydrated\ membrane}} = \frac{\lambda * V_{PM,w}}{V_{eq}} * 100\% \qquad (7)$$

The conductivity of these membranes increases significantly with the PCV' values and the K^+ form membrane shows a much *higher* conductivity than does the Na^+ form membrane. We suggest that at low water content, K^+ and Na^+ both associate with the sulfonate sites and are mostly not free for transport within the polymer membrane. At higher water content, K^+ ions,

with larger size and smaller surface charge density, exhibits a smaller electrostatic interaction with sulfonate groups, facilitating dissociation from fixed anions. The conductivity of the Na^+ form membrane starts to level off at PCV'>20%, which may be due to a dilution effect of the charge carriers at higher water uptake.

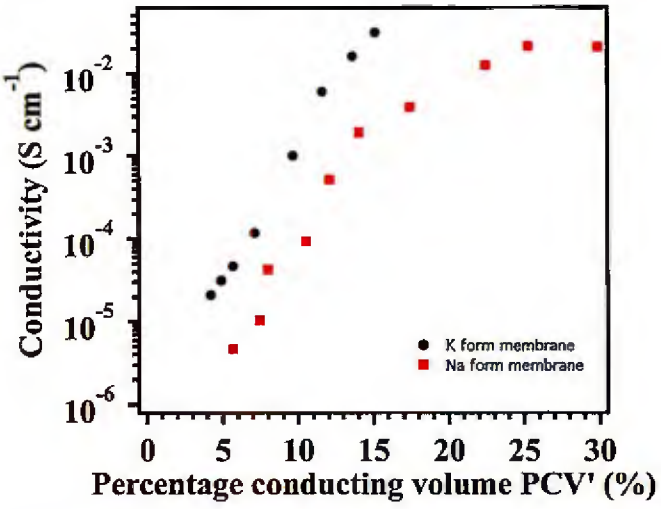

Figure 3. The conductivity of K^+ form and Na^+ form membrane as a function of percentage conducting volume PCV'.

The cation mobility in K^+ form and Na^+ form membranes was calculated using Equation 8.

$$u_{cation^+} = \frac{\sigma}{z_{cation^+} F C_{cation^+}} \quad (8)$$

Where σ is the membrane conductivity; z_{cation^+} is the valence of cation; F is the Faraday constant, 96500 C mol^{-1}, and $u_{cation^+}$is the mobility of cations in the membrane. Here, C_{cation^+} were also discussed in both membrane basis and water basis as shown above.

As shown in Figure 4(a), the K^+ and Na^+ mobility both show a range of mobility values of 10^{-4} to 10^{-9} cm^2 V^{-1} s^{-1} over the water uptake range, and the mobility dramatically decreases as the water content decreases. Comparing the mobility for the two types of membranes calculated using the two methods, i.e. a water basis and membrane basis, the K^+ mobility is always much higher than the Na^+ mobility when the membrane has similar water content. The results show higher ionic conductivity and cation mobility of K^+ form membrane than Na^+ form membrane when they are compared at the same water uptake level. As noted above, the higher mobility of K^+ can be ascribed to the cation-anion dissociation effect. The cation with larger radius has lower surface charge density and would be supposed to have weaker ion-ion interactions with sulfonate groups and a consequent higher cation-anion dissociation degree. Therefore, at the same water content,

K^+ ions are more free to move than Na^+ in the polymer membrane, with the cation-anion dissociation effect dominating.

PFG-NMR is a widely used and direct method for measurement of water mobility. Figure 4(b) shows the water diffusion coefficient of five different membranes as a function of water content. The highest values of D_{H_2O} for K^+ form membrane and Na^+ form membrane are 1.4 $\times 10^{-11}$ m^2 s^{-1} and 3.8$\times 10^{-11}$ m^2 s^{-1}, respectively. These values are much smaller than the 6.6 $\times 10^{-11}$ m^2 s^{-1} of H^+ form 3M PFSA membrane as we reported previously[42]. D_{H_2O} (K^+ form membrane) is obviously higher than the D_{H_2O} (Na^+ form membrane) when compared at the same water content. Our results agree well with the water diffusion data for MF-4SC membrane reported by Volkov[37], which the water diffusion coefficient in the membrane decreases in the order H^+>Cs^+>Na^+>Li^+. We interpret the higher water diffusion coefficient in our K^+ form membrane relative to the Na^+ form to be related to the lower hydration energy of K^+ cation, leading to weaker water-cation interaction. This would yield more loosely bound (and free) water molecules in the K^+ form membranes.

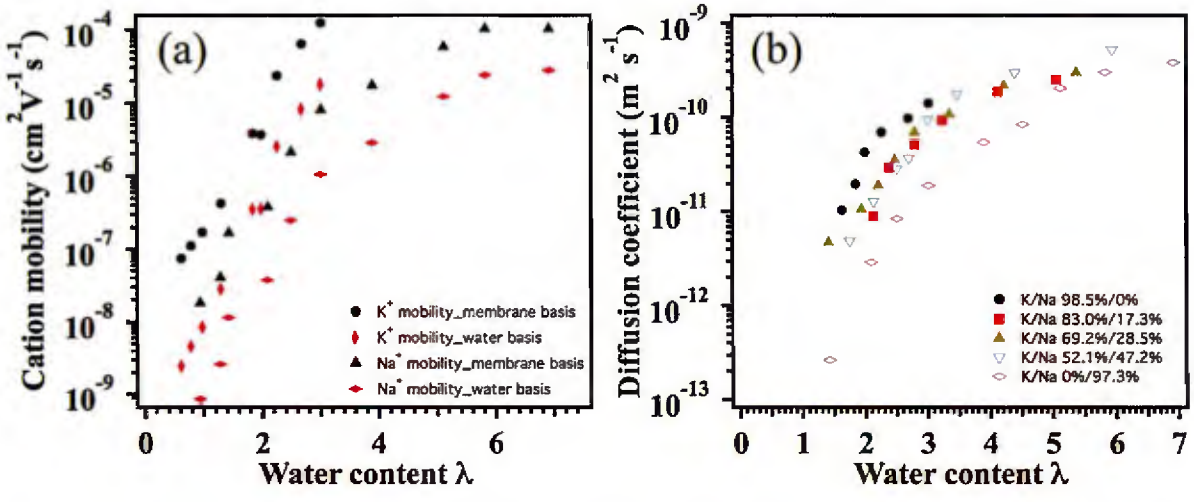

Figure 4 (a) Cation mobility of K^+ and Na^+ mobility in PFSA membrane versus water content λ (b) Water diffusion coefficient of five different PFSA membranes as a function of water content λ.

FT-IR spectra were recorded over the range 500 cm^{-1} to 4000 cm^{-1} for five hydrated PFSA membranes with various K^+ contents. The spectra are shown in Figure 5(a). The strong absorption bands at 1100~1200 cm^{-1} are assigned to overlapping CF_2 and CF_3 stretching

bands[62, 63]. The absorption peak at 1050 ~ 1065 cm^{-1} was fitted and separated into two bands. These arise from the symmetric stretching vibration of SO_3^-. The presence of a multicomponent band shape reveals two different SO_3^- chemical environments in the membrane. As reported in the literature[63], stronger cation-sulfonate interaction induces the polarization of the S-O dipole, leading to positive shift of $\upsilon_{SO_3^-}$. Therefore, it is reasonable to assign the higher frequency band (band 2) to the highly associated sulfonate group (cation-sulfonate association), while the lower frequency band (band 1) is assigned to those sulfonate groups which do not interact strongly with cations. The peak position of these two $\upsilon_{SO_3^-}$ for different membranes is plotted as a function of potassium percentage, shown in Figure 5(b), where the correlation of the cation ratio with the wavenumbers of $\upsilon_{SO_3^-}$ may provide information about the strength of cation-sulfonate interaction. The two bands both move to lower frequency as the K^+ percentage increases, revealing a decreasing polarization/electrostatic field. This suggests a *higher* degree of cation-sulfonate group dissociation if simply interpreted. This seems to contradict the general understanding of ion-association in these systems, which posits that the larger alkali metal ions show a higher degree of ion pair formation[29, 64]. However, the K^+ has significantly lower surface charge density than Na^+ and therefore would be expected to be less polarizing with respect to the sulfonate band.

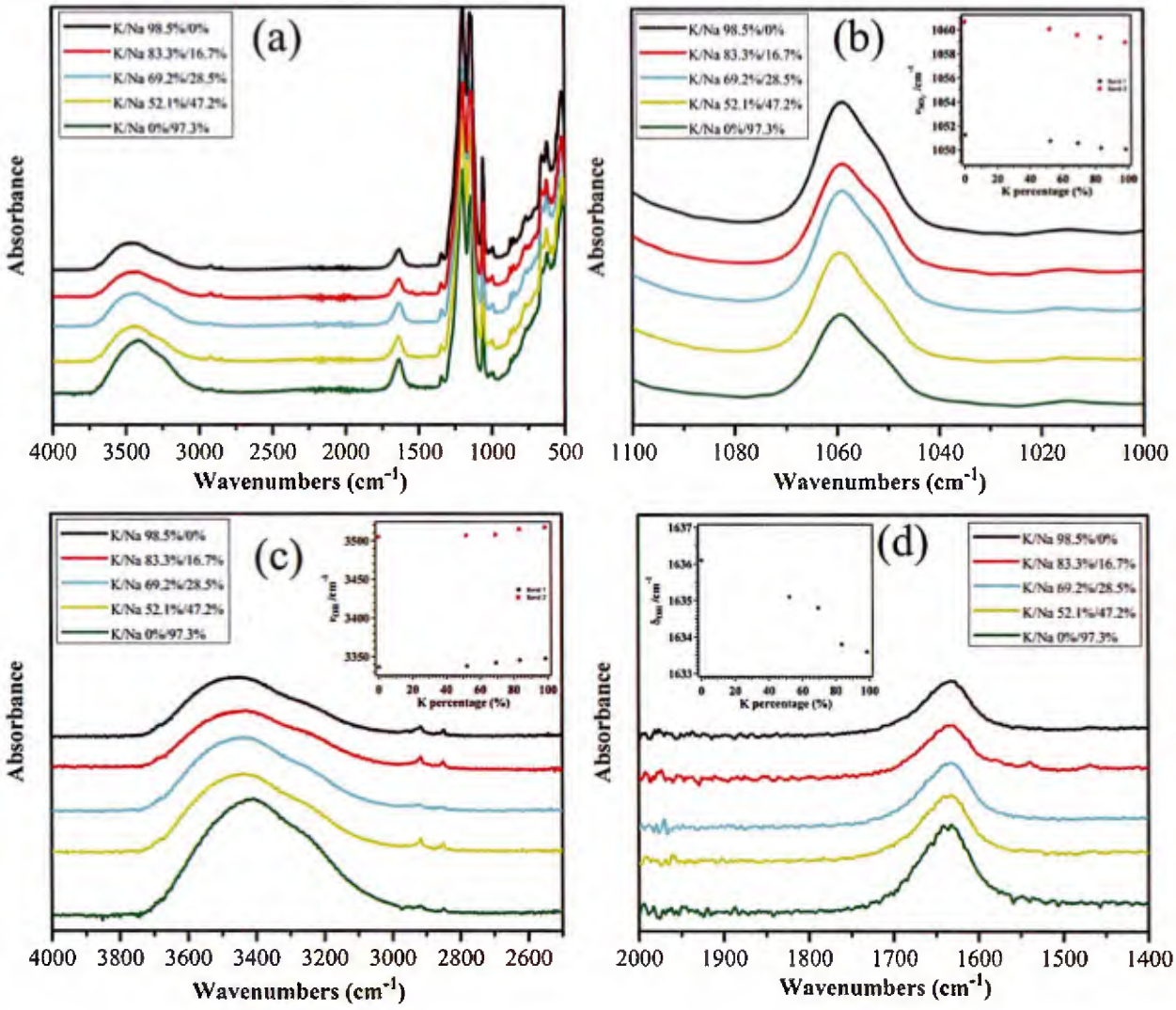

Figure 5(a) FT-IR spectra of various membrane forms; (b) Magnified spectra of symmetric stretching of SO_3^- (Insert: wavenumbers of symmetric stretching of SO_3^-); (c) Magnified spectra of OH stretching vibration band (Insert: wavenumbers of OH stretching vibration band); (d) Magnified spectra of OH bending vibration band (Insert: wavenumbers of OH bending vibration band).

The OH stretching modes v_{OH} at 3300~ 3600 cm^{-1} also consists of two sub-bands. Following Falk, the lower frequency band 1 is assigned to hydrogen bonded OH and the higher frequency band 2 is assigned to non-hydrogen bonded OH[62, 63]. It is known that the frequency of v_{OH} bands decrease with increasing strength of hydrogen bonding[63]. This agrees with our results that v_{OH} decreases as the K^+ percentage becomes lower and also agrees with the aforementioned

argument that uptake and transport results are caused by effects derived from the higher hydration energy of Na^+ vs. K^+. The behavior of the OH bending vibration band, δ_{OH}, shift is opposite to that of v_{OH}. Figure 5(d) shows the band positions of δ_{OH} as a function of potassium content in the membrane. The frequency of δ_{OH} reveals a negative shift as the potassium content increases as expected[65].

To summarize all of the results, the K^+ form membrane has lower water uptake from the vapor phase than does the sodium form. Nonetheless, the K^+ form is favored in partitioning from liquid water. The latter would appear to be a reflection of the larger cation size interacting with the sulfonate. However, when compared at the same water uptake (weight or volume based), the K^+ form surprisingly has significantly higher conductivity in spite of its larger ionic radius and known lower mobility in aqueous solution. Consistent with that result, interactions with the sulfonate as indicated by IR are actually weaker for the K^+ form. This probably reflects the lower surface charge density of the K^+ ions. Water mobility at the same water content is also higher in the case of the K^+ form. From these results, we conclude that understanding the interactions of cations in cation exchange membranes must take into account both the heat of hydration of the cation and the surface charge density of the ion. Failure to account for the latter will lead to erroneous expectations.

Transport of an ion in this type of system is controlled by a variety of factors, including the tortuosity of the transport pathway, the ability of the ion to dissociate and the mobility of the ion in the system. The first factor has been dealt with in other studies. Local motion occurring on very short time scales (sub-ns), as measured in an NMR relaxation rate measurement, reflects the chemical interactions of the ions or hydrated ions in the system. Longer range motions, as measured in conductivity or diffusion measurements, reflect this chemical information plus the tortuosity of the path for motion. Comparing changes in R_1 and D relative to the liquid indicates a factor of 1.5 (decreased in the membrane) difference in ratios, an estimate of the total tortuosity effect[5]. In this study, all measurement methods show a more or less constant offset in transport parameters (mobility, diffusion coefficient) between K^+ form, Na^+ form and various mixed K^+/Na^+ compositions. This suggests that the structural aspects, i.e. tortuosity, is essentially conserved from sample to sample as composition varies. Without more detailed investigation, we cannot separate changes in tortuosity with composition but, again, the results are consistent with any such changes being the same for all samples studied here.

In reference [66] (a modeling paper) it is suggested that there is a contribution from 'local' tortuosity versus long-range tortuosity. This is treated with an empirical expression. However, no experimental evidence of such a regime is available and the expression is not physically based. In our case, we present a clear observation of different ion interactions between sulfonates and K^+ or Na^+ by IR spectroscopy. Coupled with the constancy of the mobility differences with water content, we conclude that ion interactions with the sites, and not changes in morphology and concomitant changes in tortuosity, is the most important factor at low water content. This is also consistent with the partitioning phenomena observed.

We also reported an analysis of the applicability of the Nernst-Einstein (N-E) description relating ion conductivity to diffusivity to phase-separated single-ion conductors. This principle is the most fundamental description of total conductivity of a system based on individual ion mobilities. It had been commonly expected that the relationship was not valid for polymer electrolytes. To the contrary, we found that the ion transport could be reconciled with the Nernst-Einstein equation provided that regimes of high or low water uptake by which the membrane are treated differently. The N-E equation requires an ion concentration term. For high water contents, good agreement with the N-E equation is obtained if the concentration is calculated based only on the amount of water present, i.e. the membrane volume is ignored. For lower water contents, the concentration must be based on the total membrane volume for the diffusivity/conductivity behavior to comply. The division between these two regimes is roughly water content corresponding to the hydration number of the ion. This has implications for the study of hydrated polymer electrolytes as well as other 'channel' containing ion conductors. It led us to a concept of the ion-conductor as behaving in a very simple way, as a set of interconnected 'pipes' with sticky walls. At low water content, the ions 'stick' to the walls and the volume of the polymer materials is sampled during transport. At high water contents, the effect of these 'walls/ is minimized—the water flows as through a water channel.

We continued our work on the fundamentals of membrane behavior by the application of thermodynamic approaches to evaluate the uptake of acids into ion exchange membranes under conditions of equilibration of the membranes with concentrated solutions. This situation is encountered in practical electrochemical reactor systems such as redox flow batteries (RFBs). In these applications, a membrane separator is exposed to electrolyte solutions and/or gas phase environments, such as the electrolyte solutions in the RFBs which are usually composed of 3-5M

H_2SO_4 solutions The most commonly deployed separators for electrochemical applications are ion exchange membranes, such as Nafion and related perfluorosulfonic acid (PFSA) membranes. These exhibit phase separation between hydrophilic and hydrophobic phases. The hydrophilic phase typically contains an aqueous phase, with channels through which ions move[20].

The liquid bathing environments will come to equilibrium with the aqueous phase of the membrane. This affects the composition inside the membrane which, in turn, affects the critical transport phenomena that are central to the operating efficiency of the device. For example, in our recent work on vanadium redox batteries (VRBs—see below), we have shown that membranes exposed to concentrated solutions containing acid and vanadium exhibit unexpected transport properties stemming from the uptake of 'molecular' acid under Donnan breakthrough conditions, here the term 'breakthrough' refers to the breakdown of significant co-ion exclusion, resulting in the uptake of 'molecular' acid into the membrane, i.e. the concentration is sufficiently high to overcome the Donnan potential opposing co-ion uptake. Effects include membrane dehydration and complex coupling of transport of species as well as decreased conductivity in the presence of the imbibed electrolyte. Our detailed explication of these effects for multiple materials provides a glimpse into how these different materials respond.

Criteria for membrane selection are sorely needed to allow comparisons of disparate material types, including anion and cation exchange membranes, composite IEMs and so on. Unfortunately, the preponderance of studies of the physical chemistry of membranes in contact with electrolytes focuses on dilute solutions[67-71]. This is consistent with the long-standing application of ion exchange materials for simple separations or in ion selective electrodes. Donnan effects are often invoked in discussion of ion exclusion and the inhibition of transport of 'co-ions' but the thermodynamics underlying the effect is rarely elucidated and is in fact not completely developed.

The excellent work of Freeman and co-workers begins to assess the thermodynamics of uptake of salt into IEMs in the context of desalination applications[72, 73]. After developing an initial, broad thermodynamic framework to describe the equilibrium, they adapted the counterion condensation model of Manning to this purpose with good results for their system. The notion behind this theory is that as ionic strength increases and small amounts of salt are imbibed in the membrane, the average separation between ions decreases to below the Bjerrum length characteristic of ion pairs. At that point, the mobile ions tend to 'condense' around the fixed ion

sites in the polymer. While in this application the solution is still relatively dilute, this presents a step in the direction of a general description.

In this work we begin the development of an approach to description of uptake phenomena for higher concentrations associated with practical electrochemical applications. First we explore the applicability of the Freeman-Manning approach to provide a general framework for the description of the more complicated situation encountered in the membrane/highly concentrated electrolyte regime. In this first study, we begin from a relatively simple starting point by studying the uptake of strong acids into membranes. We present data on uptake of several different acids by two perfluorosulfonate membranes. The general thermodynamic framework allows us to calculate activity coefficients for the acids in the membrane. However, we find that the applicability of the counterion condensation model is limited. Returning to the broad framework of the problem, we describe a characteristic parameter, the Donnan potential. We show that this parameter behaves in a sensible manner as a description of the membrane properties. This gives us the basis for a characteristic membrane parameter that allows material comparison

First, we collect data describing that uptake for a series of acids in contact with perfluorosulfonic acid membranes. Figure 6 shows the uptake data that will be the basis of this investigation. There we give the acid uptake into a Nafion 1100 EW membrane for membranes exposed to solutions of one of three different acids as a function of concentration in the external solution. Some of plots are close to linear, particularly over the 'low' concentration range and the slopes in this regime reflect the moles inside the membrane relative to those in the bathing solution outside. The ratio of the outside concentration/inside concentration is between 1.5 (HBr) and ~25 (H_2SO_4) in different acid-membrane combinations.

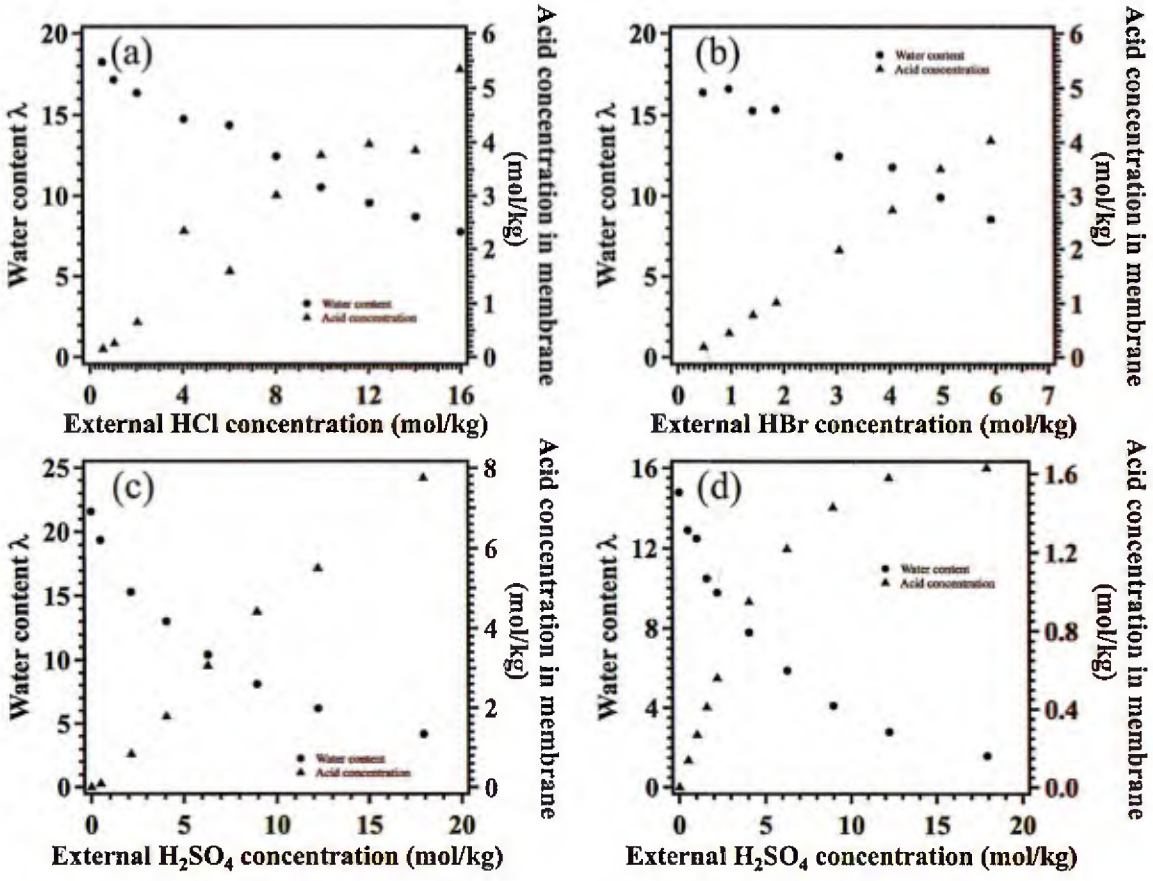

Figure 6: Water uptake and acid uptake in membranes as a function of external acid concentration, (a) HCl in Nafion 117 membrane; (b) HBr in Nafion 117 membrane; (c) H_2SO_4 in Nafion 117 membrane; (d) H_2SO_4 in 3M825 membrane.

It is commonly expected that an ion exchange membrane will exclude acids, salts and/or bases via the Donnan exclusion effect. This effect arises from the unfavorable electrostatic interaction between the fixed ion sites on the polymer with co-ions, i.e. ions of the same charge type, coupled to the requirement of electroneutrality. The data all show that significant acid is taken into the membrane, although in each case less acid is present in the membrane than in the bathing solution and this difference varies based on acid type. We conclude that we have achieved a situation of 'Donnan breakthrough' in which the chemical potential of the electrolyte exceeds the electrostatic co-ion repulsion that is the main feature of Donnan exclusion. We point out the large difference between data obtained for the Nafion and 3M ionomer samples. There are a number of causes of this difference. The EW's are different as are the morphologies.

These are the primary factors affecting uptake, in our opinion, but more information is likely needed.

As an alternative, based on the first part of the Freeman-Manning analysis we estimate the Donnan potential difference at the membrane surface. This parameter reliably captures the membrane behavior, with the potential tending toward the same constant value for the membrane exposed to different acids. The counterion condensation theory may provide insight into the evolution of the Donnan potential as a function of concentration in the low concentration regime.

Finally, we comment on the possible development of this approach as a useful predictive parameter for membrane behavior in RFBs. Our long-term goal is to develop correlations of the calculated parameters with underlying factors influencing the value of the Donnan potential, such as aspects of membrane structure and morphology, the ion exchange capacity of the material, mechanical properties of the material and surface states of the membrane. This will, in turn, provide a basis for comparison of broad classes of membranes. Structural studies to determine polymer phase segregation, pore formation and size of relevant features will include both microscopy and scattering studies are now underway but incomplete.

Over the past several years, there has been significant improvement in many characteristics of VRFBs. The overall rate at which redox flow batteries can be operated with good efficiency has been substantially increased. The work of the PNNL group has improved the temperature and concentration range of stability of electrolytes.[74, 75] This has been undergirded by detailed studies of many aspects of the components and devices, ranging from some first attempts to assess factors leading to durability or capacity fade to detailed studies of electrode kinetics to systematic investigations of water, acid and vanadium species uptake into membranes. Many of these studies have been reported for different cell designs, electrode materials and membrane types.

Redox flow batteries are a type of 'open battery' unlike the normal type of battery. Reagents flow in and out of the battery and contact electrodes. From that simple notion stem some important aspects of the structure of these batteries. In a normal battery, the layered electrodes and separator are wound to pack in high area per volume. The emphasis is strongly on achieving high energy density. For an open system, the manifolding and flow in a wound system is impractical and the common geometry is a stack of flat plate. To achieve high performance in this configuration requires higher power density and higher current density of operation. In the

traditional battery, an operating current density in the mA/cm^2 range and an ASR on the order of 10 ohm-cm^2 are typical. For the open system, this is not acceptable if we are to overcome the disadvantage of not being able to wind the components. Based on this, we focus on achieving much lower cell resistance and higher current density, both by orders of magnitude. By comparison to numbers given above, the ASR is ~0.05 ohm-cm^2 or less in a well-hydrated PEM fuel cell using membranes analogous to those in our flow battery.

The membrane electrolyte or separator used plays a key role in this cell resistance. We must use thin membranes for the highest performance. This alone allows us to significantly (and linearly) decrease resistance in the cell. Describing in more detail the membrane impact on performance, to the level at which the transport can be modeled, is quite complex. The membrane is exposed to concentrated acid solutions containing similar, though lower, concentrations of vanadium species in four difference oxidation states, the relative amounts of which vary with state of charge of the battery. Under these situations, it is entirely expected that the transport of any one of the species present (protons, water, up to 4 vanadium cations, 'membrane' and bisulfate) will be significantly coupled to that of the others. This implies that a 'concentrated solution theory' (CST) approach must be embraced.[77, 78] One of our goals has been to collect sufficient data to understand the possibilities for simplification of the monstrously complex description demanded by CST. Another part of our work has been to use observations under dilute solution conditions to provide some initial guidance to behavior, perhaps exhibiting some limiting aspects.

When exposed to concentrated electrolytes, the exclusion of co-ions expected from the Donnan equilibrium is no longer broadly operative. Electrolyte taken up by the membrane can alter the ionic equilibrium within membrane and further influence its ionic transport properties, such as conductivity and ion permeation, as well as water transport. The conductivity of cation exchange membrane, such as Nafion, is determined by its contents of electrolyte species. However, due to the complexity of ionic transport within ion exchange membrane under strong electrolyte equilibrium, very limited understanding has been established related to the fundamental mechanism of ion transport in this scenario. Some preliminary studies of acid-membrane interaction on membrane performance have been carried out for polymer electrolyte fuel cell study. Nafion equilibrated with sulfuric acid solution has been studied by several

research groups.[79-80] In the acid concentration range studied, sulfuric acid can effectively break through the Donnan potential caused by sulfonate in membrane. The partitioned sulfuric acid can alter ionic environment in Nafion and enhance its conductivity at low concentrations. Equilibration of Nafion with concentrated acid solutions also reduces its water content a critical facilitator of proton transport in IEMs[81]. The transport number of the anion in Nafion was measured to be less 0.1 within the studied acid concentration range, since the diffusivity of anions is more than one order of magnitude lower than that of protons in membrane. Hydrohalogenic and phosphoric acids have also been used in acid-membrane equilibration studies. The measured partitioning coefficients of HF, HCl and HBr were higher than sulfuric acid, and in the sequence of HF>HBr>HCl[82]. It was found that HF and phosphoric acid has very limited influence on membrane conductivity[83]. Kusoglu et al. carried out a more detailed study on Nafion equilibrated with HBr for hydrogen-bromine redox flow battery[84]. Small angle X-ray scattering was carried out to obtain morphological information and correlated to the ionic equilibrium and conductivity of membrane.

The presence of vanadium cations in the membrane is another important factor deciding membrane conductivity. Due to the differences in fundamental transport mechanism, the mobility of cations, $\sim 10^{-8}\ m^2 \cdot V^{-1} \cdot s^{-1}$, is generally at least one order of magnitude slower than that of protons ($u_{H^+} \cong 10^{-7}\ m^2 \cdot V^{-1} \cdot s^{-1}$) in fully hydrated Nafion[83, 85]. In a VRFB, vanadium cations can actively partition into the membrane to replace fast moving protons and reduce conductivity. Cho et al. [86] reported the vanadium partitioning isotherm in Nafion soaked in vanadium/acid mixed solution of different valence states, as well as membrane's conductivity after ion exchange. Conductivities of 20 to 30 mS/cm were estimated on Nafion 212 membrane with 21% V^{3+} and 12% VO^{2+} content. It has been shown that the Nafion membrane has a stronger affinity to multivalent cations than to protons and other monovalent cations[87-89]. Because some metal cations can reduce the water content in Nafion from its fully hydrated state, they can potentially impede proton motion. Some transition metal cations can directly interact with the proton to alter its mobility and thereby further influence membrane conductivity via an unclear mechanism[88]. Although most cation related studies of Nafion are not focused on vanadium chemistry, the results provide insight to help understand the ionic transport process in the membrane separator of VRFB.

Another line of recent research focuses on understanding and modeling the transport properties of vanadium ions in the environment of the VRFB. Measurements of crossover in a novel operating VRFB cell involving three flow regions show increased mobility of vanadium ions on the positive side through the membrane in the direction concurrent with the flux of protons. Crossover against the proton flux was reduced from the static state by 75%. However, the patterns of which ion species diffused and why suggested trends dependent on ion concentrations at varying SOC, such as increased transport of VO_2^+ at high current densities, when that ion would be increasingly present in the solution.[90]

A discrepancy exists in a number of studies in which side of the battery the vanadium tends to accumulate over the course of many cycles. Two different models suggest an expected build-up of vanadium in the negative reservoir. [91, 92] Meanwhile, two experimental reports describe an overall vanadium accumulation on the positive side. [93,94]

The modeling work of Knehr et al [91] is paired with experimental cycling data that shows a decrease in capacity over 45 cycles. The shorter charge time is attributed to vanadium imbalance in the electrolyte reservoirs. A model based on convection, diffusion and migration indicates the net accumulation of vanadium in the negative reservoir, but this is highly dependent on the viscosity values used as input in the model. There is limited data in the literature reporting on the viscosity of the negative electrolytes, particularly involving V^{2+}. The authors used viscosity values reported elsewhere (2.5cP), but the values from this measurement are in 1.5- 2M sulfuric acid, vs. 5M sulfuric acid used in the model. The value used as input for the viscosity of the positive electrolyte (1M Vanadium, 5M sulfuric acid) was 5cP. This was based on a handful of reports that measured viscosity of 1M VO^{2+} in 3M H_2SO_4 at ~5cP, 1M VO_2^+ in 5M H_2SO_4 at 5cP, and VO^{2+} and VO_2^+ in 5M H_2SO_4 at ~9 and 8 cP respectively. The vanadium concentration in the latter values, however, is not clear from the report. Meanwhile, other reports show values for 2M VO^{2+} and 2M H_2SO_4 at 2.69cP[95],2.11cP[96], and 2.79 cP [97]. Viscosity of 2M VO^{2+} in 5M H_2SO_4 have been reported at ~5 cP[98] and 5.169cP[97] and values of 1M VO^{2+} and 5M H_2SO_4 at 3.37 cP[98]. The authors of this study did not address the discrepancy between the model and experimental data, though they did refer to two earlier modeling studies that resulted in the opposite conclusion. Of those two references, one[99] is a thermal model of the battery and does not address cross over, and the other [100] used a selemion membrane, which in a

previous report was shown to result in the opposite trend to that Nafion showed (i.e. vanadium build up on the positive rather than negative side)[92]. The modeling work comparing anion and cation exchange selemion membranes to Nafion [92] results in vanadium accumulation in the positive reservoir, while the model suggests the opposite trend for the Nafion membrane, mainly as a result of higher diffusivity rates for vanadium ions in Nafion than the other membranes.

The first of the two experimental studies that suggested vanadium build up on the positive side of the battery over time monitored the concentrations of different ions in the electrolytes over cycling time using an automated titration instrument.[94] Interestingly, during self-discharge, vanadium accumulated on the negative side beginning at both 0% SOC and 65% SOC. In the case of monitoring crossover at 0% SOC where V^{3+} crossed against VO^{2+} over 90 hours ~13 moles of VO^{2+} crossed verses ~7 moles of V^{3+} which suggests a 3:2 crossover ratio, maintaining charge balance, which indicates an interdependence of the diffusion crossover of the two ions. During charge cycles, the overall accumulation of vanadium was on positive side and over 250 cycles, the amount of vanadium on the positive side increased by 35%. Tang et al. suggested that the reason for the difference here could be that Sun et al. only charged to 65% SOC and thereby avoided electrode gas reactions that occur at SOC above 90%. The second experimentally based report that observed the net accumulation of vanadium in the positive reservoir charged up to a SOC of 90%[101] However this experiment used iron ions counter to the vanadium ions, which could alter the crossover and used HCl instead of H_2SO_4 in the electrolyte, which could change the swelling patterns of the membrane in comparison to other studies.

We developed a synthesis of results to date and some new results describing uptake and mass transport of water, vanadium species and protons in Nafion membranes for use as separators in VRFBs. Resistance issues as well as species cross-over are important contributors to performance loss in VRFBs. After a brief discussion of our state-of-the-art cell performance, we consider the uptake and transport of various species through a number of membrane materials under various conditions. We draw together numerous previous studies and augment them with new data to provide a summary of our present state of understanding of the experimental facts regarding membrane behavior. From there, we compare rates of various processes and then sum up some expectations for transport in the membrane.

In Figure 7, we present polarization curves showing recently obtained levels of performance starting with electrolyte at ~100% state of charge. These results significantly surpass previously reported data [102-104]. Using SDAPP 2.3 as a membrane gave a peak power density of 2588 mW/cm^2 and a limiting current density of 5033 mA/cm^2 compared to Nafion 212's performance of 1355 mW/cm^2 at a limiting current density of 1817 mA/cm^2, both of which vastly exceeded the performance described in the references cited above.

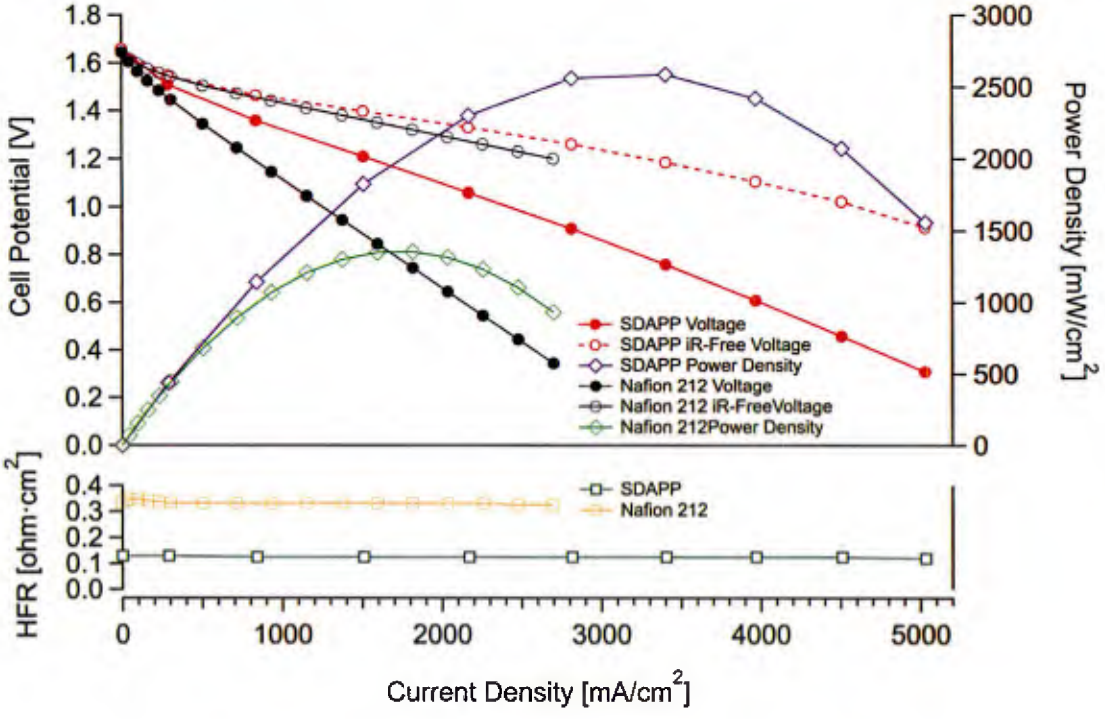

Figure 7. Single-pass discharge polarization curve of a zero-gap VRB comparing the performance of Nafion 212 to SDAPP.

iR-free polarization curves represent a combination of activation and concentration polarizations, which are primarily attributed to the electrode kinetics and mass transport through the electrode induced by the flow field, respectively.

We attribute the superior performance of SDAPP over Nafion 212 to higher selectivity of the membrane, i.e. a higher ratio of conductivity to permeability [105,106]. Improved electrode properties along with a concentrated electrolyte (1.7 M V^{x+} / 3.3 M H_2SO_4) at high flow rate minimize the losses due to kinetic and electro-active reagent mass transport processes. The cell voltage therefore shows a linear behavior as a function of current density. A system with that

level of performance is amenable to cycling with 90% efficiency at 500 mA/cm^2 or more. The cycling accesses lower states of charge and thus the actual cycling performance is not reflected by the polarization curve. However, such curves indicate the intrinsic, best case losses due to cell resistance, kinetic limitations and mass transport resistances in the cell. As can be seen in Figure 7, the essentially ohmic appearance of the polarization curves indicated that the latter are minimal. With a measured ASR of 0.13 ohm-cm^2, the IR corrected curve still shows some ohmic character. This is due to the ohmic loss associated with delivery of reagents through the pores of the electrode.

Therefore, to a first approximation, the slope of the iR-free curve shown in Figure 7 represents the ASR for ionic conduction in the electrode, consistent with AC impedance results. With the benefit of the constant OCV VRFB system given by the single pass mode, we are able to estimate the length of ionic pathway in the electrode according to Equation (1):

$$ASR = \frac{l}{\sigma_e} \times N_m \qquad (1)$$

where l is the membrane thickness, σ_e is the electrolyte conductivity, and N_m is the MacMullin number. The calculated path length is 0.2 mm, which represents the total conduction length for both electrodes including the tortuosity factor. If we assume that the loss due to the ionic conduction in the electrode is symmetric for positive and negative electrode, the conduction length for each side would be 100 μm. The thickness of the electrode (t) is approximately 134 μm in the cell with 30% compression. This result suggests that the reaction zone is geometrically toward the membrane side. This finding is opposed to previous studies, which suggest the reaction zone is closer to the current collector. In the higher performance cells used here different carbon electrode properties and the higher vanadium concentration electrolyte fed at 100% SoC in a single pass manner facilitate the mass transport of the active species and therefore move the reaction zone.

3.2 Influence of vanadium cations on ion transport in the polymer membrane: Dilute Solution Case

While it is well known that the conductivity of Nafion decreases dramatically due to prolonged exposure to acidic electrolyte solutions and that battery and efficiency losses may be attributed in part due to vanadium permeation across the membrane, much less is known about the equilibrium between Nafion and ionic solutions and its impact on proton transport. In general, multivalent cations are preferentially partitioned into Nafion compared to protons due to a larger electrostatic interaction and stronger binding energy with the negatively charged sulfonic acid group.[87, 103, 107] Although it has been demonstrated that factors other than valence, e.g. ionic size, can influence the cation partitioning competition in Nafion, valence state generally favors uptake of multivalent cations over monovalent cations.[89, 108] The solvation shell may play a role in screening the electrostatic interactions with sulfonic acid sites. In order to determine how these effects manifest in a VRB membrane environment, we have examined how uptake and conductivity are influenced in both the case of dilute and concentrated solutions.

In dilute solutions, the relative content of V^{3+} and VO^{2+} in the membrane trend closely in magnitude with respect to the relative vanadium content in solution the phase. These data are shown in Figure 8. The partitioning of V^{3+} into the membrane is only slightly stronger than VO^{2+}, despite V^{3+} having a higher ionic charge than VO^{2+}. (Note that the 'normalized' x-axis presents solution concentration as the mole fraction of vanadium in the proton/vanadium bathing mixture and the normalized y-axis presents the membrane concentration as the fraction of sulfonate sites 'occupied' by vanadium.) Perhaps the relatively small difference is due to the fact that V^{3+} has a more strongly held and saturated first hydration shell than does VO^{2+}, leading to more effective screening of charge (see below).

Also shown in Figure 8 is the effect that vanadium speciation in Nafion has on water content $\lambda = n_{H_2O}/n_{-SO_3H}$. Both V^{3+} and VO^{2+} have high affinity for sulfonate in the membrane, but surprisingly they do not significantly reduce membrane water content.[103] This is contradictory to other reported observations that water content loss is in accord with cation affinity to membrane.[87, 88] In those cases, tight ion pairing between ions and sulfonate sites leads to a diminished affinity for water. Our results suggest that cationic affinity to membrane is not the only dominating factor in determining water uptake of the membrane in the cation form. The highly hydrated vanadium cations themselves carry additional water into the membrane and the results would then indicate that it is likely that only solvent-separated ion-pairs form.[36]

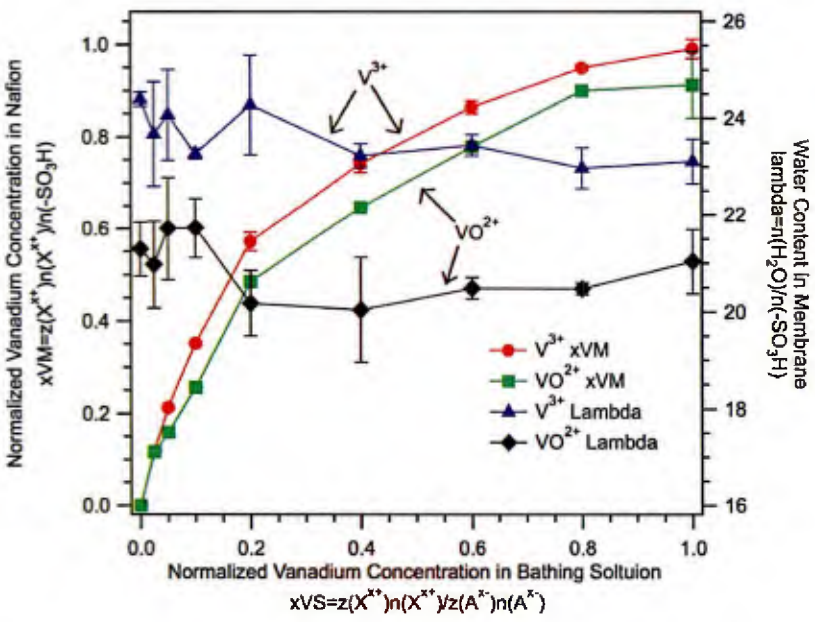

Figure 8. Normalized vanadium content in Nafion 117 with respect to the normalized vanadium concentration in the solution phase.

In the dilute electrolyte case the membrane is in the form H^+/V^x. The conductivity loss by VO^{2+} partitioning into Nafion has been studied in detail and it was shown that VO^{2+} strongly hinders proton motion and effectively lowers the proton concentration in the membrane.[103] The loss of conductivity due to V^{3+} is less pronounced than with VO^{2+} as shown in Figure 9(a). The interaction of VO^{2+} and V^{3+} with the membrane is thus likely different, leading to differing effects on proton mobilities. Overall, the membrane conductivity decreases by more than an order of magnitude as protons are replaced by vanadium ions.

Losses in conductivity could be caused by caused by lowered proton concentration and/or reduced proton mobility. The conductivity of membranes equilibrated in solutions of V^{3+} is given by:

$$\sigma_{m_{V3+}} = F(z_{H^+}c_{H^+}u_{H^+} + z_{V^{3+}}c_{V^{3+}}u_{V^{3+}}) \qquad (2)$$

where F is Faraday's constant, z is charge number, c is the concentration in the membrane phase and u the mobility. Equation (2) may be simplified by introducing a normalized content fraction $x_M = z_M c_M / c_{-SO_3H}$ giving:

$$\sigma_{m_{V^{3+}}} = Fc_{-SO_3H}(x_{H^+}u_{H^+} + x_{V^{3+}}u_{V^{3+}}) \quad (3)$$

where $c_{SO_3H^-}$ is calculated from the density measurement of fully hydrated proton-form Nafion and is assumed to be invariant of vanadium content. Equation (3) thus gives a simple means to calculate proton and V^{3+} mobilities from membrane uptake and conductivity measurements and these results are summarized in Table **Error! Reference source not found.**.

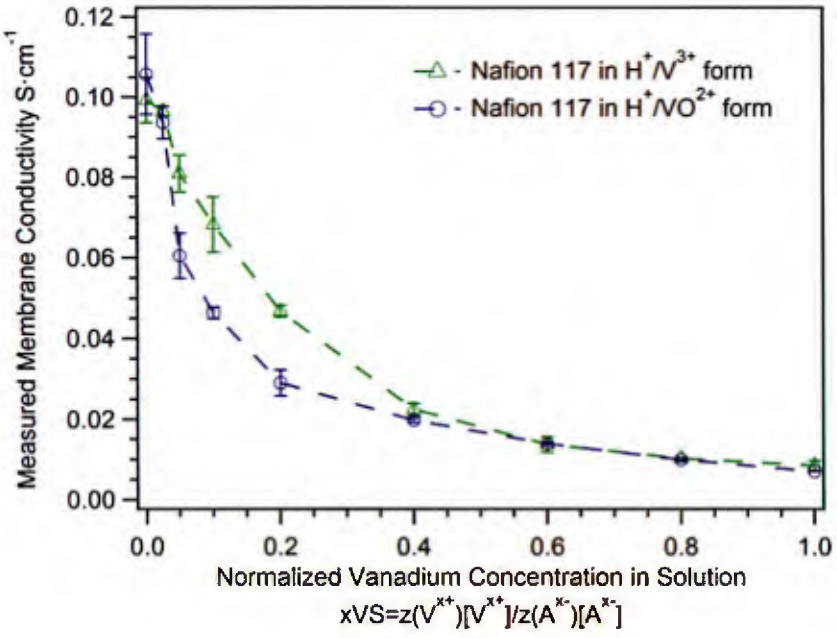

Figure 1. (a) Comparison between Nafion 117 conductivity loss as a function of vanadium concentration in the equilibrating solution for H^+/V^{3+} and H^+/VO^{2+} forms.

(b) Comparison between Nafion 117 conductivity loss as a function of vanadium concentration in the membrane for H^+/V^{3+} and H^+/VO^{2+} forms.

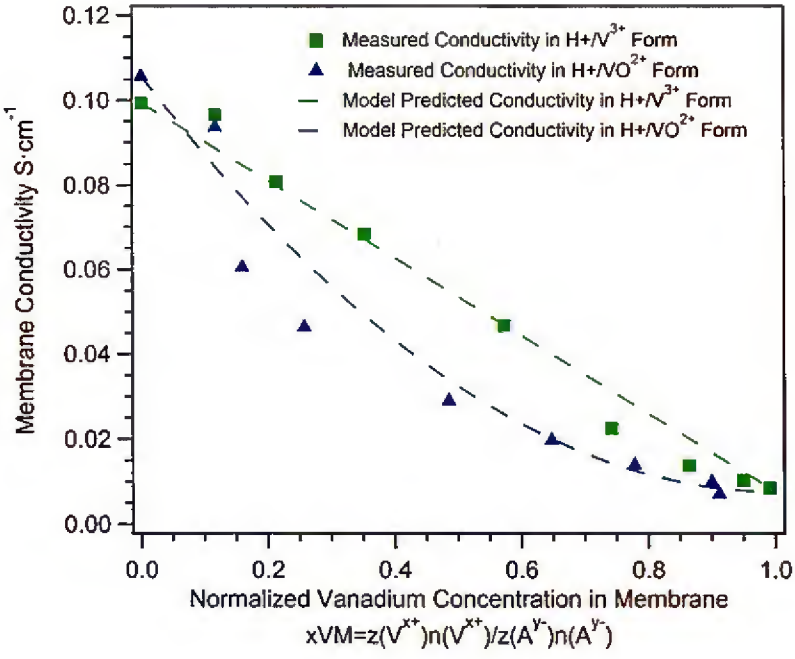

)

In Figure 9(b) we show the membrane conductivity's dependence on vanadium uptake. A model was constructed to fit the data, which assumed that: 1) the mobilities of the vanadium ions were constant, 2) H^+ mobility is linearly reduced by VO^{2+} abundance, and 3) H^+ has constant mobility in coexistence with V^{3+}. By calculation, V^{3+} and VO^{2+} both have much lower mobility than protons in proton form Nafion. As we can see here, in H^+/V^{3+} form membrane, conductivity is linearly decreased with increasing V^{3+} content in membrane. This implies that both proton and V^{3+} have essentially constant mobility within the entire vanadium content range. For VO^{2+}, the conductivity is obviously lower than that predicted for the constant mobility of both ions. Accordingly, we assume proton mobility is linearly decreased by $[VO^{2+}]$ in membrane. It turned out that membrane conductivity matches reasonable well with the linear proton mobility assumption. The changing proton mobility with VO^{2+} suggests there is an interaction between protons and VO^{2+}.

The structure of hydration shells and the complexation chemistry of vanadium ions is of great interest to clarify the behavior of V^{3+} and VO^{2+} exchanged Nafion and the apparent VO^{2+} effect on proton transport in the membrane.[109,110] Considerations of the structure and chemistry of the vanadium oxo species in particular have been presented. Based on classic

work by Ballhausen and Gray [111], Winkler and Gray [112] gave an excellent and useful overview on the vanadyl cation in the context of a more general discussion of metal oxo complexes. The V-O bond is exceptionally strong. One important takeaway from the latter is that the V-O bond includes significant back bonding contributions rendering the oxygen quite weakly basic. They report that the primary electronic band observed for this species is unchanged between pH -0.5 to 1.5. Vijayakumar et al. [113] presented a detailed discussion of the proposed interaction between $VO(H_2O)_5^{2+}$ and the sulfonate of Nafion. They presented several structures that were probed using electronic structure calculations and EXAFS at vanadium and sulfur edges. However, the spectra predicted did not present good matches. Moreover, the specific interactions proposed in that work, in which sulfonate enters the vanadyl primary solvation sphere seem unlikely in light of the similar mobility of this cation relative to that of $V(H_2O)_6^{3+}$ which we surmise from conductivity and permeability data.

Based on this, we conclude that the reason for the different cation-proton interactions has not been satisfactorily explained yet. One simple hypothesis that we find plausible is the possibility of protonation of the oxo moiety on the vanadium but the argument for that seems to be weakened by the comments of Winkler and Gray.

It has been demonstrated that high valence cations, like Al^{3+}, can form stable hydration shells beyond the first hydration shell by H-bonding.[114,115] Cations with higher valence can have more ordered hydration shells and stronger restriction on water molecules in hydration shell. Water in the hydration shells of multivalent cation is more condensed than in bulk water.[116] $V(H_2O)_6^{3+}$ has a water self-exchange rate constant of about $5\times10^2\ s^{-1}$ and $VO(H_2O)_5^{2+}$ has self-exchange rate constants of $5\times10^2\ s^{-1}$ on the equatorial positions and $\sim10^9\ s^{-1}$ on the axial position.[117] With high valence state, V^{3+} and VO^{2+} can constraint water in its hydration shell strongly enough to overcome the deswelling effect caused by cation uptake, thereby maintaining a higher hydration level in membrane.

3.3 Influence of vanadium cations on ion transport in the polymer membrane: Concentrated Solution Case

We now turn our attention to the case of VRBs in the context of concentrated solution theory. The results presented here should shed light on interactions of electrolyte solutions with

the polymer membranes under conditions that would mimic a more realistic operating battery. In this regime the vanadium (0-2 mol·dm^{-3}) and sulfuric acid (5 mol·dm^{-3}) were concentrated enough to overcome Donnan exclusion, or to achieve so-called Donnan breakthrough, for the anion to enter in significant quantities into the membrane. In contrast to the dilute case, Nafion samples equilibrated in concentrated solutions demonstrate a much less pronounced decrease in conductivity and show similar conductivity at a given vanadium concentration of the bathing electrolyte solutions regardless of the different valence state as shown in Figure 10.

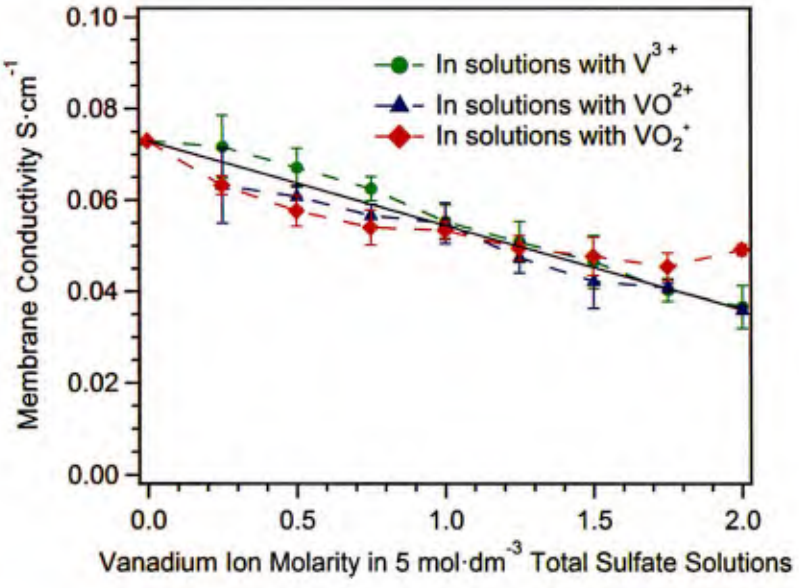

Figure 10. Nafion conductivity after being equilibrated in electrolyte solutions with vanadium in the +3, +4, and +5 valence states. The vanadium ion concentration in solutions was 0 to 2 mol·dm^{-3}; the total sulfuric acid/bisulfate/sulfate concentration was 5 mol·dm^{-3}.

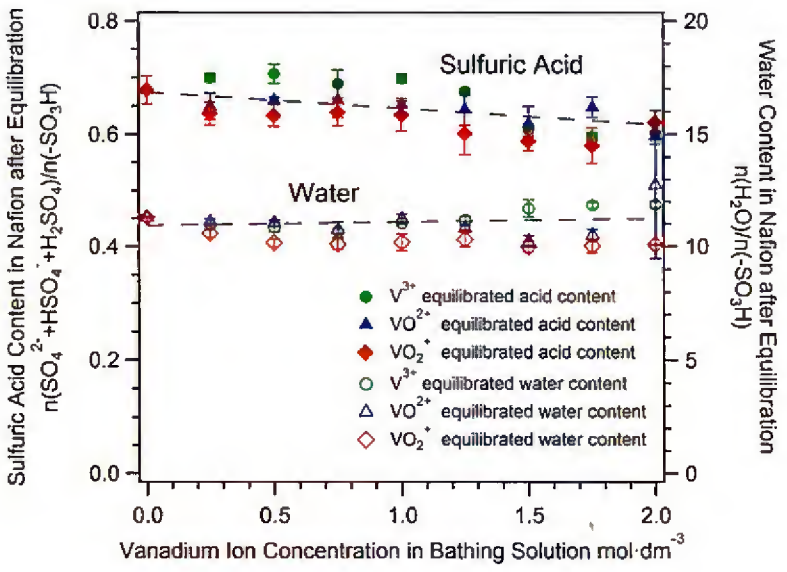

Figure 11. Water and sulfuric acid contents in Nafion equilibrated in concentrated electrolyte solutions (vanadium concentrations 0 to 2 mol·dm^{-3}; total sulfate 5 mol·dm^{-3}). The water and sulfuric acid concentrations are invariant with environmental concentration.

The water and sulfuric acid contents in Nafion equilibrated concentrated electrolyte solutions consistent with vanadium concentration results and are shown in Figure 11 Membrane water and sulfuric acid content are largely controlled by the acid concentration in the electrolyte environment. In dilute electrolyte equilibration, VO^{2+} and V^{3+} cannot significantly change water content in membrane. In the concentrated electrolyte scenario, the relatively unchanged water and sulfuric acid contents as a function of vanadium concentration suggest that vanadium ions do not affect membrane deswelling in the presence of large amounts of sulfuric acid. This is consistent with the observation on the vanadium concentration's influence on vanadium permeation across Nafion, which we expand upon below. It was illustrated that vanadium permeation, or diffusion, is mainly controlled by the sulfuric acid concentration in the electrolyte [118] (see below). This behavior suggests that equilibration with sulfuric acid is the primary factor determining Nafion water content, consistent with the decreasing water activity with increasing acid concentration and thereby the uptake of electrolyte species and vanadium crossover.

Vanadium ion partitioning in Nafion is highly dependent on the apparent charge number of the cation. The vanadium ion content in Nafion equilibrated in concentrated electrolyte is presented in Figure12. All three vanadium ion types in Nafion are nearly proportional to

vanadium concentration in the electrolyte solutions. V^{3+} and VO^{2+} have similar partitioning extent in Nafion, both stronger than VO_2^+. V^{3+} and VO^{2+} have higher partitioning in Nafion than VO_2^+ because cations with higher valence usually have higher affinity to sulfonate in membrane.[87, 89] V^{3+} and VO^{2+} have high positive charge to generate stronger electrostatic attraction to sulfonate. Although VO^{2+} has a lower apparent charge number than V^{3+}, VO^{2+} can still have similar affinity to V^{3+}, because it has a vanadium atom with +4 valence in the oxo complex. The affinity of VO^{2+} for sulfonate may be due to the high positive change on vanadium atom in it. The extent of solvation of the cation and the extent to which the ion's charge is screened also play roles.

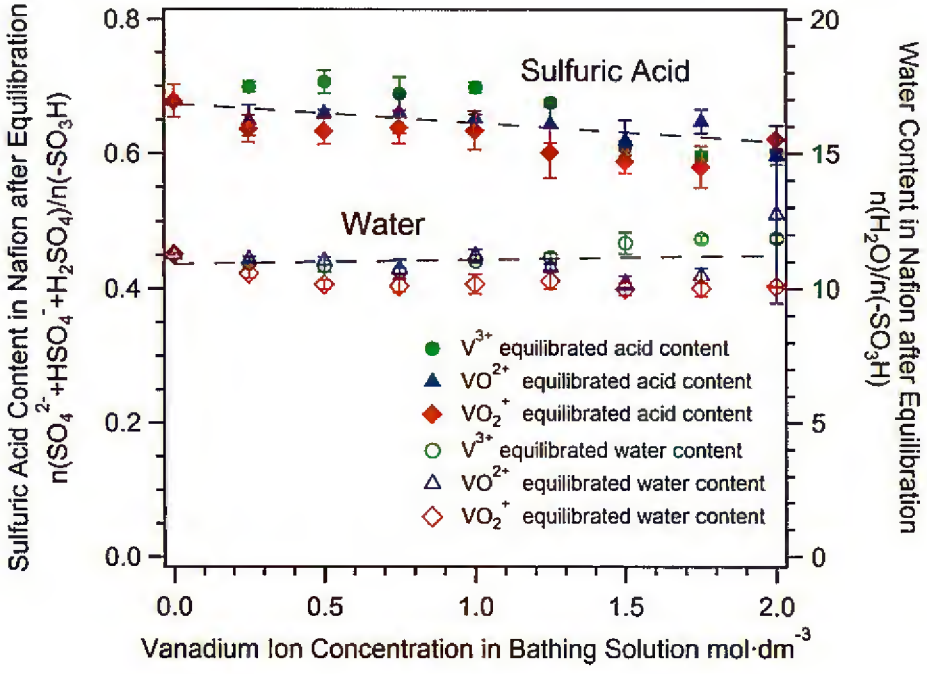

Figure 12. Vanadium ion content in Nafion being equilibrated in concentrated electrolyte solutions with V^{3+},VO^{2+} or VO_2^+.

As was the case in dilute solutions, vanadium ions that are partitioned into Nafion from concentrated solutions is the primary reason for the sharp decrease in membrane conductivity. The conductivity of Nafion is highly dependent on the water content given that proton transport is mitigated by water's roles as a mediator.[75, 119-121] The effective proton concentration in the membrane is enhanced by acid dissociation, an effect that is balanced by cations in the

membrane reducing the proton concentration and potentially interfering with proton transport.[88,122] Since the equilibrium in Nafion with concentrated electrolyte solutions includes all these factors (water, acid and cations) the analysis of Nafion conductivity in concentrated electrolyte is complicated and influences the proton mobility and in turn the proton transference number. We can now construct a model to account for these issues.

Because sulfuric acid and sulfonic acid in Nafion can fully dissociate, the charge balance is given by:

$$n_{H^+} + z_{V^{x+}} n_{V^{x+}} = n_{H_2SO_4} + n_{-SO_3H}. \quad (4)$$

Vanadium ions in Nafion reduce the number of protons available for charge transport, with a relative proton concentration of n_{H^+}/n_{-SO_3H}. The water content in Nafion equilibrated in the concentrated solutions should be corrected by water in vanadium ion's hydration sphere and extra sulfuric acid. It is assumed that water molecules in the first hydration shell of vanadium ions cannot take part in proton transfer. Water content available for proton transport is reduced: $n'_{H_2O} = n_{H_2O} - n_{V^{x+}} \times n_{V^{x+}}^{hydration}$. Here $n_{V^{x+}}^{hydration}$ is the hydration number of vanadium ions in their first hydration shells; with values of 6, 5, and 3 for V^{3+},VO^{2+} and VO_2^+ respectively.[75] Because of high hydrophobicity of bisulfate, we assume water can be similarly coordinated by sulfonate and bisulfate in the ionic domain in membrane. The corrected water content is symbolized as λ' is given by:

$$\lambda' = (\lambda - n_{V^{x+}}^{hydration} \frac{n_{V^{x+}}}{n_{-SO_3H}})/(1 + \frac{n_{H_2SO_4}}{n_{-SO_3H}}). \quad (5)$$

These results are shown in Figure 13.

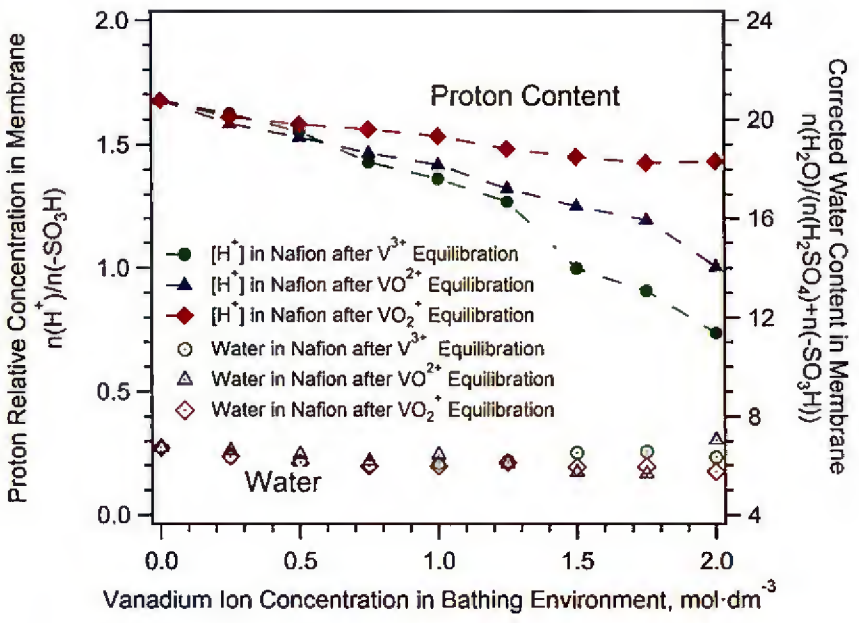

Figure 13. Proton content and corrected water content in Nafion after equilibration. The proton is provided by sulfuric and sulfonic acid dissociation and reduced by vanadium replacement. The water content is corrected by vanadium aqua-coordination and extra sulfuric acid.

In the presence of sulfuric acid, VO^{2+} and VO_2^+ influence proton transport in Nafion, while V^{3+} does not interfere with proton mobility. Our modeling analysis was carried out by assuming that proton mobility does not change in the presence of vanadium. It was previously shown that proton mobility is a linear function of water content in Nafion equilibrated with sulfuric acid.[103] Using these assumptions, an empirically derived relationship for the proton mobility's dependence on water content may be given by:

$$u_{H^+} = \left(6.88\lambda' - 12.5\right) \times 10^{-5} \mathrm{cm}^2 \cdot \mathrm{V}^{-1} \cdot \mathrm{s}^{-1}. \quad (6)$$

The proton transference number can then be calculated by the modeled proton mobility:

$$t_{H^+} = \frac{F c_{H^+} u_{H^+}}{\sigma_{measured}} = \frac{F \cdot c_{-\mathrm{SO_3H}} \cdot u_{H^+}}{\sigma_{measured}} \left(\frac{n_{\mathrm{H^+}}}{n_{-\mathrm{SO_3H}}}\right) \quad (7)$$

where c_{-SO_3H} is the sulfonate concentration in Nafion equilibrated in 5 mol·dm^{-3} sulfuric acid solution given by 1.39×10^{-3}mol·cm^{-3}, according to the Nafion density measurements, and is assumed to be constant over the entire vanadium concentration range in the experiment.[103] The calculated proton transference numbers are presented in Figure 14.

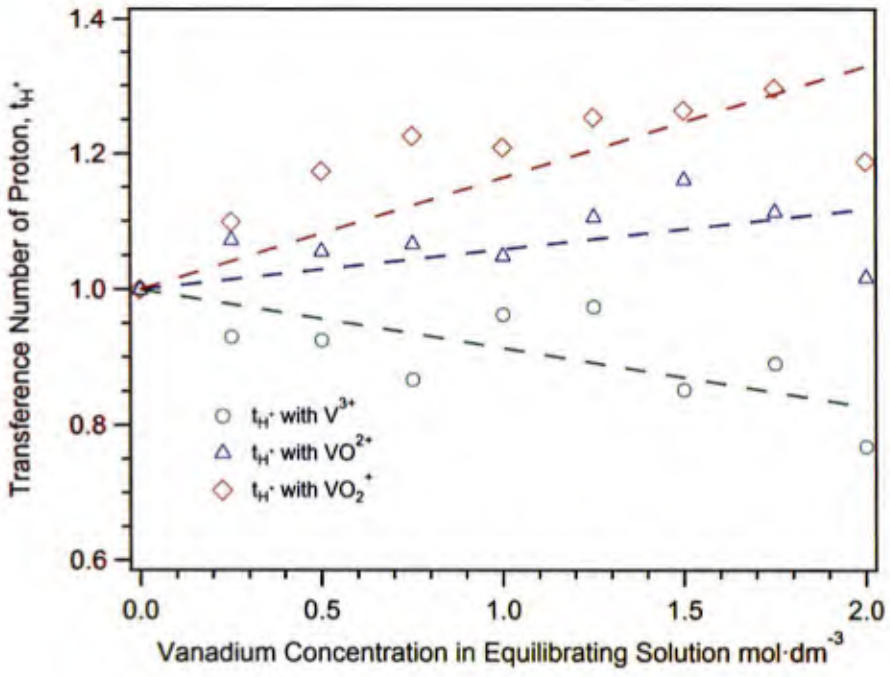

Figure 14. Proton transference number in Nafion with coexistence of vanadium ions (V^{3+}, VO^{2+} or VO_2^+) in concentrated electrolyte equilibration. The proton mobility is assumed to be only dependent on membrane's corrected water content.

Clearly, with the no-cation-interference assumption, protons coexisting with V^{3+} have transference numbers less than one and decrease with increasing acid concentration. This suggests that in the concentrated electrolytes, V^{3+} in Nafion does not influence proton transfer, similar to that in the dilute electrolyte equilibration case. The V^{3+} mobility can be calculated, $(6.3 \pm 0.8) \times 10^{-5}\ \mathrm{cm^2 \cdot V^{-1} \cdot s^{-1}}$, with the assumption that the anion transference number in Nafion is negligible due to Donnan exclusion.[92, 103, 123] This V^{3+} mobility is very close to V^{3+} mobility in the dilute electrolyte equilibration case. However, the proton transference number exceeds unity when protons coexist in the membrane with VO^{2+} or VO_2^+. This means that proton mobilities are overestimated with the no-vanadium-interference assumption or that the no-interference assumption is only valid for V^{3+}. Like the VO^{2+} influence on proton mobility in

dilute electrolyte equilibrium[103], VO^{2+} and VO_2^+ can reduce proton mobility by their presence in Nafion. VO_2^+ has a more significant decelerating effect on proton mobility than VO^{2+}. Since V^{3+} has the very similar mobility in Nafion equilibrated with dilute or concentrated electrolyte, in this case, we assume that VO^{2+} has mobility, 6.28×10^{-5} $cm^2 \cdot s^{-1} \cdot V^{-1}$, identical to its mobility in the dilute electrolyte equilibrated Nafion.

Concerning the mobility of VO_2^+ in Nafion, there is no literature report yet. So we assume that vanadium ions' mobility and diffusivity satisfy Einstein-Smoluchowski equation: $u_j \propto |z_j| D_j$.

The mobility of VO_2^+ can be derived from the diffusivities of vanadium ions reported in literature.[94] The derived mobility of VO_2^+ is 3.0×10^{-5} $cm^2 \cdot s^{-1} \cdot V^{-1}$. Proton mobility can be calculated by the relation between conductivity and mobility:

$$u_{H^+} = \frac{(\sigma - F z_{V^{x+}} c_{V^{x+}} u_{V^{x+}})}{F c_{H^+}} \tag{8}$$

The calculated proton mobility is dependent on the VO^{2+} or VO_2^+ content in Nafion, as is presented in Figure 15. Obviously, the decelerating effect of VO_2^+ is stronger than that of VO^{2+}.

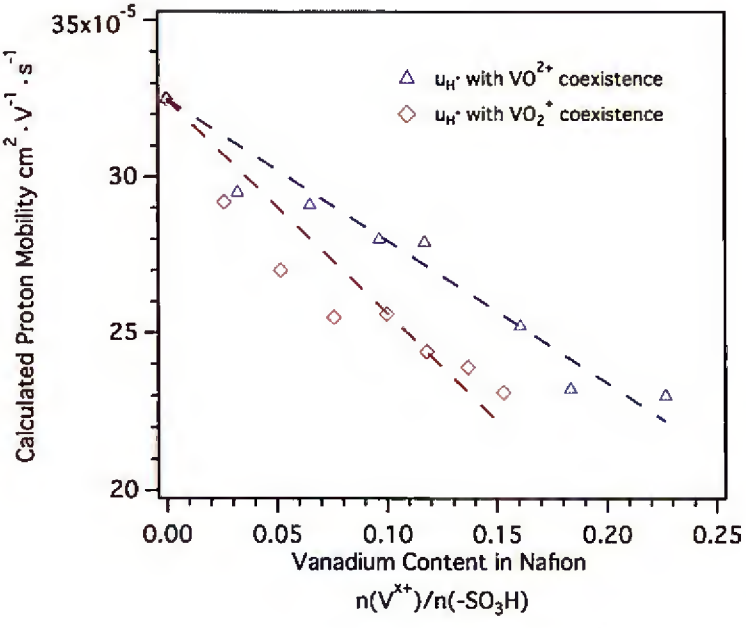

Figure 15. Calculated proton mobility as a function of vanadium content in Nafion for VO^{2+} and VO_2^+.

In an operating VRFB the driving force for species transport is a gradient in the electrochemical potential [124-126] and multi-component uptake of vanadium species, sulfuric acid, and anions will all have a pronounced effect especially at the higher concentrations that are being sought for grid-scale applications to maximize the volumetric energy density.[73] The models we constructed in this section were limited to "static" observations of how membrane conductivity, ion mobility, species uptake, and proton transference number were affected by acid and vanadium concentrations. An operando analysis of these parameters in working systems would help inform the theory of concentrated solutions for flow batteries and several groups are working towards that end.[127, 128] While Nafion has been thoroughly examined in VRFBs due to its high ionic conductivity and chemical stability, the high cost and significant vanadium crossover and key limiting factors to commercial adoption. We suggest that the considerations made above to characterize the effects of species uptake on performance will be of paramount importance.

3.4 Vanadium permeation through the membrane

The permeability of the vanadyl ion through Nafion is governed by the partitioning of the ion into the membrane as well as the diffusion coefficient of the ion in the membrane. These two variables are dependent on a number of factors. The partitioning is altered by the acid concentration in the solution around the membrane. As the acid concentration increases, the 'competition' for partitioning favors the protons. Diffusion is also affected by the acid concentration. Water in the membrane acts to form channels through which diffusion occurs, essentially lubricating the diffusion path. With exposure to acid, the membrane dehydrates slowing mobility of all species.[94, 97]

Previous work showed that the membrane permeability decreased dramatically with increasing acid concentration.[98, 129] For a simple experiment in which VO^{2+} permeation was monitored from a compartment which initially contained VO^{2+} in acid through the membrane to a compartment that contained only acid, the VO^{2+} permeation rates depended strongly on exact experimental conditions but were controlled by acid concentration. Increasing the VO^{2+} concentration while fixing the ratio acid to VO^{2+} yielded permeation data in which the permeation rate of VO^{2+} through the membrane decreased with increasing $[VO^{2+}]$. In general,

over the range of concentration between 0 and 5 M H_2SO_4, the permeability of VO^{2+} dropped by about two orders of magnitude.

Results for similar experiments for V^{3+}, measured using UV-Vis spectroscopy detection[21], and VO^{2+}, measured using EPR detection[118], are summarized in Table 1. Clearly, the permeation rates for the vanadium species are essentially similar and their respective mobilities are very slow relative to that of protons.

3.5 An Overall Summary of Transport

Capacity fade that occurs during cycling has been attributed in part to preferential volumetric transfer of vanadium ions and water. Transport of water occurs primarily by diffusion of hydrated species including protons, vanadium ions, sulfate and bisulfate ions, as a result of osmotic pressure differences and by migration of ions with accompanying electroosmotic flow. Using the figures measured or described above, it is possible to assess the relative rates of some of these transport processes that is expected during battery operation.

A calculation of the flux due to permeation as a current density yields 0.7×10^{-4} and 2.7×10^{-4} for V^{3+} and VO^{2+} respectively. Based on the mobilities, the transference number of protons is at least 0.87 and that of each vanadium species roughly 0.065 (assuming that all vanadium species are in the membrane). Thus, the fluxes due to migration at a current density of 100 mA/cm^2 are orders of magnitude higher than the permeation fluxes. Assuming that the electroosmotic drag coefficient is 3 for protons, 8 for V^{3+} and 7 for VO^{2+}, the flux of water due to drag in one direction will be on the order of 300 mA/cm^2 or roughly 50 times the vanadium flux.

Clearly, the absolute magnitude of these parameters will depend on the exact details of changes of composition during state of charge and thus requires modeling to integrate over these changes. It is useful nonetheless to have a rough idea of how rapidly different transport mechanisms for different species are likely to move those species.

References for Section II.1

[1] S.C. Yeo, A. Eisenberg, Physical properties and supermolecular structure of perfluorinated ion - containing (Nafion) polymers, Journal of applied polymer science, 21 (1977), pp. 875-898.

[2] D. Nandan, H. Mohan, R. Iyer, Methanol and water uptake, densities, equivalental volumes and thicknesses of several uni-and divalent ionic perfluorosulphonate exchange membranes (Nafion-117) and their methanol-water fractionation behaviour at 298 K, Journal of membrane science, 71 (1992), pp. 69-80.

[3] W.Y. Hsu, T.D. Gierke, Ion transport and clustering in Nafion perfluorinated membranes, Journal of Membrane Science, 13 (1983), pp. 307-326.

[4] K. Pushpa, D. Nandan, R. Iyer, Thermodynamics of water sorption by perfluorosulphonate (Nafion-117) and polystyrene–divinylbenzene sulphonate (Dowex 50W) ion-exchange resins at 298±1 K, Journal of the Chemical Society, Faraday Transactions 1: Physical Chemistry in Condensed Phases, 84 (1988), pp. 2047-2056.

[5] T.A. Zawodzinski Jr, M. Neeman, L.O. Sillerud, S. Gottesfeld, Determination of water diffusion coefficients in perfluorosulfonate ionomeric membranes, The Journal of Physical Chemistry, 95 (1991), pp. 6040-6044.

[6] J.A. Elliott, D. Wu, S.J. Paddison, R.B. Moore, A unified morphological description of Nafion membranes from SAXS and mesoscale simulations, Soft Matter, 7 (2011), pp. 6820-6827.

[7] A. Bıyıkoğlu, Review of proton exchange membrane fuel cell models, Int J Hydrogen Energ, 30 (2005), pp. 1181-1212.

[8] Y.J. Bai, M. Maalouf, A.B. Papandrew, T.A. Zawodzinski, Proton Conductivity and Partial Molar Volume of Different Polymer Electrolyte Membranes, Ecs Transactions, 41 (2011), pp. 1545-1553.

[9] M. Bass, A. Berman, A. Singh, O. Konovalov, V. Freger, Surface Structure of Nafion in Vapor and Liquid, The Journal of Physical Chemistry B, 114 (2010), pp. 3784-3790.

[10] M. Bass, V. Freger, Hydration of Nafion and Dowex in liquid and vapor environment: Schroeder's paradox and microstructure, Polymer, 49 (2008), pp. 497-506.

[11] P. Choi, N.H. Jalani, R. Datta, Thermodynamics and proton transport in Nafion II. Proton diffusion mechanisms and conductivity, J Electrochem Soc, 152 (2005), pp. E123-E130.

[12] P. Choi, N.H. Jalani, R. Datta, Thermodynamics and proton transport in Nafion I. Membrane swelling, sorption, and ion-exchange equilibrium, J Electrochem Soc, 152 (2005), pp. E84-E89.

[13] M. Pineri, G. Gebel, R.J. Davies, O. Diat, Water sorption–desorption in Nafion® membranes at low temperature, probed by micro X-ray diffraction, J Power Sources, 172 (2007), pp. 587-596.

[14] L.A. Zook, J. Leddy, Density and Solubility of Nafion: Recast, Annealed, and Commercial Films, Analytical Chemistry, 68 (1996), pp. 3793-3796.

[15] Y. Bai, M.S. Schaberg, S.J. Hamrock, Z. Tang, G. Goenaga, A.B. Papandrew, T.A. Zawodzinski Jr, Density Measurements and Partial Molar Volume Analysis of Different Membranes for Polymer Electrolyte Membrane Fuel Cells, Electrochimica Acta, 242 (2017), pp. 307-314.

[16] M. Skyllas-Kazacos, M.H. Chakrabarti, S.A. Hajimolana, F.S. Mjalli, M. Saleem, Progress in Flow Battery Research and Development, J Electrochem Soc, 158 (2011), pp. R55-R79.

[17] W. Wang, Q.T. Luo, B. Li, X.L. Wei, L.Y. Li, Z.G. Yang, Recent Progress in Redox Flow Battery Research and Development, Advanced Functional Materials, 23 (2013), pp. 970-986.

[18] E. Korngold, K. Kock, H. Strathmann, Electrodialysis in Advanced Waste-Water Treatment, Desalination, 24 (1978), pp. 129-139.

[19] R.L. Dotson, K.E. Woodard, Electrosynthesis with Perfluorinated Ionomer Membranes in Chlor-Alkali Cells, Acs Sym Ser, 180 (1982), pp. 311-364.

[20] K.A. Mauritz, R.B. Moore, State of understanding of Nafion, Chemical reviews, 104 (2004), pp. 4535-4586.

[21] B. Schwenzer, J. Zhang, S. Kim, L. Li, J. Liu, Z. Yang, Membrane development for vanadium redox flow batteries, ChemSusChem, 4 (2011), pp. 1388-1406.

[22] A. Steck, H.L. Yeager, Water sorption and cation-exchange selectivity of a perfluorosulfonate ion-exchange polymer, Analytical Chemistry, 52 (1980), pp. 1215-1218.

[23] R. Tandon, P.N. Pintauro, Divalent/monovalent cation uptake selectivity in a Nafion cation-exchange membrane: Experimental and modeling studies, Journal of Membrane Science, 136 (1997), pp. 207-219.

[24] H. Yeager, A. Steck, Ion-exchange selectivity and metal ion separations with a perfluorinated cation-exchange polymer, Analytical Chemistry, 51 (1979), pp. 862-865.

[25] M. Lopez, B. Kipling, H.L. Yeager, Ionic diffusion and selectivity of a cation exchange membrane in nonaqueous solvents, Analytical Chemistry, 49 (1977), pp. 629-632.

[26] H.L. Yeager, Cation Exchange Selectivity of a Perfluorosulfonate Polymer, Perfluorinated Ionomer Membranes, American Chemical Society1982, pp. 25-39.

[27] P. Pintauro, R. Tandon, L. Chao, W. Xu, R. Evilia, Equilibrium partitioning of monovalent/divalent cation-salt mixtures in Nafion cation-exchange membranes, The Journal of Physical Chemistry, 99 (1995), pp. 12915-12924.

[28] E. Vallejo, G. Pourcelly, C. Gavach, R. Mercier, M. Pineri, Sulfonated polyimides as proton conductor exchange membranes. Physicochemical properties and separation H+/M z+ by electrodialysis comparison with a perfluorosulfonic membrane, Journal of Membrane Science, 160 (1999), pp. 127-137.

[29] J. Bontha, P.N. Pintauro, Water orientation and ion solvation effects during multicomponent salt partitioning in a Nafion cation exchange membrane, Chem Eng Sci, 49 (1994), pp. 3835-3851.

[30] Y. Yang, P.N. Pintauro, Multicomponent space-charge transport model for ion-exchange membranes with variable pore properties, Ind. Eng. Chem. Res., 43 (2004), pp. 2957-2965.

[31] S. Shi, A.Z. Weber, A. Kusoglu, Structure-Transport Relationship of Perfluorosulfonic-Acid Membranes in Different Cationic Forms, Electrochimica Acta, 220 (2016), pp. 517-528.

[32] M. Legras, Y. Hirata, Q.T. Nguyen, D. Langevin, M. Métayer, Sorption and diffusion behaviors of water in Nation 117 membranes with different counter ions, Desalination, 147 (2002), pp. 351-357.

[33] N.H. Jalani, R. Datta, The effect of equivalent weight, temperature, cationic forms, sorbates, and nanoinorganic additives on the sorption behavior of Nafion®, Journal of Membrane Science, 264 (2005), pp. 167-175.

[34] A. Kusoglu, A.Z. Weber, New Insights into Perfluorinated Sulfonic-Acid Ionomers, Chemical Reviews, 117 (2017), pp. 987-1104.

[35] H.L. Yeager, A. Steck, Cation and Water Diffusion in Nafion Ion Exchange Membranes: Influence of Polymer Structure, J Electrochem Soc, 128 (1981), pp. 1880-1884.

[36] K. Hongsirikarn, J.G. Goodwin, S. Greenway, S. Creager, Effect of cations (Na+, Ca2+, Fe3+) on the conductivity of a Nafion membrane, J Power Sources, 195 (2010), pp. 7213-7220.

[37] V.I. Volkov, A.A. Pavlov, E.A. Sanginov, Ionic transport mechanism in cation-exchange membranes studied by NMR technique, Solid State Ionics, 188 (2011), pp. 124-128.

[38] T. Okada, S. Møller-Holst, O. Gorseth, S. Kjelstrup, Transport and equilibrium properties of Nafion® membranes with H+ and Na+ ions, J Electroanal Chem, 442 (1998), pp. 137-145.

[39] Z. Tang, R. Svoboda, J.S. Lawton, D.S. Aaron, A.B. Papandrew, T.A. Zawodzinski, Composition and conductivity of membranes equilibrated with solutions of sulfuric acid and vanadyl sulfate, J Electrochem Soc, 160 (2013), pp. F1040-F1047.

[40] M. Maalouf, B. Pyle, C.N. Sun, D.S. Wu, S.J. Paddison, M. Schaberg, M. Emery, K.H. Lochhaas, S.J. Hamrock, H. Ghassemi, T.A. Zawodzinski, Proton Exchange membranes for high temperature fuel cells: Equivalent weight and end group effects on conductivity, Ecs Transactions, 25 (2009), pp. 1473-1481.

[41] M. Maalouf, C.N. Sun, B. Pyle, M. Emery, G.M. Haugen, S.J. Hamrock, T.A. Zawodzinski, Factors enabling high mobility of protons and water in perfluorosulfonate membranes under low hydration conditions, Int J Hydrogen Energ, 39 (2014), pp. 2795-2800.

[42] J. Peng, K. Lou, G. Goenaga, T. Zawodzinski, Transport Properties of Perfluorosulfonate Membranes Ionic Exchanged with Cations. , Acs Appl Mater Inter, (2018), pp. Unpublished results.

[43] E.O. Stejskal, J.E. Tanner, Spin diffusion measurements: spin echoes in the presence of a time - dependent field gradient, The journal of chemical physics, 42 (1965), pp. 288-292.

[44] J. Palomo, P.N. Pintauro, Competitive absorption of quaternary ammonium and alkali metal cations into a Nafion cation-exchange membrane, Journal of Membrane Science, 215 (2003), pp. 103-114.

[45] E. Nightingale Jr, Phenomenological theory of ion solvation. Effective radii of hydrated ions, The Journal of Physical Chemistry, 63 (1959), pp. 1381-1387.

[46] N.H. Jalani, R. Datta, The effect of equivalent weight, temperature, cationic forms, sorbates, and nanoinorganic additives on the sorption behavior of Nafion®, Journal of membrane science, 264 (2005), pp. 167-175.

[47] G. Xie, T. Okada, The state of water in Nafion 117 of various cation forms, Denki Kagaku, 64 (1996), pp. 718-726.

[48] T. Gierke, G. Munn, F. Wilson, The morphology in nafion perfluorinated membrane products, as determined by wide - and small - angle x - ray studies, Journal of Polymer Science Part B: Polymer Physics, 19 (1981), pp. 1687-1704.

[49] T. Okada, M. Saito, K. Hayamizu, Ion and Water Transport Characteristics in Perfluorinated Ionomers: Molecular Interactions, Perfluorinated Polymer Electrolyte Membranes for Fuel Cells, (2008), pp. 37-77.

[50] T. Okada, Y. Ayato, M. Yuasa, I. Sekine, The effect of impurity cations on the transport characteristics of perfluorosulfonated ionomer membranes, The Journal of Physical Chemistry B, 103 (1999), pp. 3315-3322.

[51] T. Okada, N. Arimura, H. Satou, M. Yuasa, T. Kikuchi, Membrane transport characteristics of binary cation systems with Li+ and alkali metal cations in perfluorosulfonated ionomer, Electrochimica acta, 50 (2005), pp. 3569-3575.

[52] J. Peng, T.A. Zawodzinski, Ion transport in phase-separated single ion conductors, Journal of Membrane Science, 555 (2018), pp. 38-44.

[53] J. Peng, A.L. Roy, S.G. Greenbaum, T.A. Zawodzinski, Effect of CO2 absorption on ion and water mobility in an anion exchange membrane, J Power Sources, 380 (2018), pp. 64-75.

[54] Y.S. Kim, B.S. Pivovar, Moving beyond mass-based parameters for conductivity analysis of sulfonated polymers, Annual review of chemical and biomolecular engineering, 1 (2010), pp. 123-148.

[55] Y.S. Kim, B. Pivovar, Comparing proton conductivity of polymer electrolytes by percent conducting volume, Ecs Transactions, 25 (2009), pp. 1425-1431.

[56] K.M. Cable, K.A. Mauritz, R.B. Moore, Effects of hydrophilic and hydrophobic counterions on the Coulombic interactions in perfluorosulfonate ionomers, Journal of Polymer Science Part B: Polymer Physics, 33 (1995), pp. 1065-1072.

[57] S.S. Jang, V. Molinero, T. Çağın, W.A. Goddard, Nanophase-segregation and transport in Nafion 117 from molecular dynamics simulations: effect of monomeric sequence, The Journal of Physical Chemistry B, 108 (2004), pp. 3149-3157.

[58] M.K. Petersen, F. Wang, N.P. Blake, H. Metiu, G.A. Voth, Excess proton solvation and delocalization in a hydrophilic pocket of the proton conducting polymer membrane Nafion, The Journal of Physical Chemistry B, 109 (2005), pp. 3727-3730.

[59] T.D. Gierke, Ionic Clustering in Nafion Perfluorosulfonic Acid Membranes And its Relationship to Hydroxyl Rejection and Chlor-Alkali Current Efficiency, J Electrochem Soc, 124 (1977), pp. C319-C319.

[60] T.D. Gierke, W.Y. Hsu, The Cluster-Network Model of Ion Clustering in Perfluorosulfonated Membranes, Acs Sym Ser, 180 (1982), pp. 283-307.

[61] W.Y. Hsu, T.D. Gierke, Elastic Theory for Ionic Clustering in Perfluorinated Ionomers, Macromolecules, 15 (1982), pp. 101-105.

[62] M. Laporta, M. Pegoraro, L. Zanderighi, Perfluorosulfonated membrane (Nafion): FT-IR study of the state of water with increasing humidity, Physical Chemistry Chemical Physics, 1 (1999), pp. 4619-4628.

[63] G. Xie, T. Okada, T. Arimura, Fourier Transform Infrared Spectroscopy Study of Fully Hydrated Nation Membranes of Various Cation Forms, Zeitschrift für physikalische Chemie, 205 (1998), pp. 113-125.

[64] J. Savage, G.A. Voth, Proton solvation and transport in realistic proton exchange membrane morphologies, The Journal of Physical Chemistry C, 120 (2016), pp. 3176-3186.

[65] G.C. Pimentel, A.L. McClellan, The hydrogen bond, Reinhold Publishing Corporation, New York, 1960.

[66] A.R. Crothers, C.J. Radke, A.Z. Weber, Impact of Nano- and Mesoscales on Macroscopic Cation Conductivity in Perfluorinated-Sulfonic-Acid Membranes, The Journal of Physical Chemistry C, 121 (2017), pp. 28262-28274.

[67] K.M. Beers, D.T. Hallinan, X. Wang, J.A. Pople, N.P. Balsara, Counterion Condensation in Nafion, Macromolecules, 44 (2011) 8866-8870.

[68] G.S. Manning, Limiting Laws and Couterion Condensation in Polyelectrolyte Solutions.I. Colligative Properties, J Chem Phys, 51 (1969) 924-&.

[69] G.S. Manning, Limiting laws and counterion condensation in polyelectrolyte solutions II. Self - diffusion of the small ions, The Journal of Chemical Physics, 51 (1969) 934-938.

[70] G.S. Manning, Limiting Laws and Counterion Condensation in Polyelectrolyte Solutions .3. An Analysis Based on Mayer Ionic Solution Theory, J Chem Phys, 51 (1969) 3249-&.

[71] H. Ohshima, S. Ohki, Donnan potential and surface potential of a charged membrane, Biophysical Journal, 47 (1985) 673-678.

[72] J. Kamcev, M. Galizia, F.M. Benedetti, E.S. Jang, D.R. Paul, B.D. Freeman, G.S. Manning, Partitioning of mobile ions between ion exchange polymers and aqueous salt solutions: importance of counter-ion condensation, Physical Chemistry Chemical Physics, 18 (2016) 6021-6031.

[73] J. Kamcev, D.R. Paul, B.D. Freeman, Ion Activity Coefficients in Ion Exchange Polymers: Applicability of Manning's Counterion Condensation Theory, Macromolecules, 48 (2015) 8011-8024.

[74] L. Li, S. Kim, W. Wang, M. Vijayakumar, Z. Nie, B. Chen, J. Zhang, G. Xia, J. Hu, G. Graff, J. Liu, Z. Yang, A stable vanadium redox-flow battery with high energy density for large-scale energy storage, Advanced Energy Materials, 1 (2011) 394-400.

[75] M. Vijayakumar, L. Li, G. Graff, J. Liu, H. Zhang, Z. Yang, J.Z. Hu, Towards understanding the poor thermal stability of V5+ electrolyte solution in vanadium redox flow batteries, Journal of Power Sources, 196 (2011) 3669-3672.

[76] Y.P. Ma, M. Doyle, T.F. Fuller, M.M. Doeff, L.C. Dejonghe, J. Newman, The measurement of a complete set of transport-properties for a concentrated solid polymer electrolyte solution, Journal of the Electrochemical Society, 142 (1995) 1859-1868.

[77] N.P. Balsara, J. Newman, Relationship between steady-state current in symmetric cells and transference number of electrolytes comprising univalent and multivalent ions, Journal of the Electrochemical Society, 162 (2015) A2720-A2722.

[78] M.W. Verbrugge, R.F. Hill, Experimental and theoretical investigation of perfluorosulfonic acid membranes equilibrated with aqueous sulfuric-acid solutions, Journal of Physical Chemistry, 92 (1988) 6778-6783.

[79] G. Pourcelly, A. Lindheimer, C. Gavach, H.D. Hurwitz, Electrical transport of sulfuric-acid in nafion perfluorosulfonic membranes, Journal of Electroanalytical Chemistry, 305 (1991) 97-113.

[80] B.S. Pivovar, W.H. Smyrl, E.L. Cussler, Electro-osmosis in Nafion 117, polystyrene sulfonic acid, and polybenzimidazole, Journal of the Electrochemical Society, 152 (2005) A53-A60.

[81] T.A. Zawodzinski, C. Derouin, S. Radzinski, R.J. Sherman, V.T. Smith, T.E. Springer, S. Gottesfeld, Water-uptake by and transport through Nafion(r) 117 membranes, Journal of the Electrochemical Society, 140 (1993) 1041-1047.

[82] G. Pourcelly, A. Lindheimer, G. Pamboutzoglou, C. Gavach, Conductivity of sorbed hydrohalogenic acid in nafion perfluorosulfonic membranes, Journal of Electroanalytical Chemistry, 259 (1989) 113-125.

[83] T. Okada, G. Xie, O. Gorseth, S. Kjelstrup, N. Nakamura, T. Arimura, Ion and water transport characteristics of nafion membranes as electrolytes, Electrochimica Acta, 43 (1998) 3741-3747.

[84] A. Kusoglu, K.T. Cho, R.A. Prato, A.Z. Weber, Structural and transport properties of nafion in hydrobromic-acid solutions, Solid State Ionics, 252 (2013) 68-74.

[85] B. Kienitz, B. Pivovar, T. Zawodzinski, F.H. Garzon, Cationic contamination effects on polymer electrolyte membrane fuel cell performance, Journal of the Electrochemical Society, 158 (2011) B1175-B1183.

[86] H.S. Cho, M. Ohashi, J.W. Van Zee, Absorption behavior of vanadium in Nafion (r), Journal of Power Sources, 267 (2014) 547-552.

[87] T. Okada, Y. Ayato, M. Yuasa, I. Sekine, The effect of impurity cations on the transport characteristics of perfluorosulfonated ionomer membranes, Journal of Physical Chemistry B, 103 (1999) 3315-3322.

[88] T. Okada, N. Nakamura, M. Yuasa, I. Sekine, Ion and water transport characteristics in membranes for polymer electrolyte fuel cells containing H+ and Ca2+ cations, Journal of the Electrochemical Society, 144 (1997) 2744-2750.

[89] R. Tandon, P.N. Pintauro, Divalent/monovalent cation uptake selectivity in a nafion cation-exchange membrane: Experimental and modeling studies, Journal of Membrane Science, 136 (1997) 207-219.

[90] D.C. Sing, J.P. Meyers, Direct measurement of vanadium crossover in an operating vanadium redox flow battery, ECS Transactions, 50 (2013) 61-72.

[91] K. Knehr, E. Agar, C. Dennison, A. Kalidindi, E. Kumbur, A transient vanadium flow battery model incorporating vanadium crossover and water transport through the membrane, Journal of The Electrochemical Society, 159 (2012) A1446-A1459.

[92] A. Tang, J. Bao, M. Skyllas-Kazacos, Dynamic modelling of the effects of ion diffusion and side reactions on the capacity loss for vanadium redox flow battery, Journal of Power Sources, 196 (2011) 10737-10747.

[93] Y. Zhao, J. Xi, X. Teng, Z. Wu, X. Qiu, Electrolyte volume change study in all vanadium redox flow battery, Acta Chimica Sinica, 69 (2011) 132-136.

[94] C. Sun, J. Chen, H. Zhang, X. Han, Q. Luo, Investigations on transfer of water and vanadium ions across nafion membrane in an operating vanadium redox flow battery, Journal of Power Sources, 195 (2010) 890-897.

[95] C.-H. Wu, H.-Y. Liao, K.-L. Hsueh, J.-S. Hung, Study of the kinetics of vanadium redox reaction by rotating disk electrode, ECS Transactions, 35 (2011) 11-22.

[96] H.-Y. Yang, K.-L. Hsueh, C.-L. Hsieh, J.-S. Hung, Study of the kinetics of vanadium (ii)/(iii) redox reaction, ECS Transactions, 50 (2013) 87-92.

[97] J.S. Lawton, A. Jones, T. Zawodzinski, Concentration dependence of vo2+ crossover of nafion for vanadium redox flow batteries, Journal of The Electrochemical Society, 160 (2013) A697-A702.

[98] F. Rahman;, M. Skylls-Kazacos, Solubility of vanadyl sulfate in concentrated sulfuric acid solutions, J. Power Sources, 72 (1998) 105-110.

[99] A. Tang, S. Ting, J. Bao, M. Skyllas-Kazacos, Thermal modelling and simulation of the all-vanadium redox flow battery, Journal of Power Sources, 203 (2012) 165-176.

[100] M. Skyllas-Kazacos, L. Goh, Modeling of vanadium ion diffusion across the ion exchange membrane in the vanadium redox battery, Journal of Membrane Science, 399 (2012) 43-48.

[101] Q. Luo, L. Li, Z. Nie, W. Wang, X. Wei, B. Li, B. Chen, Z. Yang, In-situ investigation of vanadium ion transport in redox flow battery, Journal of Power Sources, (2012).

[102] D.S. Aaron, Q. Liu, Z. Tang, G.M. Grim, A.B. Papandrew, A. Turhan, T.A. Zawodzinski, M.M. Mench, Dramatic performance gains in vanadium redox flow batteries through modified cell architecture, Journal of Power Sources, 206 (2012) 450-453.

[103] Z. Tang, R. Svoboda, J.S. Lawton, D.S. Aaron, A.B. Papandrew, T.A. Zawodzinski, Composition and conductivity of membranes equilibrated with solutions of sulfuric acid and vanadyl sulfate, Journal of the Electrochemical Society, 160 (2013) F1040-F1047.

[104] J.-Y. Chen, C.-L. Hsieh, N.-Y. Hsu, Y.-S. Chou, Y.-S. Chen, Determining the limiting current density of vanadium redox flow batteries, Energies, 7 (2014) 5863-5873.

[105] Z. Tang, J.S. Lawton, C.-N. Sun, J. Chen, M.I. Bright, A.M. Jones, A.B. Papandrew, C.H. Fujimoto, T.A. Zawodzinski, Characterization of sulfonated diels-alder poly(phenylene) membranes for electrolyte separators in vanadium redox flow batteries, Journal of the Electrochemical Society, 161 (2014) A1860-A1868.

[106] C. Fujimoto, S. Kim, R. Stains, X. Wei, L. Li, Z.G. Yang, Vanadium redox flow battery efficiency and durability studies of sulfonated diels alder poly(phenylene)s, Electrochemistry Communications, 20 (2012) 48-51.

[107] K.L. Huang, T.M. Holsen, J.R. Selman, Impurity partitioning in nafion and ceramic separators used for purification of spent chromium plating solutions, Journal of Membrane Science, 210 (2002) 137-145.

[108] P.N. Pintauro, R. Tandon, L. Chao, W. Xu, R. Evilia, Equilibrium partitioning of monovalent/divalent cation-salt mixtures in nafion cation-exchange membranes, Journal of Physical Chemistry, 99 (1995) 12915-12924.

[109] J. Krakowiak, D. Lundberg, I. Persson, A coordination chemistry study of hydrated and solvated cationic vanadium ions in oxidation states plus iii, plus iv, and plus v in solution and solid state, Inorganic Chemistry, 51 (2012) 9598-9609.

[110] M. Saito, N. Arimura, K. Hayamizu, T. Okada, Mechanisms of ion and water transport in perfluorosulfonated ionomer membranes for fuel cells, Journal of Physical Chemistry B, 108 (2004) 16064-16070.

[111] C.J. Ballhausen, H.B. Gray, The electronic structure of the vanadyl ion, Inorganic Chemistry, 1 (1962) 111-122.

[112] J.R. Winkler, H.B. Gray, Electronic structures of oxo-metal ions, in: D.M.P. Mingos, P. Day, J.P. Dahl (Eds.) Molecular electronic structures of transition metal complexes i2012, pp. 17-28.

[113] M. Vijayakumar, L. Li, Z. Nie, Z. Yang, J. Hu, Structure and stability of hexa-aqua v(iii) cations in vanadium redox flow battery electrolytes, Physical Chemistry Chemical Physics, 14 (2012) 10233-10242.

[114] P.A. Bergstrom, J. Lindgren, M. Read, M. Sandstrom, Infrared spectroscopic evidence for second-sphere hydration in aqueous solutions of aluminum(3+), chromium(3+) and rhodium(3+), Journal of Physical Chemistry, 95 (1991) 7650-7655.

[115] J. Stangret, T. Gampe, Ionic hydration behavior derived from infrared spectra in hdo, Journal of Physical Chemistry A, 106 (2002) 5393-5402.

[116] I. Waluyo, C. Huang, D. Nordlund, U. Bergmann, T.M. Weiss, L.G.M. Pettersson, A. Nilsson, The structure of water in the hydration shell of cations from x-ray raman and small angle x-ray scattering measurements, Journal of Chemical Physics, 134 (2011).

[117] E. Wiedemann, A. Heintz, R.N. Lichtenthaler, Transport properties of vanadium ions in cation exchange membranes: Determination of diffusion coefficients using a dialysis cell, Journal of Membrane Science, 141 (1998) 215-221.

[118] J.S. Lawton, D.S. Aaron, Z. Tang, T.A. Zawodzinski, Qualitative behavior of vanadium ions in nafion membranes using electron spin resonance, Journal of Membrane Science, 428 (2013) 38-45.

[119] T.A. Zawodzinski, T.E. Springer, J. Davey, R. Jestel, C. Lopez, J. Valerio, S. Gottesfeld, A comparative study of water uptake by and transport through ionomeric fuel cell membranes, Journal of the Electrochemical Society, 140 (1993) 1981-1985.

[120] T.A. Zawodzinski, C. Derouin, S. Radzinski, R.J. Sherman, V.T. Smith, T.E. Springer, S. Gottesfeld, Water uptake by and transport through Nafion(r) 117 membranes, Journal of the Electrochemical Society, 140 (1993) 1041-1047.

[121] M.A. Hickner, Water-mediated transport in ion-containing polymers, Journal of Polymer Science Part B-Polymer Physics, 50 (2012) 9-20.

[122] A. Lehmani, P. Turq, M. Perie, J. Perie, J.P. Simonin, Ion transport in Nafion(r) 117 membrane, Journal of Electroanalytical Chemistry, 428 (1997) 81-89.

[123] G. Pourcelly, A. Lindheimer, C. Gavach, H.D. Hurwitz, Electrical transport of sulphonic acid in nafion perfluorosulphonic membranes, Journal of Electroanalytical Chemistry, 305 (1991) 97-113.

[124] J.P. Meyers, J. Newman, Simulation of the direct methanol fuel cell - ii. Modeling and data analysis of transport and kinetic phenomena, Journal of the Electrochemical Society, 149 (2002) A718-A728.

[125] D.C. Sing, P.H. Michael, J.P. Meyers, Redox flow battery simulations for optimizing separator membrane performance, ECS Transactions, 41 (2012) 11-24.

[126] Y.A. Gandomi, T.A. Zawodzinski, M.M. Mench, Concentrated solution model of transport in all vanadium redox flow battery membrane separator, ECS Transactions, 61 (2014) 23-32.

[127] B. Li, Q. Luo, X. Wei, Z. Nie, E. Thomsen, B. Chen, V. Sprenkle, W. Wang, Capacity decay mechanism of microporous separator-based all-vanadium redox flow batteries and its recovery, Chemsuschem, 7 (2014) 577-584.

[128] Y.A. Gandomi, D.S. Aaron, T.A. Zawodzinski, M.M. Mench, In situ potential distribution measurement and validated model for all-vanadium redox flow battery, Journal of the Electrochemical Society, 163 (2016) A5188-A5201.

[129] Z.-Z. Lu, S.-L. Hu, X.-L. Luo, Z.-H. Wu, L.-Q. Chen, X.-P. Qiu, Effects of proton exchange membranes on performance of vanadium redox flow battery, Chemical Journal of Chinese Universities-Chinese, 28 (2007) 145-148.

[130] M.W. Verbrugge, R.F. Hill, Ion and solvent transport in ion - exchange membranes ii . A radiotracer study of the sulfuric - acid, Nafion - 117 system, Journal of the Electrochemical Society, 137 (1990) 893-899.

II.2 Polyoxometallates and their Use as Electrochemical Mediators

We also studied the behavior of poly(oxometallates) (POMs) as potential electrochemical mediators.This class of mediators provides a versatile group of compounds that might carry out reactions external to a cell, followed by recycling at the electrode. We have been using these mediators in previous ONR work and wanted to extend our study.

Recent reports on the use of polyoxometalates for electrochemistry have inspired questions about their fundamental electrochemical properties. Phosphomolybdic acid is the longest known keggin ion polyoxometalate. Berzelius prepared and analyzed the first keggin ion $(NH_4)_3PMo_{12}O_{40}$ in 1826, the tungstosilic acid was prepared by Margnac in 1862. The first systematic attempt to understand the nature of heteropoly compounds occurred in 1908 by Miolati. Some of the most significant work was done by Tsigdinos, who published methods using ether extraction for the synthesis and purification of phosphomolybdic acid. [1]

Tsigdinos studied the redox behavior of 12-phosphomolybdic acid which he refers to as dodeca-molybdophosphoric acid. He found multiday stability of polarograms in 0.5 M H_2SO_4, indicating stability in that solvent. He also found that solutions more dilute than 10^{-4} M gave less well defined polarograms. Reversibility of the first 3 waves was ascertained using cyclic voltammetry at a platinum electrode in water-dioxane solutions. He states that is important not to use earlier work due to an unrecognized hydrolytic instability on mercury electrodes and at elevated pH values.[70] Tsigdinos also prepared many of the polyoxometalates including $FePMo_{12}O_{40}$, $PVMo_{12}O_{40}$, $PV_2Mo_{10}O_{40}$, and $PWMo_{11}O_{40}$. [1]

Based upon these reports it became clear that the electrochemistry of keggin ions varied widely with solvent, necessitating study of the electrochemistry of phosphomolybdic acid in the proposed reaction conditions. The reaction of phosphomolybdic acid on glassy carbon was studied to determine if a heterogeneous catalyst is necessary. The oxidation of phosphomolybdic acid was then studied using a glassy carbon rotating disk electrode to attempt to elucidate the kinetics of the oxidation reaction. Then a small cell with a hydrogen counter electrode was assembled to test the anode performance of a phosphomolybdic acid based fuel cell/hydrogen pump. The literature shows several promising examples of fuel cells and hydrogen pumps using phosphomolybdic acid as a mediator but the performance of such devices is hard to ascertain due to the coupling of cell performance and solution reaction.[2-5] There is significant discussion concerning the current

efficiency but little to no discussion of voltage efficiency. What are the sources of voltage loss, the kinetic, ohmic, and mass transport overpotential required to reoxidize the phosphomolybdic acid.

One important characteristic which will significantly affect the overpotential required is the degree of reversibility. Based upon the literature we know that the electrochemical stability and therefore reversibility of phosphomolybdates will vary with solvent. It is highly desirable to use an aqueous solvent because aqueous solvents tend to provide excellent solubility (900+ g/L for phosphomolybdic acid), low cost, and high conductivity.

These materials have been studied since their discovery in the 1800s but little has been done in recent decades. None of the older literature studied the aqueous mixtures preferred in modern biomass oxidation studies.

Here we report fundamental electrochemical studies of phosphomolybdic acid. We study the electrochemical reversibility, diffusion coefficient, number of electrons transferred, and chemical reversibility. These studies are carried out using cyclic voltammetry, rotating disk electrode voltammetry, bulk electrolysis, and thin layer voltammetry. We also study the nature of the change in the number of electrons transferred with the reduction state of the bulk solution.

Cyclic voltammetry (CV) was used to determine the overall of behavior of POM compounds. 15 gives the cyclic voltammograms of phosphomolybdic acid on a glassy carbon electrode. To help elucidate some of the kinetic information contained within 15, Figure 16 and 17 were constructed. Figure 16 contains the plot of peak separation vs scan rate. An ideally reversible reaction would show no dependence of peak separation on scan rate. Figure 17 is the plot of peak current vs the square root of scan rate. Reversible reactions show a linear relationship between these variables.

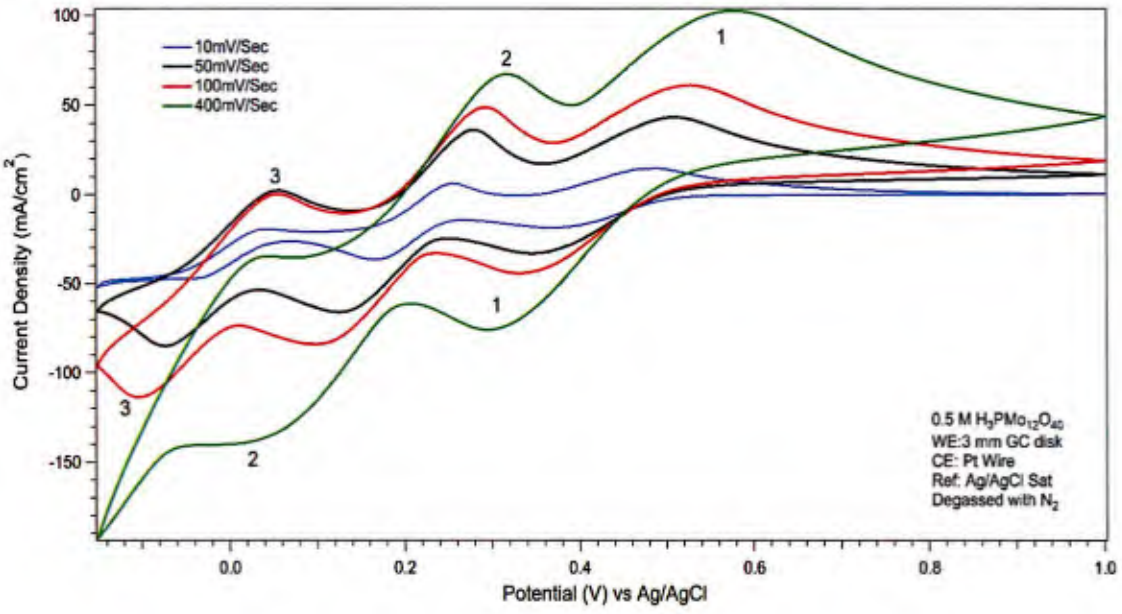

Figure 15: Cyclic Voltammetry of Phosphomolybdic Acid on Glassy Carbon. 0.5 M $H_3PMo_{12}O_{40}$, We: 3mm GC disk, Ce: Pt wire, Ref: Ag/AgCl (0.205 V vs NHE)

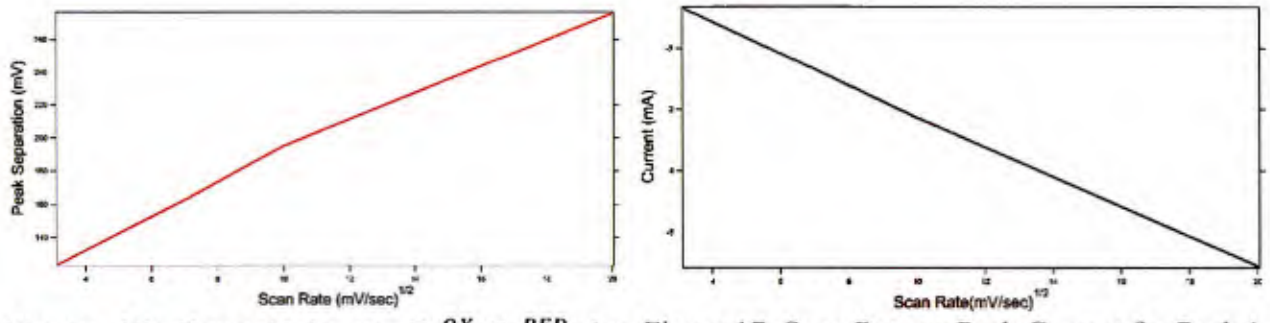

Figure 16: Scan Rate vs $E_p{}^{OX}$-$E_p{}^{RED}$ for Peak 1

Figure 17: Scan Rate vs Peak Current for Peak 1

Peaks 1, 2, and 3 are each 2 electron redox reactions.[70] The two electron nature of peak 1 was confirmed by exhaustive electrolysis a in both H-type and zero gap flow type electrochemical cells. The reactions are listed below.

Peak 1: $H_3PMo_{12}O_{40} + 2e^- + 2H^+ = H_5PMo_{12}O_{40}$

Peak 2: $H_5PMo_{12}O_{40} + 2e^- + 2H^+ = H_7PMo_{12}O_{40}$

Peak 3: $H_7PMo_{12}O_{40} + 2e^- + 2H^+ = H_9PMo_{12}O_{40}{}^{3-}$

Peak 1 has features of both reversible and irreversible waves. The reduction of peak 1 is linear with square root of scan rate, and $\frac{{I_p}^{OX}}{{I_p}^{RED}} = 1$; shown in Figure . The determination of ${I_p}^{OX}$ required the use of a potential hold at 0.4 V to remove the contribution of peak 2 from the resulting signal. Those are 2 of the 3 main criteria for reversibility. The remaining criteria is that the separation between the two peaks should be 59/n mV, independent of scan rate. The peak separation as shown in 17 is almost linearly dependent on square root of scan rate and is always greater than 59/n mV. Meeting some but not all of the tests for reversibility is evidence of quasi-reversibility. Peak 1 also shows a shift in the calculated E^0 of 10 mv, linear with square root of scan rate, from 424 mV to 432mV vs Ag/AgCl. To convert an Ag/AgCl reference electrode to NHE, add roughly 205 mV to the potential.

Peak 2 is significantly less well resolved than peak 1 yet still exhibits linearity of ${I_p}^{RED}$ vs square root of scan rate. Determining an acceptable value for ${I_p}^{OX}$ was complicated by the proximity to the other waves. The peak separation was strongly dependent on scan rate.

The kinetics of an electrochemical reaction can often be strongly affected by the heterogenous electrode surface. Metals in general are known to catalyze many electrochemical reactions. Precious metals often exhibit the highest electrochemical activity due to optimum binding strengths with important reactants. Platinum in particular is prized for its activity and stability in a variety of harsh reaction environments. To determine if the phosphomolybdic acid electrochemistry was different on platinum, CVs of phosphomolybdic acid were conducted on a platinum surface (Figure 18).

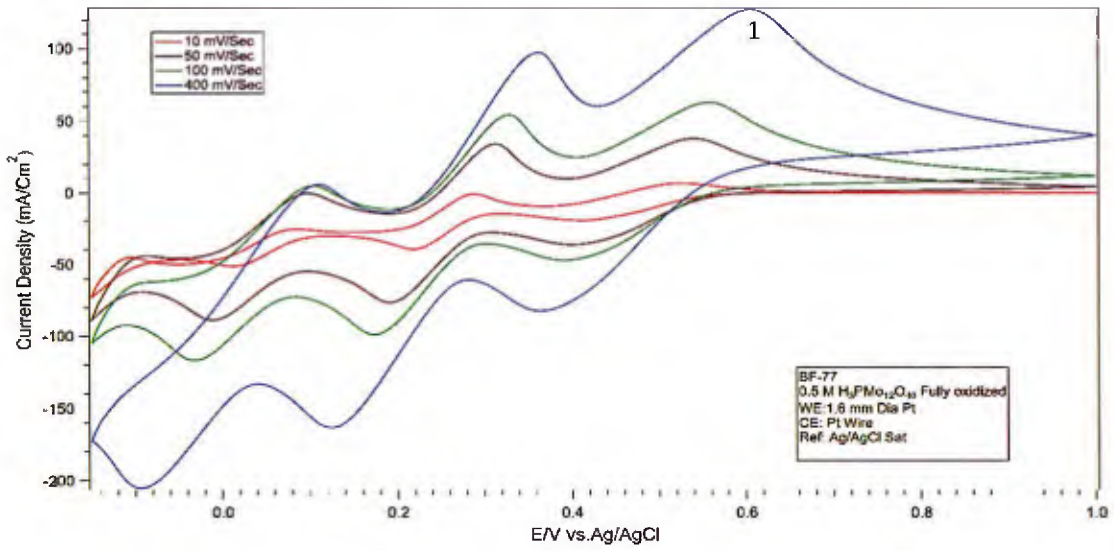

Figure 18: Cyclic Voltammetry of Phosphomolybdic Acid on Platinum. 0.5 M $H_3PMo_{12}O_{40}$, We: 1.6 mm Pt disk, Ce: Pt wire, Ref: Ag/AgCl (0.205 V vs NHE)

The voltammograms in Figures 16 and 18 exhibit remarkable similarities.

For peak 1 they share the linearity of peak heights with square root of scan rate, $\frac{{I_p}^{OX}}{{I_p}^{RED}} = 1$, and the dependence of ${E_p}^{Ox} - {E_p}^{Red}$ on scan rate. The peaks are slightly sharper and more resolved but still exhibit the same quasi-reversible features as the glassy carbon voltammograms, indicating that the platinum does not sufficiently catalyze the reaction to achieve reversibility.

An unexpected characteristic was noticed when preparing bulk reduced solutions for other experiments, cyclic voltammograms of bulk reduced phosphomolybdic acid are different in appearance from their fully oxidized counterparts. When a cyclic voltammetric scan is performed, the reaction occurs entirely within the boundary layer. This assumption is valid when the ratio of diffusion coefficient to scan rate is sufficiently low. At these scan rates the assumption is valid. This means that the ratio of ${PMo_{12}O_{40}}^{-3}{}_{\text{Bulk}}$ to ${PMo_{12}O_{40}}^{-5}{}_{\text{Bulk}}$ should have no effect on the cyclic voltammetric response after the first cycle.

To better understand this phenomena, solutions of phosphomolybdic acid were bulk reduced by 0 (Figure 14), 1 (Figure 18) and 2 (Figure 19) electrons. This bulk reduction was conducted using an H-cell and a large area platinum electrode. Cyclic voltammetry was then performed and the

results of the 6th cycle were used in the generation of this data. The first CV scan will often depend upon the solution redox state, but by the 6th scan the results will be stable.

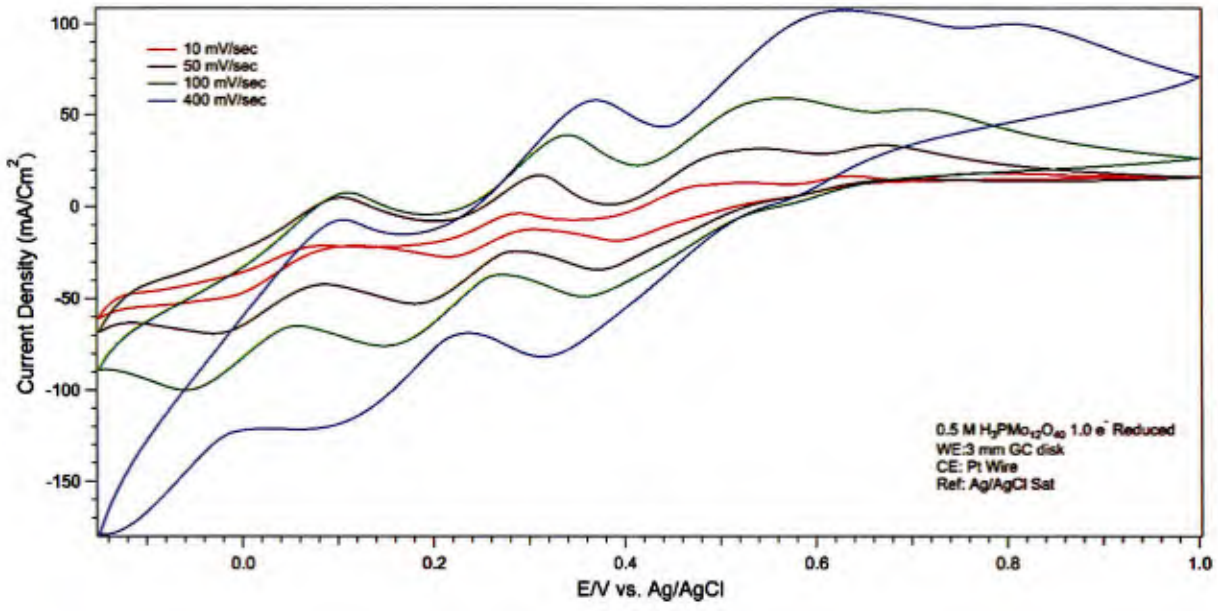

Figure 18: Cyclic Voltammetry of Phosphomolybdic Acid Bulk Reduced One Electron. 0.25 M $H_3PMo_{12}O_{40}$/0.25 M $H_5PMo_{12}O_{40}$, We: 3mm GC disk, Ce: Pt wire, Ref: Ag/AgCl (0.205 V vs NHE)

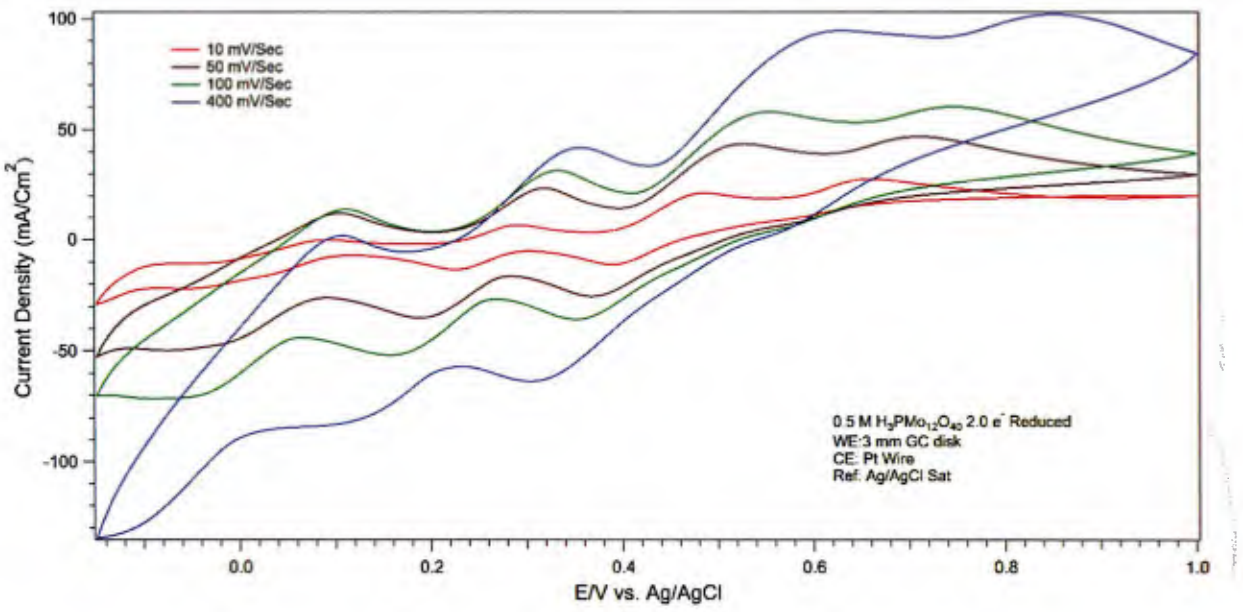

Figure 19: Cyclic Voltammetry of Phosphomolybdic Acid Bulk Reduced Two Electrons. 0.5 M $H_5PMo_{12}O_{40}$, We: 3mm GC disk, Ce: Pt wire, Ref: Ag/AgCl (0.205 V vs NHE)

We can see very little effect on the shape of peaks 2 and 3 from Figure . Peak 1 shows significant changes based on the ratio of ${PMo_{12}O_{40}}^{-3}{}_{\text{Bulk}}$ to ${PMo_{12}O_{40}}^{-5}{}_{\text{Bulk}}$. ${Peak_1}^{RED}$ gets slightly smaller but shows no change in shape. ${Peak_1}^{OX}$ begins to split into two separate waves at 0.55 V and 0.85 V vs Ag/AgCl. This change indicates the formation of a third species in solution but it must be occurring on a time scale longer than the characteristic time of the CV scans.

This type of reaction is known as an ECE reaction in electrochemical notation. E stands for an electron transfer step, C stands for a chemical step. What is believed to be occurring is that an electron is transferred to the POM complex, then a slow chemical step occurs in solution, then the newly formed chemical reacts on the electrode. This is competing with the 3 EE reactions which occur within each individual scan.

One possibility considered for explaining the peak splitting was that it was caused by hydrolysis of the phosphomolybdic acid on the surface of the electrode where it was being reduced. To better distinguish between this possibility and the ECE reaction hypothesis, we conducted cyclic voltammetry in a phosphomolybdic acid solution which was being reduced by glucose (Figure).

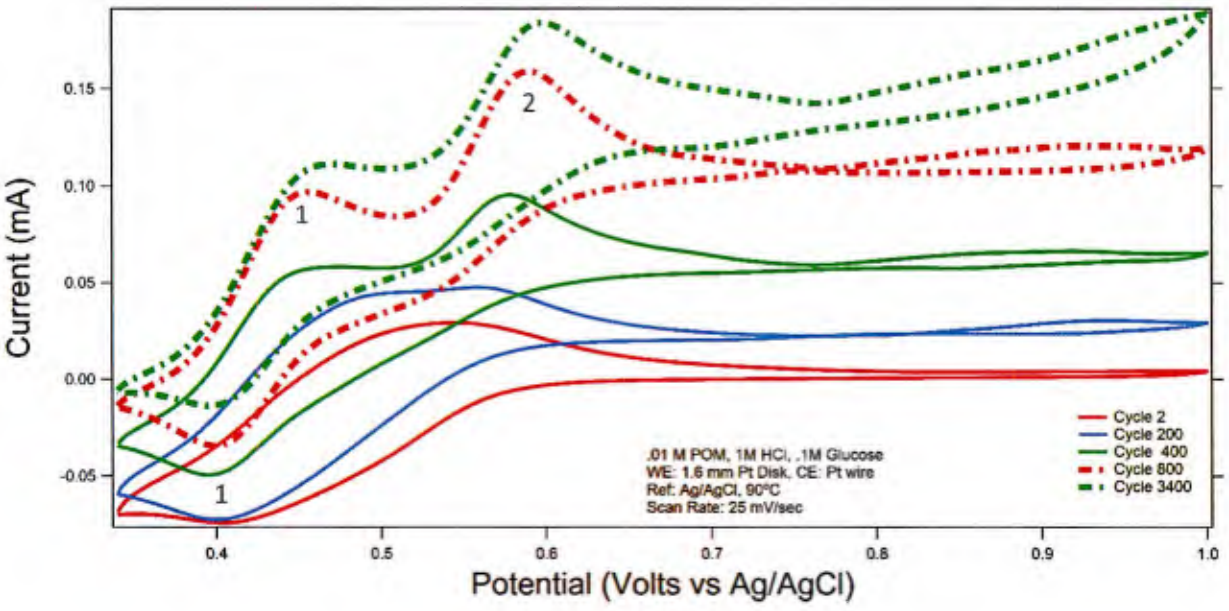

Figure 20: Repeated CV of Phosphomolybdic Acid During Bulk Reduction by Glucose. 0.01 M $H_3PMo_{12}O_{40}$, 1M HCl, We: 1.6mm Pt disk, Ce: Pt wire, Ref: Ag/AgCl (0.205 V vs NHE), 90°C, v = 25 mV/sec

Figure 20 demonstrates repeat cyclic voltammograms of a 90 °C mixture of phosphomolybdic acid, hydrochloric acid, and glucose. The experiment consisted of heating a single chamber containing the solution, a Pt working and counter electrode, and the reference. The potential was cycled between 0.3 V and 1.0 V vs Ag/AgCl to isolate peak 1 from Figure 18 and Figure 19. The phosphomolybdic acid was reduced chemically by the glucose during this period and experienced no bulk electrochemical reduction as was evidenced by integrating the current over all the cycles. The overall electrochemical charge transferred to the 25 ml solution was a 16 coulomb oxidation in 51 hours.

The 0.4 V reductive peak can be clearly identified in all of the scans although the peak height decreases with time and the peak begins to split, showing another potential peak near 0.5 V. The oxidative peak clearly splits with peak 1 showing a decrease in potential from 0.55 V to 0.45 V and peak 2 increasing in potential from 0.541 V to 0.6 V. Table 1 below shows the change in peak location as the solution is progressively reduced. Reduction peak 1 does not shift appreciably with the increasing concentration of the reduced species in the bulk. Oxidation peak 1 shifts closer to reduction peak 1 as the concentration of RED_{Bulk} increases, beginning to appear more reversible.

Oxidation peak 2 shifts in the other direction, away from both oxidation and reduction peak 1. This makes for a very clear split in the two oxidation peaks. There is a possible reduction peak forming at 0.55 V but it is unclear due to the background current.

What is clear from Figure 20 and Table 1 is that the phosphomolybdic acid peak does begin to split regardless of whether the solution is reduced chemically in solution as is done here or electrochemically as is demonstrated in Figure 19. This is further evidence that the reduced form of the phosphomolybdic acid is unstable in these conditions, either succumbing to its known hydrolytic instability or some other solution reaction. [70]

Table 1: Peak Height vs Scan Number

Cycle Number	Starting Time (h)	E_{RED}	E_{OX}-1	E_{OX}-2
2	0.0073	0.405	0.541	N/A
200	2.91	0.398	Not Identifiable	0.557
400	5.84	0.3952	0.459	0.5795
800	11.7	0.3989	0.458	0.5883
3400	51	0.396	0.471	0.597

To further confirm the bulk reaction hypothesis, we conducted the experiment from Figure 20 with no glucose added. This solution contained maintained its original state of charge throughout the experiment. Figure 21 shows the cyclic voltammograms of phosphomolybdic acid in hydrochloric acid on a platinum electrode. There is almost no change over 4000 cycles. This shows that the reaction causing the peak splitting is occurring in the solution rather than at the electrode since the peak splitting does not occur without bulk reduction.

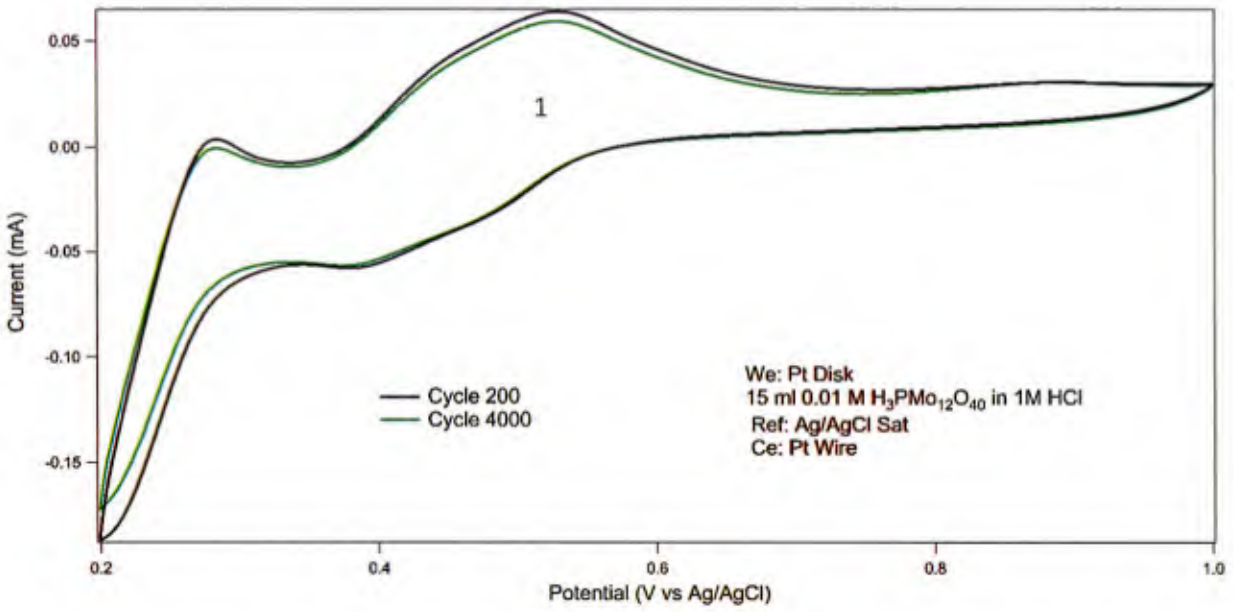

Figure 21: Repeated CV of Phosphomolybdic Acid. 0.01 M $H_3PMo_{12}O_{40}$, 1M HCl, We: 1.6mm Pt disk, Ce: Pt wire, Ref: Ag/AgCl (0.205 V vs NHE), 90°C, ν = 25 mV/sec

During various full scale experiments, the phosphomolybdic acid solution turned dark blue and would not reoxidize (indicated by turning yellow). Single compartment cyclic voltammetry experiments also exhibited unusual behavior, a dark blue compound diffused away from both electrodes during cycling. It became necessary to determine if the cause of this was related to a chemical irreversibility or contamination.

Potentiostatic coulometry (or bulk electrolysis) is a useful technique by which the state of charge of the entire solution can be controlled at will. The state of charge can be tracked by integrating the current (equation 4). The experiments take place on a longer time scale than most electrochemical experiments, enabling access to slower chemical steps. The most common metric for bulk electrolysis experiments in batteries is current efficiency at a given pair of potentials. Current efficiencies less than 1 are indications of irreversible reactions, although not necessarily of the intended compound. Imperfect current efficiency can be caused by side reactions at the electrode, instability of an active compound, solvent breakdown, or crossover of active species.

The afore mentioned H-cell was used for these experiments with a platinum mesh working electrode and stirring. To minimize the opportunity for contamination, the apparatus was designed

such that it is easy to confirm only glass, NAFION, platinum, and the reference electrode were in contact with the solution.

The solution was cycled a total of 60 times between 0.35 V and 0.8 V, isolating peak 1 from the previous figures. The initial capacity of 35 coulombs corresponds almost perfectly to 2 electron transfer, confirming the literature reports that peak 1 is a 2 electron transfer redox reaction.

The capacity starts at 35 coulombs and drops to 32 coulombs, a loss of 9% capacity over 60 cycles. The capacity fades and recovers several times although there is a general downward trend. After each cycle, the solution recovered its fully oxidized, pale yellow color. No crossover of phosphomolybdic acid was noted on visual inspection of the apparatus. This provided sufficient support to consider 2 electron reduction a safe 100% state of charge for battery experiments. It is possible and advantageous to reduce the solution further, but the stability of further reduction is not examined in this work.

Following the preliminary work above, 5 polyoxometalate and co-catalyst compounds in 3 supporting electrolytes were tested for activity in the oxidation of glycerol. Activity was generally ranked as Fe-$PMo_{12}O_{40}$ > V-$PMo_{12}O_{40}$ > $PWMo_{11}O_{40,}$ > $PMo_{12}O_{40}$ > TiO_2-$PMo_{12}O_{40}$ > Cu-$PMo_{12}O_{40}$. Supporting electrolyte activity was ranked as 5 M HCl > water > 5 M H_2SO_4.

Recent reports on the use of keggin ions to breakdown biomass molecules has inspired us to search for increased activity and additional biomass compounds to use as substrates. The current glut of glycerol from the biodiesel boom makes it a particularly attractive substrate. This reaction is to be tested in aqueous solution at low temperature to decrease the likelihood of forming toxic byproducts.

It has been shown that primary and secondary alcohols can be oxidized by polyoxometalate compounds in the presence of concentrated sulfuric acid. [2] The reaction mechanism is explored but the rates are not[4] Other researchers have used polyoxometalate compounds for the oxidation of starch and cellulose to power a fuel cell.[6] They studied the ability of different mediators and substrates to power a fuel cell but did not specifically look at the oxidation rates of those combinations. The literature also appears to be entirely lacking in hydrochloric acid based work, with all the research being focused on sulfuric acid or water based systems.

Here we report reduction studies of five biomass compounds in 3 supporting electrolytes. Fe-$PMo_{12}O_{40}$, V-$PMo_{12}O_{40}$, $PWMo_{11}O_{40}$, $PMo_{12}O_{40}$, TiO_2-$PMo_{12}O_{40}$, and Cu-$PMo_{12}O_{40}$ were tested in the electrolytes of 5 M HCl, water, and 5 M H_2SO_4. The reaction rate constants and reaction orders are examined.

Once it was determined that the kinetics of glucose oxidation by phosphomolybdic acid could not be readily studied with cyclic voltammetry, we conducted bulk oxidation experiments to understand the glycerol oxidation kinetics. Excess glycerol was placed in a sealed glass reactor with catalyst and thermostatted to 90 °C. The glass reaction chamber was connected to an electrochemical flow cell. The steady state current was recorded as R (equation 1). To increase signal, a series of reduction and reoxidation steps were performed.

The batch experiment is expected to be as pseudo first order since the experiment has excess substrate with the POM_{OX} concentration changing. In the continuous experiment, the substrate is supplied in great excess and the POM is being regenerated, this is a pseudo zeroth order reaction since none of the reagent concentrations are changing. The results of these two experiments are correlated later to help provide confirmation of results and to develop additional parameters.

1 $$R = K * [Substrate]^X * [POM_{OX}]^Y [Co - Catalyst]^z$$

The conversion of charge passed to moles is accomplished using the equation **2**.

2 $$Q = nFN$$

Where Q is charge passed in coulombs, n is the number of electrons per equivalent, N is the number of moles reacted, and F is the Faraday constant (96485 C/Mol). For consistency and ease of conversion we work in moles of H^+ or e^-, which directly translates to grams of hydrogen.

We compared the effect of several additives in either water, HCl or H_2SO_4. The presence of sulfuric acid has been shown to increase the rate and alter the mechanism (PC-ET to ET-OT) for the oxidation of the primary and secondary alcohols by polyoxometalates.[4]

Figure 22 shows the reoxidation profiles of several catalyst combinations in a solution consisting of catalyst, glycerol, and water. The copper and titanium dioxide solutions show a decrease in activity relative to the base line of the pure phosphomolybdic acid. They show far lower activity

than the pure phosphomolybdic acid for the oxidation of glycerol. The best performing combinations in this system are the iron and vanadium complexes. The reoxidation profiles of the iron and vanadium systems are such that they continue to show significant current for their entire reoxidation time. The other combinations undergo rapid reoxidation until they reach a steady state of low constant current. The pure phosphomolybdic acid, vanadium-phosphomolybdic acid, and phosphomolybdotungstic acid solutions show increasing levels of reduction with each increasing time step of 2, 4, 6, and 8 hours. The iron system approaches its maximum reduction by the second reduction step of 4 hours. The best of these systems still only yield about 70 Coulombs or 0.00073 g of hydrogen, in 10 hours.

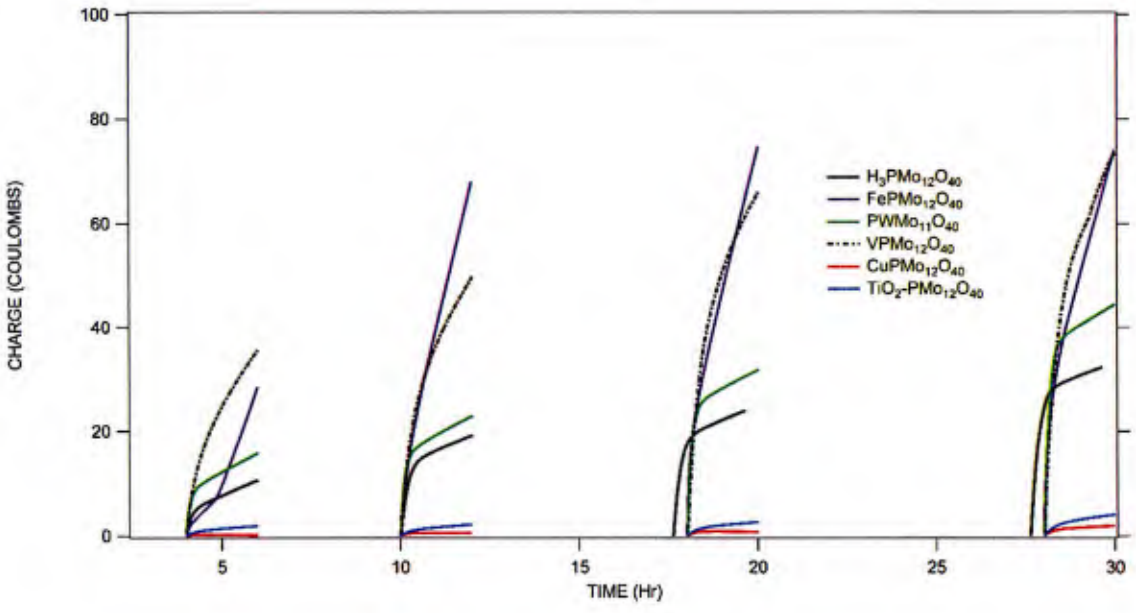

Figure **22**: Catalysts in 0.5 M Glycerol

The rates of glycerol oxidation presented in Figure… are insufficient for the development of a device. It has been suggested that the presence of sulfuric acid can catalyze the oxidation process two separate ways. Several authors discuss a change in the reaction mechanism from electron transfer to oxygen insertion in the presence of sulfuric acid.[4]

Another possibility is that at higher temperatures (above 50 °C), the mediators can react with water to produce a variety of oxidizing and super oxidizing compounds. Super oxidizers are species with

redox potentials greater than that of the Ce^{3+}/Ce^{4+} redox couple (1.7 V). For example, Fe(III) can be oxidized at the anode of an electrochemical cell to form the super oxidizer Fe(IV) as is shown in 3.

3 $$Fe^{3+} + 4H_2O \leftrightarrow FeO_4{}^{2-} + 8H^+ + 3e^-$$

Mediators can also react with anions in the solution such as $SO_4{}^{2-}$ to produce $SO_4{}^-$ radicals which are also powerful oxidizers.[5]

Figure 23 shows the oxidation profile of the catalysts shown in Figure 22 when exposed to 5 M sulfuric acid. All combinations tested are significantly less reactive in the sulfuric acid except for the neat phosphomolybdic acid which stayed roughly the same. The iron system was once again the most reactive although far less reactive than without the acid. It achieved a 10 hour reduction charge of roughly 45 coulombs The extended time period of elevated current for the iron and vanadium systems is no longer present. This could be due to improved electrode kinetics at lowered pH values. It could also be due to lowered reactivity with the glycerol substrate. The titanium dioxide and copper solutions once again provided little to activity. The vanadium system was the worst of the remaining combinations. All systems showed continued reduction across the increased time ranges. This indicates that they were not approaching the end of their ability to continue to oxidize the glycerol, this is due to their extremely low reactivity.

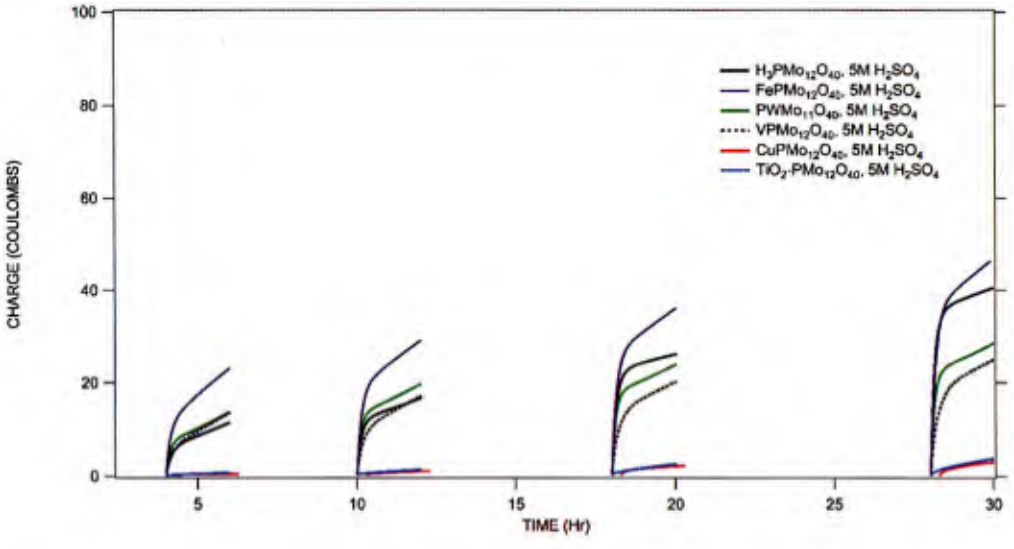

Figure **23**: Catalysts in 0.5 M Glycerol + 5M H_2SO_4

In the search for increased reaction rates, hydrochloric acid was also chosen to explore due to its ability to form various chloride radicals, similar to the iron and sulfuric acid systems. Figure 24 shows the reoxidation profiles of the selected catalyst combinations in 5 M HCl. It becomes immediately apparent that all the catalyst combinations offer improved performance in the presence of HCl versus neat or with sulfuric acid. Even the titanium dioxide and copper systems showed measurable activity in the presence of hydrochloric acid. In this case the copper showed the lowest activity and vanadium showed the highest. The iron system showed a cutoff at about 60 coulombs, similar to the 70 where it began to cutoff during the neat experiments. Here it reached the cutoff charge in 4 hours instead of 6 hours as in the neat system. The phosphomolydbdotungstic acid combination showed greatly improved performance in the presence of HCl. It rivaled iron within 6 hours and did not show the same type of cutoff as iron, gradually increasing to 82 coulombs in 10 hours.

The vanadium performance in HCl was the most promising with over 112 coulombs or .00116 g hydrogen in 10 hours. One possible explanation for this is that vanadium can form a variety of highly reactive vanadium chloride complexes in acidic conditions.[6]

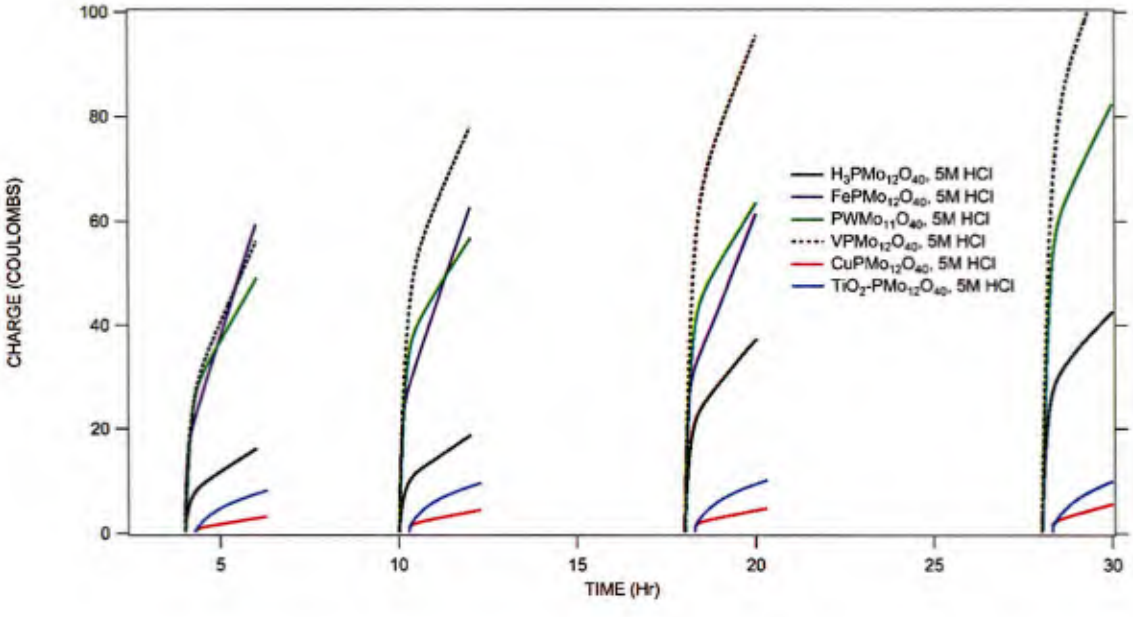

Figure 24: Catalysts in 0.5 M Glycerol + 5M HCl

After examining the above reoxidation profiles it was necessary to understand the influence of the abrupt decrease in current experienced shortly after each reoxidation step occurs. The charge to

current relationship is shown in equation 4. It is desirable to use a simplification of equation 4, shown in equation 5.

4 $$q = \int i\,dt$$

5 $$q = i_{final} * \Delta t$$

If this simplification holds, then i_{final} will be shown as a suitable surrogate for R in equation 1.

Figures 25, 26 and 27 show the total charge passed (Y-axis) the predicted charge from the i_{final} (X-Axis), effectively comparing equations 4 and 5. The final values lie along the red line when they are equivalent and the assumption holds. For reference 1 electron reduction per keggin unit corresponds to roughly 120 coulombs, 100% SOC as referenced in chapter 4 and 5 corresponds to 240 coulombs.

Figure 25 shows the comparison of predicted and recorded Q values for the 4-hour time step. That is 2 hours of chemical reduction, followed by 2 hours of concurrent chemical reduction and electrochemical oxidation. The simplification inherent in equation **5** appears valid for all samples except the $FePMo_{12}O_{40}$, $FePMo_{12}O_{40}$ – HCl, and $VPMo_{12}O_{40}$ – HCl. These are the samples showing the highest i_{final}. Interestingly, none of the samples except for the TiO_2-$PMo_{12}O_{40}$ outperformed the Q predicted.

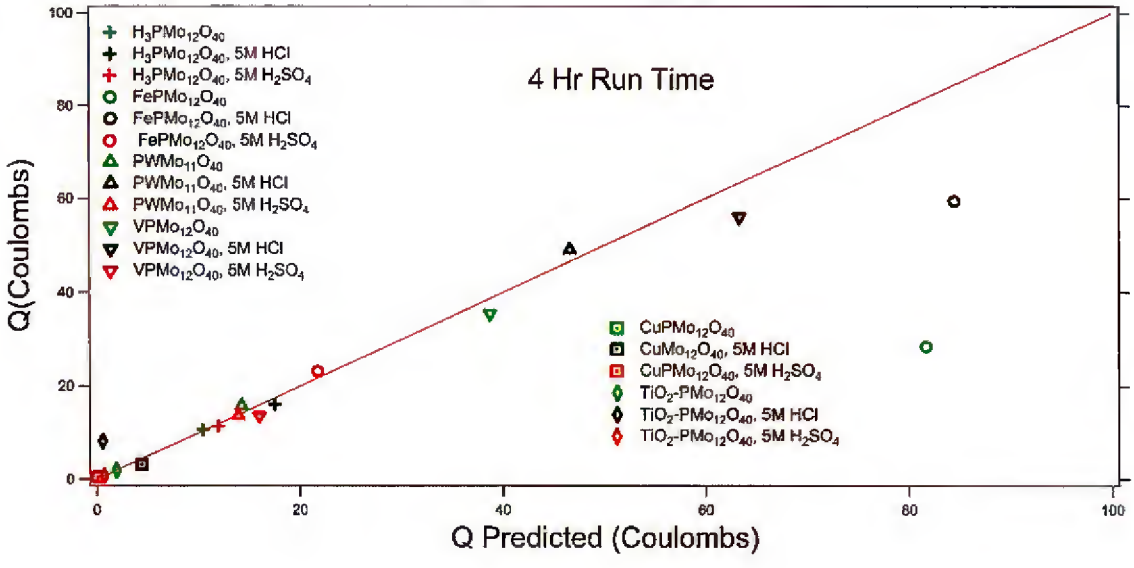

Figure **25**: 4 Hour Q Measured vs Q Predicted

Figure 26 shows the same comparison of the two Q values as before but with 4 hours reduction, followed by 2 hours of chemical reduction and electrochemical reoxidation. As before, the $FePMo_{12}O_{40}$, $FePMo_{12}O_{40}$ – HCl, and $VPMo_{12}O_{40}$ – HCl samples are showing significant differences between the predicted and experienced Q values. Additionally, $PWMo_{11}O_{40}$ – HCl is added to the list of samples which are showing this difference.

Figure 27 further shows this difference at the 8 hour mark, 6 hours of chemical reduction, followed by 2 hours of chemical reduction and electrochemical oxidation. By this point, the top 6 performing catalyst combinations are showing $Q_{predicted}/Q_{actual}$ far less than 1. Those samples are $FePMo_{12}O_{40}$, $FePMo_{12}O_{40}$ – HCl, $PWMo_{11}O_{40}$ – HCl, $PMo_{12}O_{40}$, $VPMo_{12}O_{40}$ – HCl, and $FePMo_{12}O_{40}$ – HCl. It can be reasonably assumed that all of these samples are now showing sufficient degrees of reduction to require the use of the full equation 1, rather than the simplified version.

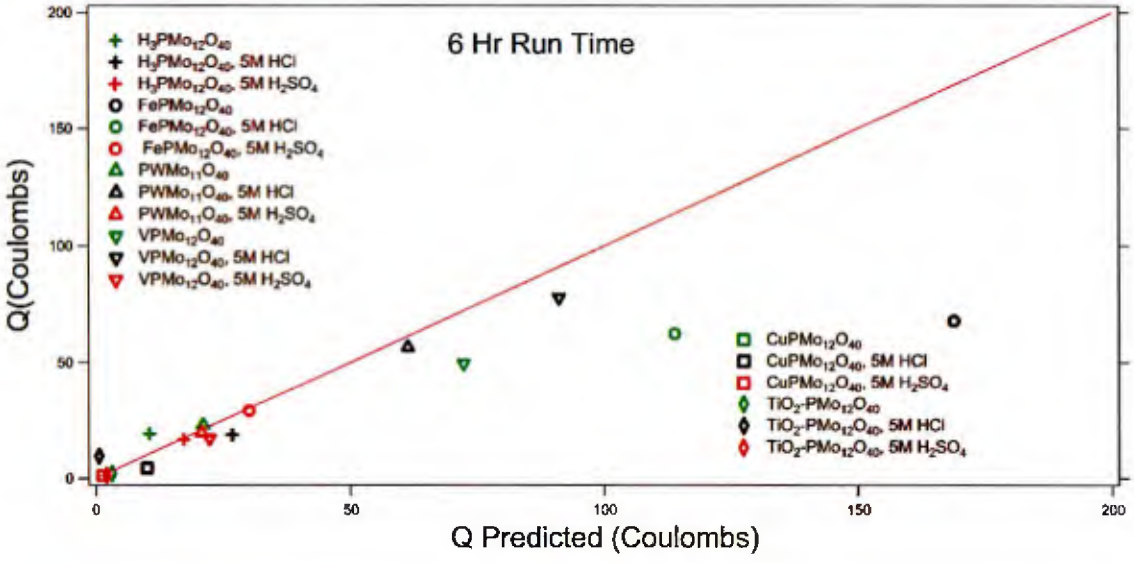

Figure**26**: 6 Hour Q Measured vs Q Predicted

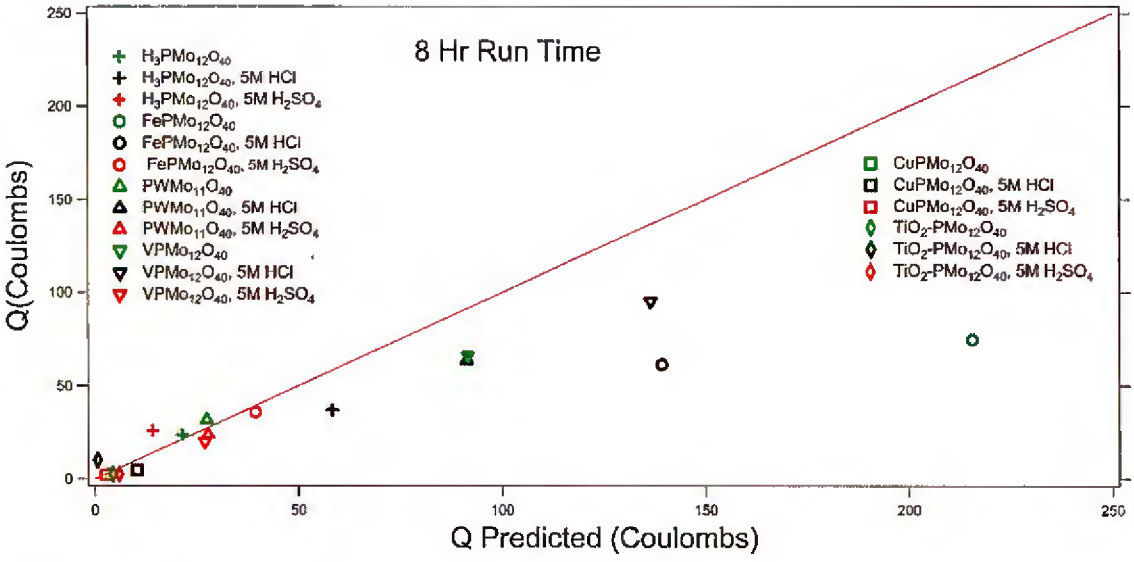

Figure 27: 8 Hour Q Measured vs Q Predicted

There are three hypothesized reasons for this consistent movement away from the 1:1 ratio of Q to Q-predicted with time. The first is the production of inhibiting products. Inhibiting products could be glycerol oxidation products or compounds formed by the reduction of catalyst complexes. A second is the reduction in the concentration of active catalyst species. The concentration of glycerol is not changing by more than 2.5% based on coulometry. The other likely explanation is that the electrochemical performance is too low to allow the samples to be fully reoxidized before reaching the end of the 2 hour oxidation period. This is unlikely since all samples returned to their initial color, indicating full reoxidation.

We believe that inhibiting glycerol oxidation products are likely not the culprit. The 4, 6, 8 ,and 10 hour steps were all run on the same solution, one after the other. The known glycerol oxidation products are not able to be electrochemically oxidized on carbon felt, so they would still likely be present after the electrooxidation phase. The cell appears to regenerate after each reoxidation step. A chemical study of the products in solution could be used to determine the presence of any inhibiting products and their activity on carbon felts in the presence of POM.

Liu showed the formation of starch-phosphomolybdic acid complexes (Figure 28). [3] Similar complexes with glycerol or glycerol oxidation products and phosphomolybdic acid may be hindering the reaction progress until they can be oxidized electrochemically. The other likely cause is that the quantity of oxidized phosphomolybdic acid is decreasing as it is reduced, this is linked

to the complexation possibility. They may show similar kinetic response, requiring spectroscopy to differentiate.

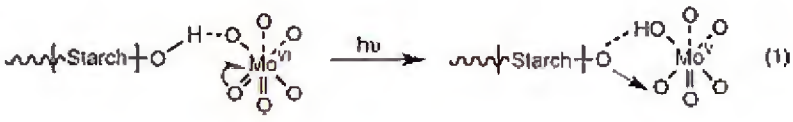

Figure 28: Formation of Starch-POM Complexes (Reproduced from Reference [3])

The purpose of Figures 25-27 is to assist in the understanding and selection of catalyst combinations. An ideal biomass oxidation catalyst has both the highest steady state current and the highest Q-transferred. The top performing catalysts in one metric are not necessarily the same as the top performing in the other metric. The choice of which metric to optimize depends on the intended mode of operation.

One proposed mode of operation is pulsed, based in response to electricity pricing. The solution reaction occurs in the presence of sunlight or waste heat for many hours, then a hydrogen tank is filled quickly when electrical power is cheap. This mode of operation favors the catalyst with the highest Q-transferred, namely the $VPMo_{12}O_{40}$ – HCl and $VPMo_{12}O_{40}$ based systems. The effectiveness of vanadium for this purpose may be due to vanadium storing additional charge which can be oxidized at the electrode?

A the continuous process has a higher conversion rate, for this process the higher I_{ss} and associated Q-predicted is preferable. The iron based systems appear to have the highest steady state currents at every time step. Iron has an important weakness as a catalyst, it is known to be unstable and destructive to NAFION membranes. For this reason iron systems may require a binder to control their activity. Amino acid complexes have been suggested as binders to control the iron activity.

To better understand the reaction rate, Figures 29-31 show the reaction rate vs electrons transferred. The Y axis represents the number of coulombs passed per hour over each time step. The X axis shows the number of electrons transferred. Electrons transferred can also be used as a proxy for time, when read from left to right, each marker represents the time points 4, 6, 8, and 10 hours respectively. This allows a subjective understanding of the cases where applying a rate equation will make sense. A more rigorous examination of the kinetics will occur in the next section.

Figure 29 shows this for the glycerol-catalyst combination with no supporting acid. As discussed previously, the iron and vanadium systems show the highest activity. The iron data is noisy but no system passes 0.65 electrons per keggin unit. The dependence of iron reaction rate on conversion appears unclear, unless the first (4hr) data point is erroneous. Iron experiences a sharp reduction in reaction rate around 0.65 electrons per keggin unit. The phosphomolybdotungstinic acid system is slightly more active than the phosphomolybdic acid only system, showing both a higher rate and a higher conversion. Only the Vanadium system shows an expected dependence of reaction rate on electrons transferred.

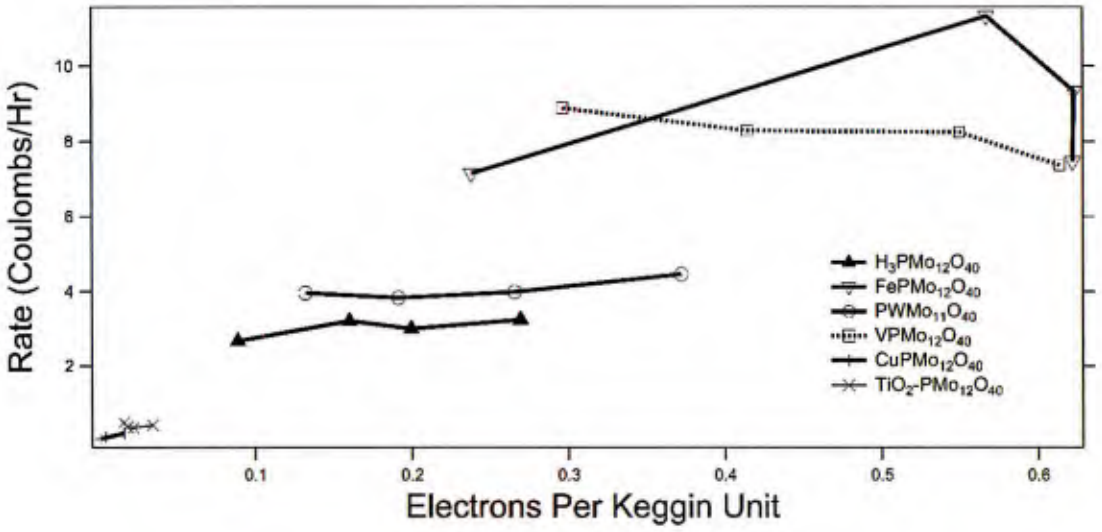

Figure **29**: Reaction Rate vs Electrons Transferred, Neat Solution

Figure 30 shows the reaction rate vs electrons transferred for the polyoxometalate-sulfuric acid systems. All combinations were notably less active when exposed to sulfuric acid. Here the highest activity catalyst by a large margin is the iron phosphomolybdate combination. The last data point was lost, but it outperforms the others in both rate and electrons transferred at every step recorded. The vanadium system underperforms in the presence of sulfuric acid. The pure phosphomolybdic acid-sulfuric acid combination performs quite well. Curiously, the reaction rate appears to increase with conversion. This could be due to sluggish electrode kinetics, causing incomplete reoxidation of the reduced catalyst in the electrochemical step. Once the number of electrons reaches a high enough level, then the reoxidation step may proceed at a higher rate. The vanadium, iron, and tungsten containing systems all appear to follow the expected trend of decreasing reaction rate with decreasing concentration of oxidized mediator.

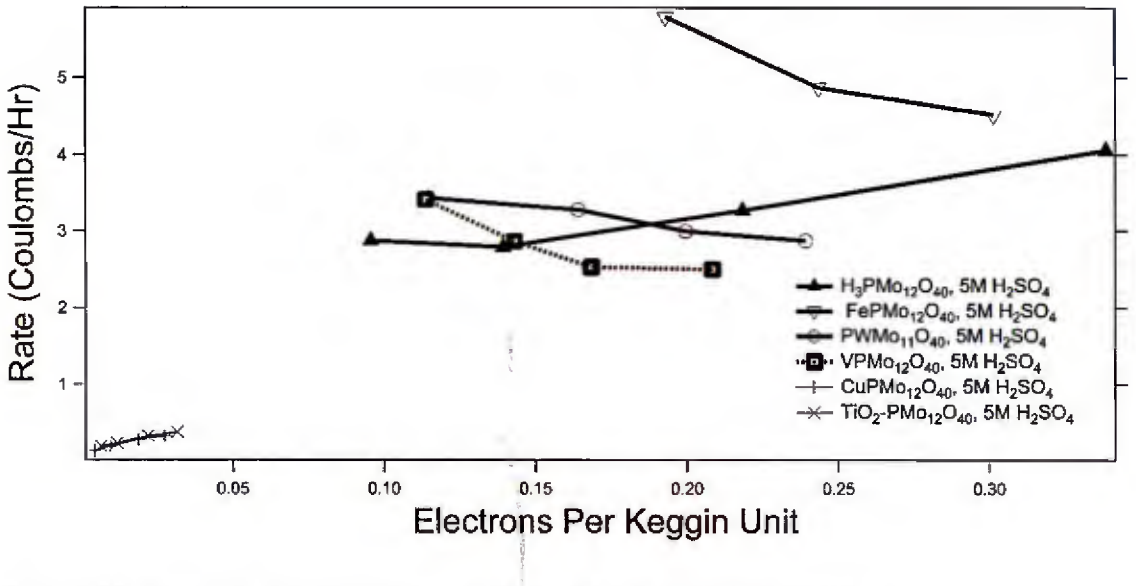

Figure **30**: Reaction Rate vs Electrons Transferred, H_2SO_4 Solution

Figure 31 shows the reaction rate vs electrons transferred plot for the hydrochloric acid-phosphomolybdic acid solution. Hydrochloric acid shows the highest activity of any combination tested. All catalysts showed higher reaction rates than in sulfuric acid or water. Vanadium showed the highest activity and a clear linear trend of decreasing activity vs electrons transferred. Iron showed the highest initial activity, then the activity sharply decreased around 0.5 electrons per keggin unit. The tungsten system exhibited a rapid but more controlled decrease in activity with electrons transferred. The pure phosphomolybdic acid system showed no clear trend of rate vs electrons transferred.

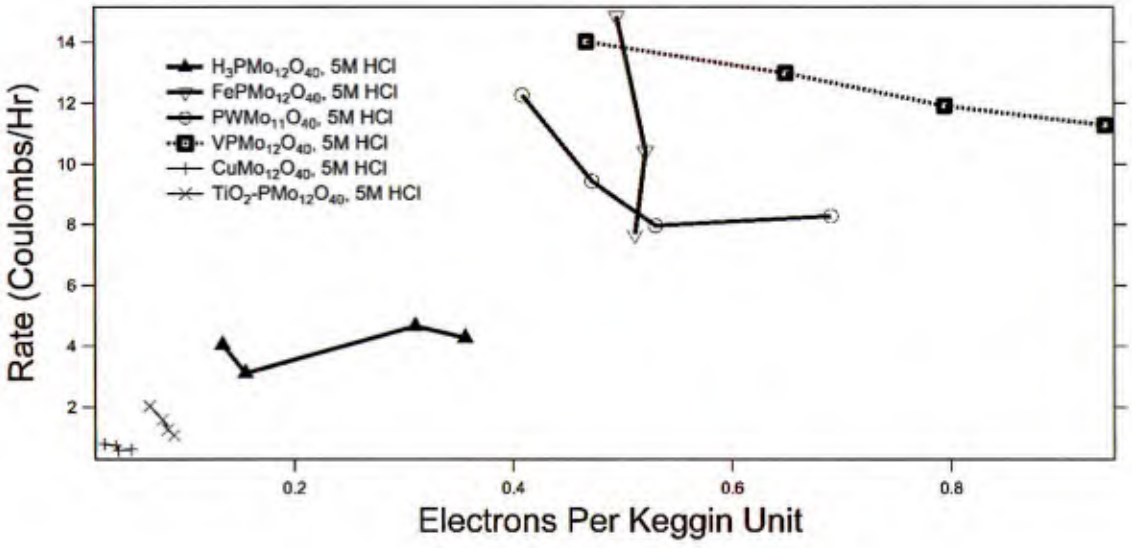

Figure **31**: Reaction Rate vs Electrons Transferred, HCl Solution

The experiment performed was designed such that the only reagent changing concentration significantly was the catalyst, the supporting acid and glycerol were supplied in large excess. The reaction reaction rate should only depend on the concentration of catalyst supplied, rolling the effects of the other reagents into the reaction rate *k'*. This is intended to enable discovery of the reaction order with respect to the catalyst. The experiment can then to be performed at a variety of concentrations for the other reagents. The *k'* values can then be plotted against concentration to determine k and the reaction orders.

Reaction order is determined tracking the change in concentration vs time. A zeroth order reaction shows no dependence of reaction rate on concentration, this can occur in systems where there is a limiting factor other than the reagents. Catalyzed systems where the catalyst surface is saturated are the most common example of such zeroth order reactions. It is unlikely that this system is zeroth order because there is no solid catalyst used. First order reactions show a linear relationship between reagent concentration and reaction rate. Vanadium appears to have this relationship in water and hydrochloric acid (Figures 29 and 31). Second order reactions show reaction rates proportional to the square of the concentration. This commonly occurs when two molecuules of the reagent are required to meet in time and space for the reaction to occur. From what is known about the mechanism of biomass oxidation by phosphomolybdic acid, this is unlikely.

Each reaction order will show linear behavior on a different representation of concentration and time. The slope of the appropriate linear plot is then used to determine the value of k'. Typical reaction rate laws and the appropriate linear plots for different reaction orders are given in Table 2.

Table 2: Reaction Order Equations and Plots

	Zeroth Order	First Order	Second Order
Rate Law	$\frac{-d[A]}{dt} = k$	$\frac{-d[A]}{dt} = k[A]$	$\frac{-d[A]}{dt} = k[A]^2$
Integrated Rate Law	$[A] = [A_0] - kt$	$[A] = [A_0]e^{-kt}$	$\frac{1}{[A]} = \frac{1}{[A]} + kt$
Linear Plot	[A] vs t	Ln([A]) vs t	$\frac{1}{[A]}$ vs t

Figures 32-34 show the R^2 values of the linear fits. This is done to determine which plot is most appropriate. When multiple reaction orders are linear, it is assumed that the reaction first order. This assumption is made because the reaction mechanism suggests first order kinetics.

The reaction is not assumed to be zeroth order. The different rates afforded by the different catalyst molecules chosen suggest a significant involvement in the reaction, making zeroth order kinetics less likely. It is expected that the extremely low reaction rates and corresponding extents of reaction will lead to high degrees of linearity. The degree of conversion may be further complicated by the continuing presence of reduced POM in solution. The 2/4 electron reduced POM couple is used by some similar systems for the oxidation of biomass. This means that the concentration of active species does not decrease linearly. The active species becomes reduced and forms a second active species, albeit likely one of reduced activity relative to the fully oxidized species.

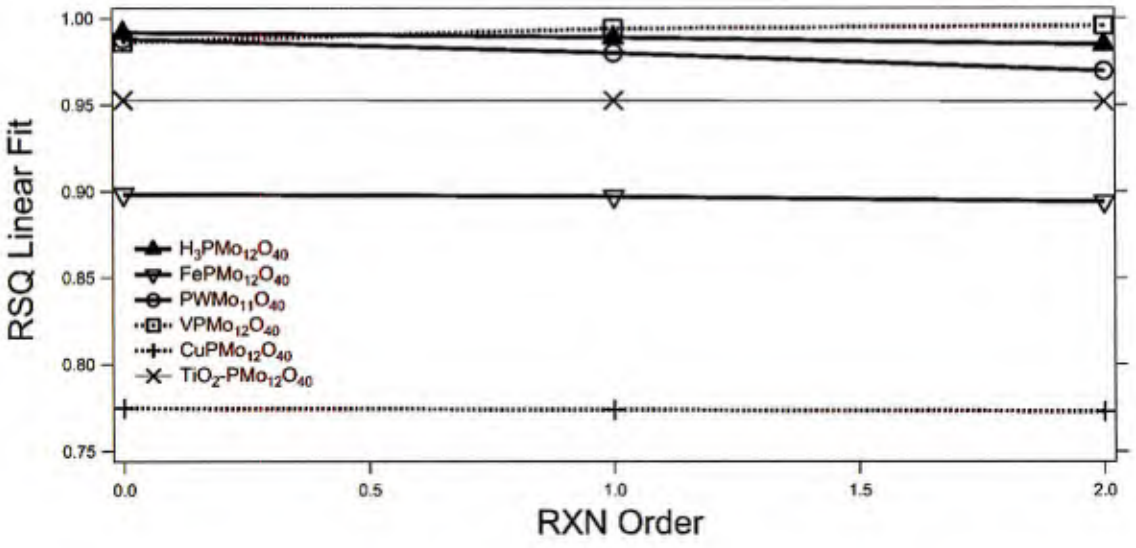

Figure **32**: R^2 for Linear Fit vs Reaction Order Plot-Neat

Figure 33 shows the R^2 of the sulfuric acid containing solutions. The pure phosphomolybdic acid system appears to be zeroth order, correlation decreases with reaction order. The iron system appears to be first order, The correlation is extremely low for the zeroth order plot (~0.2) and jumps up to almost 1 for first order plot.

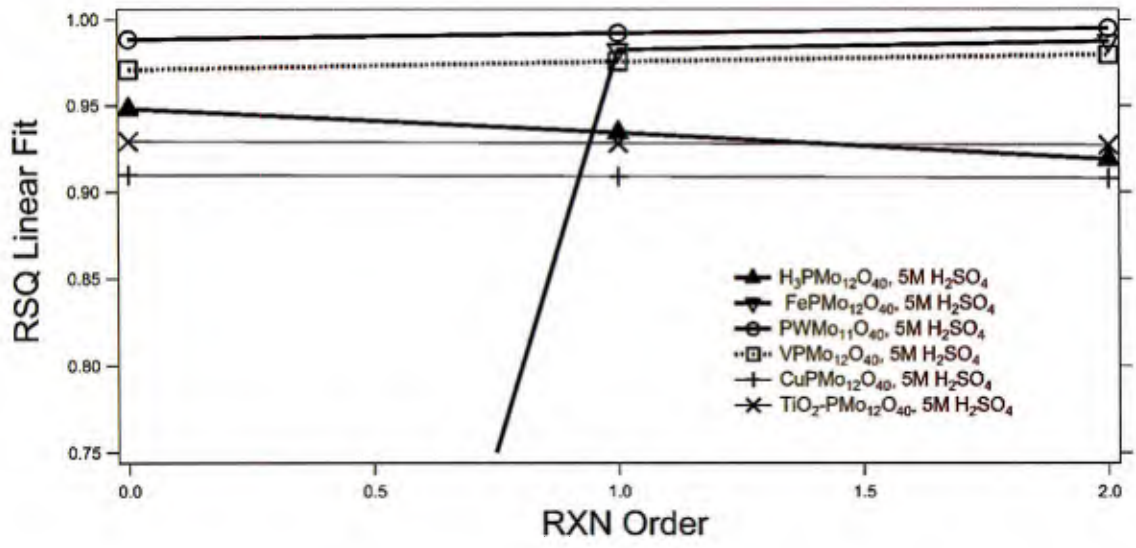

Figure **33**: R^2 for Linear Fit vs Reaction Order Plot-H_2SO_4

Figure 34 gives the R^2 data for the hydrochloric acid containing systems, the highest activity combinations tested. Again, the iron system is clearly first order with an extremely low correlation

(~0.2) in the zeroth order plot. The vanadium system exhibits a slight peak in the first order plot. The other systems can all be modeled as zeroth order or first order.

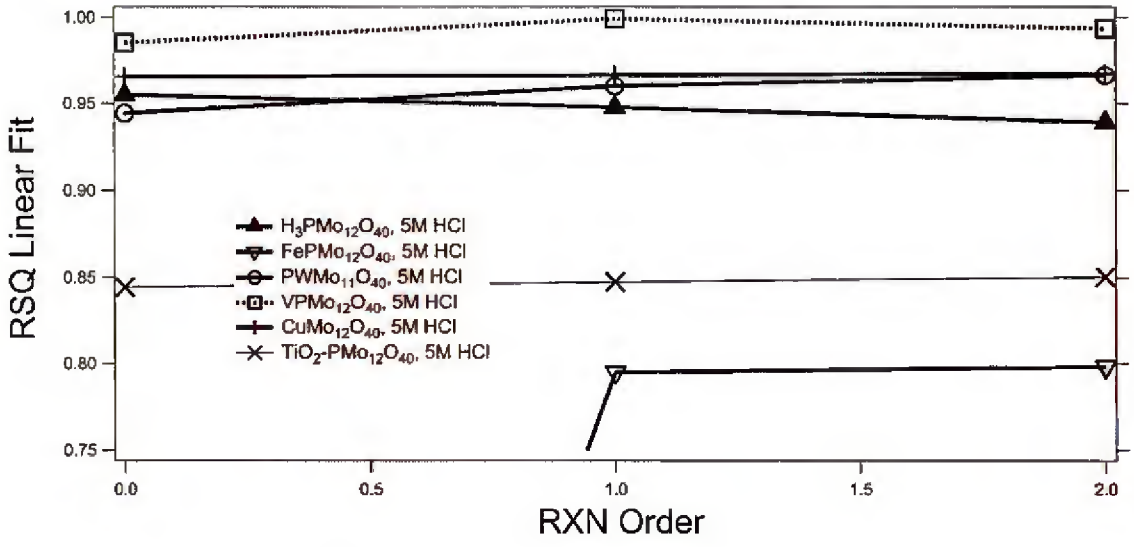

Figure **34**: R^2 for Linear Fit vs Reaction Order Plot-HCl

All of this is to suggest that a k' value can be calculated assuming the reactions are first order. Figure 35 gives the k' values for all catalyst combinations tested, note the units are 10^{-3} hr^{-1}. These are extremely low reaction rates. Further experimentation is still required to transform the k' values into k values. k values can be used with the rate equation to determine the size and concentration of reaction chambers necessary for given production rates of hydrogen.

Further optimization is likely possible, especially with respect to the catalyst POM ratios. It may be possible to do away with the expensive POM and use a larger ratio of the relatively inexpensive co-catalyst.

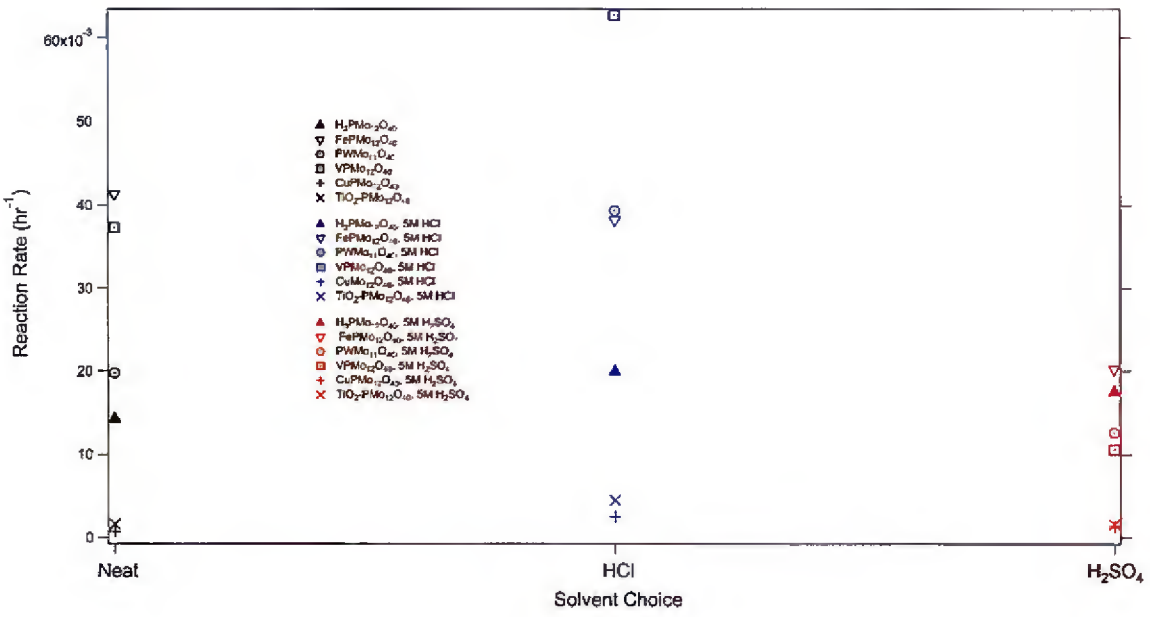

Figure **35**: k' Values for all solvent and catalyst combinations

Implications for Scale Up

Construction of hydrogen fueling stations is the definition of eventual success for the ideas presented in this work. The data presented in chapter 5 suggests that phosphomolybdic acid can be reliably oxidized in an electrolysis cell. The current densities shown will allow for reasonable stack sizes.

Stack construction is only half the chemical side of the proposed design. Determining the composition, size, and concentration of the chemical reduction chamber is also essential to understanding scale up feasibility. Hydrogen fuel cell vehicles travel roughly 70 miles per kilogram of hydrogen. According to the Federal Highway Administration, the average American drives roughly 13,500 miles per year. That means the average American would require 192 kg/yr or 0.022 kg/hr of hydrogen. The electrolytic production of hydrogen fuel will therefore require an average of 590 Amps current at all times per vehicle to be fueled. This is irrespective of what is being electrolyzed. This number creates great challenges and opportunities. Scaling up to the required size will be difficult and costly, but any voltage efficiencies gained will be multiplied over 590 Amps. Assuming 1.6 V for water electrolysis and 0.8 V for POM electrolysis the electrical demand is 944 Watts and 472 Watts respectively.

The highest steady state current achieved was 6.9 mA with POM concentration of 0.025 M, although concentrations of 0.5 M POM were possible. Assuming the reaction is first order in everything, 138mA are possible from a 0.5 M glycerol solution. 5M glycerol is also possible which would yield 1.38 A from a 50 mL reactor although the reaction order in glycerol is still unknown. In this ideal situation, a 56 gallon tank containing $3000 worth of molybdenum is required per vehicle. That is based on the molybdenum spot price of $15 per kg.

References for Section II.2

[1] Tsigdinos, G. A. & Hallada, C. J. Molybdovanadophosphoric acids and their salts. I. Investigation of methods of preparation and characterization. *Inorg. Chem.* **7,** 437–441 (1968).

[2] Liu, W., Mu, W. & Deng, Y. High-Performance Liquid-Catalyst Fuel Cell for Direct Biomass-into-Electricity Conversion. *Angew. Chemie* **126,** 13776–13780 (2014).

[3] Liu, W. *et al.* Solar-induced direct biomass-to-electricity hybrid fuel cell using polyoxometalates as photocatalyst and charge carrier. *Nat. Commun.* **5,** 3208 (2014).

[4] Sarma, B. B. *et al.* Polyoxometalate-mediated electron transfer-oxygen transfer oxidation of cellulose and hemicellulose to synthesis gas. *Nat. Commun.* **5,** 4621 (2014).

[5] Catalytic formation of carbon monoxide (co) and hydrogen (h2) from biomass. (2014).

[6] Carson, R. & Bremer, B. Mediated electrochemical oxidation process used as a hydrogen fuel generator. (2003).

II.3 Composite Catalyst Layers

In this study, a set of experimental techniques is adopted to characterize the fundamental properties of machine-prepared cathode catalyst layers (CLs) formed by different Pt to carbon (Pt:C) ratios, a highly graphitized carbon (EA carbon) and 3M ionomer (825EW) with a fixed ionomer to carbon (I:C) ratio. Scanning electron microscopy, transmission electron microscopy and Brunauer-Emmett-Teller nitrogen adsorption were conducted to investigate the CL microstructure including material dispersion and porosity. This analysis was performed on both the CL in an as-prepared condition and after being subjected to a standard Polymer Electrolyte Membrane Fuel Cell (PEMFC) testing protocol. The Pt:C ratio had a significant influence on the CL structure and transport properties. The lowest Pt:C ratio (30:70) exhibited a higher volume of secondary pores and higher proton conductivity over the whole relative humidity range. Such behavior can be associated with a more homogeneous ionomer distribution throughout the CL. The thin-film composite catalyst layer (CL) is a central component of proton exchange membrane fuel cells (PEMFCs). This layer, located at the electrode/membrane interface, comprises the region where the electrochemical reactions take place. Both the hydrogen oxidation reaction (HOR) and the oxygen reduction reaction (ORR) require a catalytic material to break the molecular bond of the diatomic gaseous reactant molecules, given the low-temperature conditions in a PEMFC.[1]

Platinum (Pt) and its alloys have prevailed as the PEMFC catalysts par excellence, due to their high activity towards both HOR and ORR, and their stability under standard operating conditions. However, the high cost and limited availability of the precious Pt metal set a cap on the maximum Pt loading for this technology to be economically feasible. The U.S. Department of Energy (DOE) established a 0.125 $g_{Pt} \cdot kW^{-1}$ total loading target at 150 kPa (abs) for a transportation PEMFC stack.[2] Such a balance between performance, durability and low Pt loading represents a challenge, especially on the cathode side, given the slower ORR kinetics. The CL design has undergone significant changes since the first-generation CLs that contained Pt black particles with polytetrafluoroethylene (PTFE) as the binder material.[3] The CL design typically used today corresponds to the thin-film CL system, which was proposed by Wilson and Gottesfeld in 1992.[4,5] This ionomer-bonded hydrophilic CL ensures a large contact area between the catalyst particles and the ionomer.[4] For such CLs, Pt utilization has been found to

be up to 45.4%, with very low catalyst loadings (0.12-0.16 $mg_{Pt} \cdot cm^{-2}$) and thicknesses (<10 μm).[6]

The effect of different levels of ionomer loading, particularly using Nafion®, has been widely investigated in thin-film CLs.[7-10] Studies have shown limitations in the CL proton conductivity (σ_{CL,H^+}) at low ionomer contents, which have been associated with the difficulty to form a continuous ionomer network.[10] On the other hand, an excess of ionomer can obstruct gas access to the reactive sites, hindering the reaction progress. Optimum Nafion loading in the CL has been reported to lie within the 30-40 wt.% range.[10,11] However, this value significantly depends on the carbon support structure.[12] Furthermore, the nanostructure of the ionomer can also be critical for the wide range of transport processes taking place in the CL. Although the perfluorosulfonic acid (PFSA) ionomer membrane structure have been extensively studied,[13] the properties of a confined thin-film ionomer are still not well understood. Several studies have shown that Nafion exhibits a heterogeneous distribution inside the CL with a 2-10nm thickness.[14] Such confinement can drastically affect the ionomer structure orientation and, therefore, the mechanisms of proton conduction and overall CL performance. Proton conductivity studies involving recast polymer films on a flat substrate have indicated intrinsic differences when compared to the bulk material.[15,16]

In the CL, the specific nanostructure is determined by the relative strength of interaction of the ionomer with the carbon, Pt or with itself; these are, in turn, related to the structure of the ionomer and its degree of functionalization with sulfonic acid groups. Indeed, some indications of specific adsorption of sulfonate groups on specific crystal faces of Pt have been reported. [17,18] This observation has led to widespread speculation that the sulfonate group interacts strongly with Pt particles in the CL, thereby 'poisoning' the Pt for ORR. Electrode performance is affected by several key properties of the ionomer component, such as conductivity and water uptake, which in turn are affected in various ways by the ionomer distribution.

Determining the ionic conductivity requires separating electronic and ionic contributions in the mixed conductor that is the composite CL. Ex situ measurements were first reported by Saab et al. using combinations of ionic and electronically conductive contacts to separate the two contributions.[19] Several studies investigating conductivity in situ have used a simplified transmission line model. [This approach, originally proposed by [20-22] Lefebvre et al. in 1999, uses a H_2-fed anode as reference and counter electrode and a N_2-purged cathode as working

electrode, thus eliminating the nonlinear charge-transfer resistances associated to the ORR. In the H_2/N_2 system, hydrogen evolution occurs at the H_2-fed counter/reference electrode, while the oxidation of the permeated H_2 occurs at the N_2-fed working electrode.[20] In subsequent work published by Liu et al., data acquisition was performed within the H-adsorption/desorption (HAD) region (~0.05-0.25V) to assure that the cathode capacity measurements are independent from the RH and frequency (up to 10kHz). The latter is guaranteed under the assumption that at low voltage perturbations, the HAD pseudocapacitance is constant up to a ~10kHz frequency. [20,23] Electrochemical impedance spectroscopy (EIS) measurements are carried out at a sufficiently high potential to ensure that the permeated-H_2 oxidation is permeation limited and, therefore, that the AC impedance signal is not influenced by the hydrogen crossover.

Water uptake (λ[=] mol H_2O/mol SO_3^-), defined as the number of water molecules per mole of sulfonic-acid groups, has also been the focus of numerous studies on the proton conducting membrane. Zawodzinski et al. investigated λ and transport properties of Nafion 117 membranes at 30°C, reporting λ=14 with the membrane exposed to saturated water vapor and λ=22 with the membrane immersed in liquid water.[24] Bai et al. studied the λ behavior of a series of 3M ionomer membranes including 3M's PFSAs with 825 equivalent weight (EW), which corresponds to the bulk membrane form of the ionomer used in the CL of this study. For the recast ionomer inside the CL, there is strong evidence that transport and morphology differ from the bulk membranes. [15,16] Siroma et al. reported the conductivity of a Nafion thin-film of about 100nm thick was about an order of magnitude less than that of bulk material.[16] Also, the thin-films showed a higher activation energy for proton conduction, suggesting an intrinsic change as the ionomer thickness decreases. Concurring with Siroma's study, the proton conductivity of the CL has been reported to be an order of magnitude smaller than the bulk membrane.[25]

Water adsorption and transport in Nafion thin-films have also been examined by several studies. [26-29] Sun et al. studied water uptake and transport of water within homemade CL films. [30] Using a combination of NMR probes reporting on local (relaxation) and long-range (PGSE Diffusion), they concluded that in the low-water content regime the local environment for water hydrating the sulfonate groups is essentially the same in the CL while longer range diffusion is strongly dependent on water content and decreases dramatically as water content decreases. The latter decrease is much stronger than in a membrane. This observation, taken together with the

likelihood that all water at low water contents is associated with sulfonates, suggests that decreasing hydration breaks up the connectivity of the ionomer network in the CL. Eastman et al. studied swelling (defined as the change in dimensions to accommodate adsorbed water molecules), water solubility and transport kinetics of adsorbed Nafion films thinner than 222 nm as a function of RH. [31] The equilibrium water adsorption was analyzed using specular X-ray reflectivity (SXR). In this study, films with a thickness below 60 nm exhibited lower water uptake, which was further verified with quartz-crystal microbalance analysis. These effects were attributed to the macromolecular and morphological confinement of the Nafion thin-film. A model based on neutron reflectivity was utilized to confirm that the confinement effect is associated with the Nafion film, and not with the silicon substrate. Results from small angle X-ray scattering under grazing incident angles (GISAXS) suggested that the ionic domains could construct a more ordered structure as the thickness increased. However, we note that these findings must be applied with some caution. The carbon or Pt on which the ionomer is adsorbed in the real system is highly rough and the surface morphology plays a role in 'templating' the resulting ionomer ordering.

Unlike the bulk ionomer membrane, the ionomer in the CL also must be permeable to gases. Reactants must be able to diffuse through the thin-film ionomer layer to reach the catalytic reaction sites. Therefore, gas permeability through ionomer thin-films has been an important research focus. Permeability is the product of solubility and diffusion of the gas, oxygen, through the ionomer. [32] PFSA ionomers exhibit higher permeability than hydrocarbon ionomers. [33] In this work, we seek to further understand the ionomer distribution and its effect on the CL properties. We present detailed characterization of a CL prepared by an industrial process (3M), as opposed to handmade catalysts from inks and decals. Unlike the many model studies or studies that use a 'homemade recipe', we are able to present detailed data for a realistic CL for a range of compositions. These films are specially prepared as free-standing films and are composed of a highly graphitized carbon (Tanaka EA-type carbon) and 3M ionomer (825EW) with a fixed ionomer to carbon (I:C) ratio. Analysis was performed on the CL in an as-prepared condition and after being subjected to a standard PEMFC test protocol. Scanning electron microscopy (SEM), transmission electron microscopy (TEM) and Brunauer-Emmett-Teller (BET) nitrogen adsorption were conducted to investigate the microstructure including material dispersions and porosity. The water uptake and conductivity were determined for each Pt:C ratio

as a function of relative humidity. This analysis provides insight into the ionomer distribution and the carbon-ionomer interaction.

Free-standing machine prepared CLs with different Pt:C ratios were provided by 3M for this study. The electrodes provided were composed of Pt-supported Tanaka EA-type carbon and 3M ionomer (825EW). The EA-type carbon is a graphitized Ketjenblack (KB) EC600JD carbon. The unmodified KB EC600JD is a high-surface area (~1400 $m^2 \cdot g^{-1}$ BET area) carbon black material. In general, carbon black materials exhibit a bimodal pore size distribution, which includes the so-called primary pores (2-20 nm diameter) located within agglomerates of carbon particles and secondary pores (>20 nm diameter) between aggregates of agglomerated KB. [14,32,34,35] KB carbon, in particular, also exhibits a significant fraction of micropores (<2 nm) compared to other widely used carbon black materials such as Vulcan XC-72.[34] Although KB carbon is nominally non-graphitized, primary KB carbon particles display a meso-graphitic structure at/near the outer surface. [12,36] Further graphitization, usually achieved by applying high current densities or temperatures (>2500 °C), have a positive effect on the resistance of the material to electrochemical corrosion and, therefore, its durability. [37, 38]

Three sets of free-standing CLs were provided as 15x30 cm thin electrode sheets, loosely supported on a paper liner for easy detachment. The general properties of these samples are shown in Figure 36; all sets were prepared with a 0.25 $mg_{Pt} \cdot cm^{-2}$ loading, 1.0 I:C ratio, and 30:70, 50:50 and 70:30 w/w Pt:C ratios. A more uniform and homogeneous electrode area can be guaranteed through this fabrication technique in comparison with handmade CLs. Free-standing CLs were used instead of a catalyst coated membrane to allow the ready application of certain experimental methods that can be affected by the membrane contribution. In particular, BET and microscopy measurements are easier when using the free-standing samples.

Physicochemical Characterization

Transmission Electron Microscopy. Typically, TEM has been conducted on powders scraped from the electrodes with the main objective of characterizing the electrocatalyst. [6, 39, 40] However, this methodology is not able to provide information on the overall CL structure, given the loss of spatial integrity. [41] In contrast, standard diamond-knife cutting of epoxy-embedded membrane electrode assemblies (MEAs) allows for the structural preservation and for the cross-section visualization of the CL.[42]

Samples for this study were prepared through both scraping and epoxy-embedding techniques, as described below:

- Scraping: The catalytic material was scraped from the freestanding electrodes to visualize the electrocatalysts material. The scraped material was then dispersed in methanol, and a drop of this suspension was placed on a 300-mesh copper grid.
- Epoxy-embedding: A small piece of the MEA was removed and embedded in an epoxy resin. Samples were then microtomed at room temperature using a Leica UCT. Araldite was used as embedding material and it was polymerized at 60°C for 24 hours in a vacuum oven.

All samples were examined in a Hitachi HF-3300 300 kV TEM/STEM (scanning transmission electron microscope), with a cold-field emission gun and 0.12 nm imaging resolution. This technique allowed characterization of the microstructure of the CLs in terms of Pt size distribution, and carbon support structure.

Pt Size Distribution. Given the high atomic number of Pt and the contrast differences with the other CL components, it is possible to evaluate Pt sizes and distributions from the TEM images. For this purpose, many TEM images from different areas of both fresh and post-operation CLs were acquired. ImageJ® was used to manually count the individual particles, guaranteeing that a large number of particles (>1000) was counted in each sample.

This parameter was analyzed for both fresh (pristine) and post-FC operation electrodes, to study the changes that the electrode undergoes during standard operation. The Statgraphics® software was used to process the results obtained. To compare and study the statistical distributions, two shape parameters were calculated: standardized skewness and standardized kurtosis.

The standardized skewness (z_1) is a measure of the asymmetry of the data distribution, calculated according to Equation 1: [43, 44]

$$z_1 = \frac{\frac{n\sum_{i=1}^{n}(x_i - \bar{x})^3}{(n-1)(n-2)s^3}}{\sqrt{6/n}} \qquad (1)$$

Where n is the number of observations, x_i is the i^{th} observation, $\bar{x}$ is the average or arithmetic mean, and s is the standard deviation. Positive skewness indicates a longer upper tail than lower, while negative skewness indicates a longer lower tail. At the 5% significance level, significant skewness could be asserted if the value of z_1 falls outside the interval (-2, +2).

The standardized kurtosis (z_2) is a measure of the relative peakedness or flatness compared to a normal (bell-shaped) curve: [43, 44]

$$z_2 = \frac{\frac{n(n+1)\sum_{i=1}^{n}(x_i - \bar{x})^4}{(n-1)(n-2)(n-3)s^4} - \frac{3(n-1)^2}{(n-2)(n-3)}}{\sqrt{24/n}} \quad (2)$$

A value close to 0 corresponds to a bell-shaped normal distribution. A positive z_2 value corresponds to a distribution that is more peaked in the center and has longer tails than the normal; whereas a negative z_2 value indicates a flatter distribution than the normal with shorter rails. At the 5% significance level, significant kurtosis could be asserted if z_2 fell outside the interval (-2, +2).[45]

X-Ray Diffraction (XRD). The XRD patterns of the samples were measured with a Bruker D2 Phaser diffractometer with Cu Kα radiation. The well-known Scherrer equation (Eqn. (**3**)[46]

$$L = \frac{K\lambda}{\beta\cos\theta} \quad (3)$$

was used to calculate catalyst particle size:[46]

$$L = \frac{K\lambda}{\beta\cos\theta} \quad (3)$$

In this equation, L is the mean size of the crystalline domains, K is a numerical factor that depends on the actual shape of the crystallite and β is the half-value breadth of the diffracted beam.

Gas Sorption Technique. To further study the structure of these materials and obtain information on the pore structure, the nitrogen (N_2) adsorption technique was used. The surface area and the pore size distribution (PSD) of the catalysts were measured and. BET and Barrett-Joyner-Halenda (BJH) Pore Size ND Volume Analysis were employed to analyze data.

Water Uptake (λ) Measurements. To perform λ measurements in the free-standing electrodes, each electrode was transferred onto a Kapton® film. The purpose of this transfer was to provide mechanical stability to the thin electrodes. All samples were hot-pressed at 120°C for 15 min. Then, the CL/Kapton system was dried by suspending it over a volume of phosphorous pentoxide (P_2O_5) for a period of 7 days. The dried samples were suspended over lithium chloride (LiCl) solutions with different concentrations over 7 days. Excess water was removed with the

aid of Kimwipes. After reaching equilibrium, the final weight of the sample (W_{wet}) was registered.

Electrochemical Impedance Spectroscopy (EIS). This technique has been developed elsewhere and is particularly useful for in situ CL proton resistance measurements.[35] For this experiment, membrane electrode assemblies (MEAs) were prepared by hot-pressing the freestanding electrodes at one side of a Nafion 212 membrane at 140°C for 10 min with a 1000 kg load. Subsequently, an in-house prepared anode electrode was hot-pressed to the other side of the membrane, along with a gas diffusion layer (GDL) against the cathode side.

The in-house anodes were prepared by mixing 10 mg of 30:70 w/w Pt:C Tanaka® catalyst powder, with 1 ml of isopropanol and 122 mg of 5 wt. % Nafion solution. The ink was sprayed onto a 5 cm^2 GDL using an airbrush. Ink was sprayed onto the substrate until a 0.2 $mg_{Pt} \cdot cm^{-2}$ catalyst loading was reached. GDLs made of carbon paper with a carbon coating (SIGRACET® Gas Diffusion Media, Type GDL 25 BC) were used for both electrodes. The σ_{CL,H^+} can then be calculated from the Nyquist plot, typically exhibiting two characteristics behaviors: a 45° angle region at high to intermediate frequencies due to proton resistance in the CL and a 55-90° angle in the lower frequency region representing the CL capacitance and resistance. [21, 32, 35, 47] The CL proton resistance, R_P, can be obtained from the extrapolation of both slopes to the real impedance axis. [32, 35, 47]

$$\mathbf{R_P = 3(Z'_{LF} - Z'_{HF})} \qquad (5)$$

Where Z'_{LF} and Z'_{HF} correspond to the low and high-frequency intercepts at the real part of the impedance, respectively. These measurements were averaged over 3 repetitions.

For these measurements, we used the same system described in the polarization curves section. After acquiring the polarization curves, the cell was changed to the H_2/Nitrogen(N_2) system and was held at OCV and 60% RH for a 1-2 h period, to eliminate O_2 gas from the pipelines and cathode compartment. EIS measurements were then performed at the same RH range used for polarization experiments. The frequency ranged from 0.5 Hz to 20 kHz with a 0.03V perturbation. H_2 and N_2 gases were both fed at 100 $mL \cdot min^{-1}$, and the cell was held at 80°C and 0.2V. After each RH shift, the cell rested for 45 min at OCV to reach equilibrium before data acquisition.

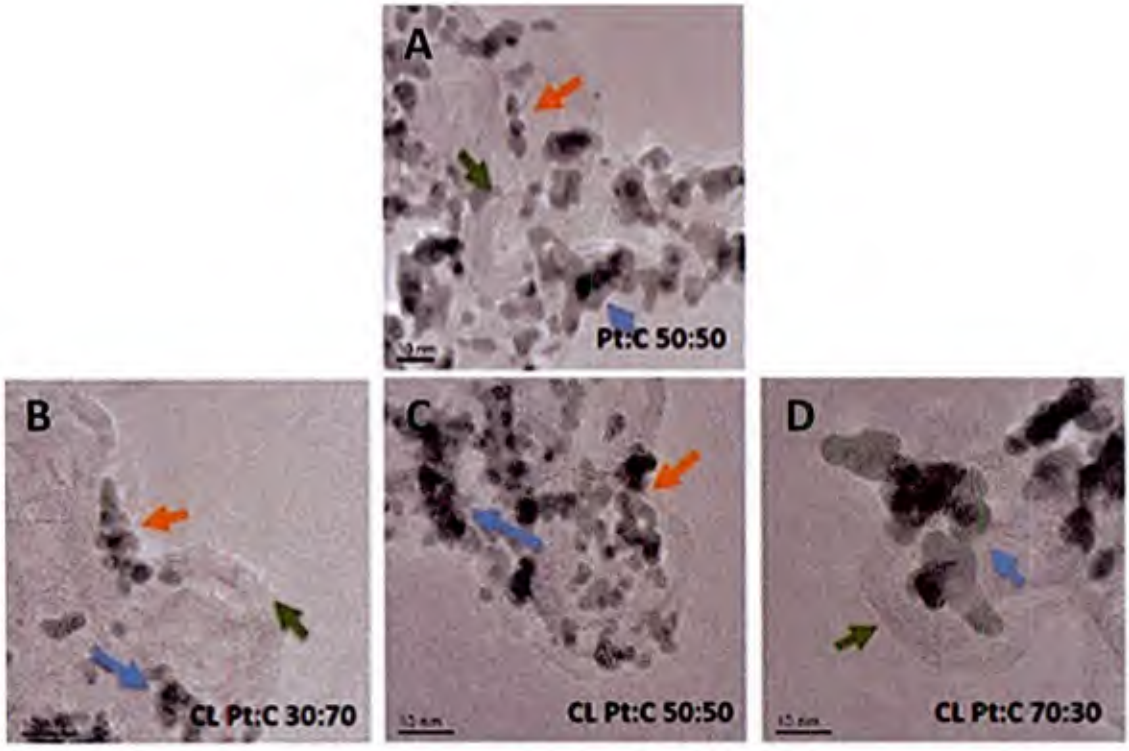

Figure 37. TEM images of 50:50 Pt:C catalyst powder (A), and the scraped 30:70(B), 50:50(C) and 70:30(D) Pt:C machine-prepared free-standing electrodes showing Pt particle accumulation around the graphitic planes of the carbon support.

To probe their structure and function, the CL samples of varying composition were characterized using the physical and electrochemical methods described.

Physicochemical Characterization

Microscopy Characterization. TEM images are shown in Figure 37 for the 50:50 Pt:C ratio catalyst powder (Figure 37a) and the set of CLs with 30:70 (Figure 37b), 50:50 (Figure 37c) and 70:30 (Figure 37d) Pt:C ratio prepared through the scraping technique. The characteristic planes and facets of the graphitic carbon support can be observed in all cases (green arrows in Figure 37). Preferential Pt deposition in the carbon structure defects (orange arrows in Figure 37) lead to a heterogeneous Pt particle distribution throughout the carbon structure and to larger Pt particle agglomeration (blue arrows in Figure 37). The agglomeration effect becomes more significant as the Pt:C ratio increases.

To obtain CL cross-sectional specimens, the "full-embedding" ultramicrotomy technique was employed for both "fresh" and post-operation samples.[41,42] To obtain the "fresh" samples, small

sections of the freestanding electrodes were hot pressed to a Nafion 212 membrane section to guarantee similar conditions to that of the post-operation cathode. These sections were embedded in an epoxy resin and then sectioned with a diamond knife on an ultramicrotome, as described previously.

Figure 38 shows representative TEM images of the 30:70, 50:50 and 70:30 Pt:C fresh electrode samples. It is useful to keep in mind what is not detectable in these images. The carbon structure is not as defined in these images as it was in F Figure 37 given the epoxy coverage throughout the sample. The presence of the epoxy also prevents the identification of the ionomer phase in these samples. Thus, several key aspects of the puzzle that is the CL, such as the internal structure of the carbon particles and the disposition of ionomer, are not readily visible. The 70:30 Pt:C sample has larger Pt particle sizes and a larger proportion of uncovered carbon areas, as observed in Figure 38C and F, in comparison to the samples with lower Pt:C ratio. Significant Pt particle agglomeration is observed with both the higher Pt:C ratio (50:50 and 70:30 Pt:C) samples.

Pt Size Distributions. Histograms of particles sizes from samples with different Pt:C ratios are shown in Figure 39. None of the fresh sample observations can be identified as normal distributions of particle size. Therefore, a robust statistical method is necessary to enable comparison of these samples. In this case, the Kruskal-Wallis (KW) test was found to be suitable, given the non-normality of the data and the existence of outliers in all samples. [48] Through this analysis, we concluded that there is a statistically significant difference amongst the medians of the fresh 30:70, 50:50 and 70:30 Pt:C ratio sample at the 95% confidence level. The calculated average Pt particle sizes are 3.5, 3.2 and 5.2 nm for the 30:70, 50:50 and 70:30 Pt:C fresh samples, respectively. The average Pt particle size is significantly higher for the highest Pt:C ratio (70:30), which is consistent with the larger agglomeration that is qualitatively observed in the TEM images in Figures 37 and 38. The 50:50 Pt:C ratio exhibited the lowest average Pt particle size. This trend was also confirmed through XRD. Particle diameters calculated from the Pt (111) peak exhibited the same trend observed from the TEM

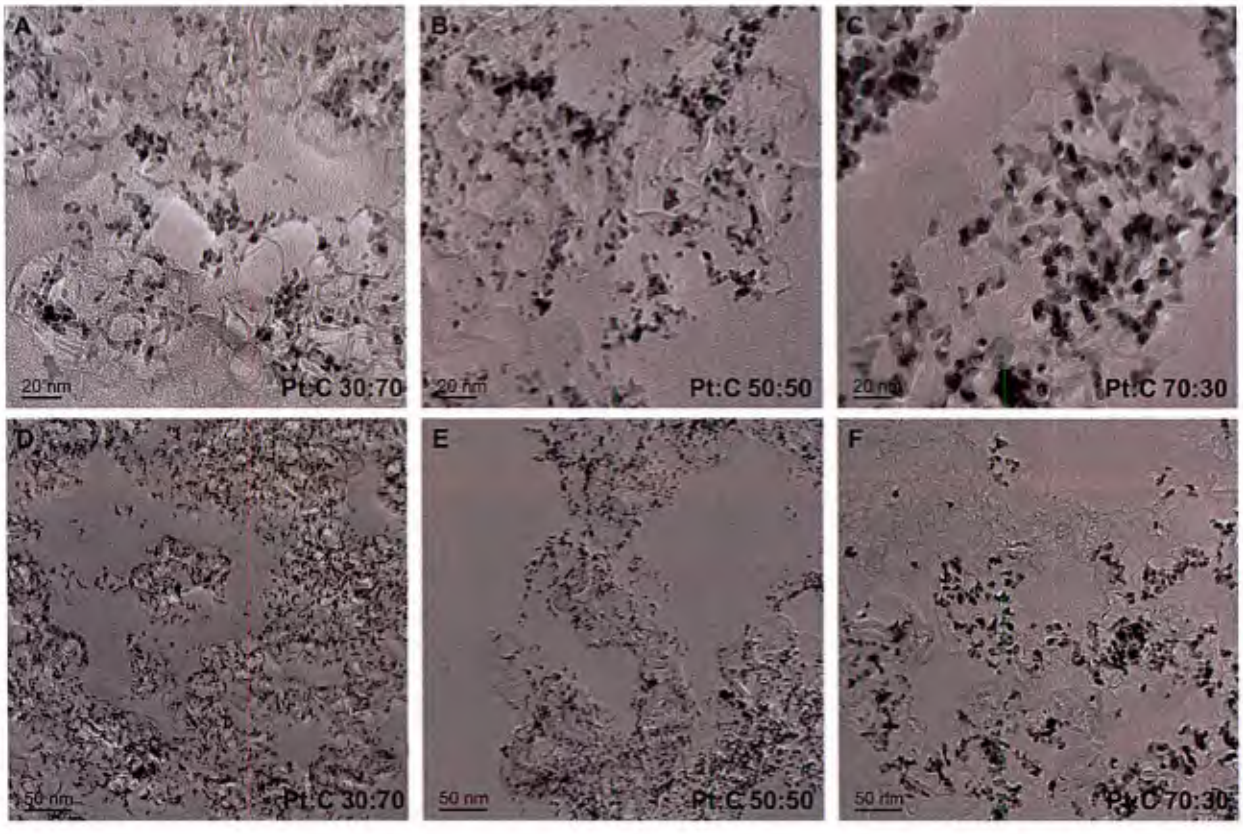

Figure 38. TEM images of epoxy-embedded fresh 30:70 (A, D), 50:50 (B, E) and 70:30 (C, F) Pt:C electrodes. The latter exhibits a higher proportion of Pt uncovered carbon area as a result of a higher degree of Pt particle agglomeration.

measurements ($d_{70:30\ Pt:C}$:10.9 nm>$d_{30:70\ Pt:C}$:5.8 nm>$d_{50:50\ Pt:C}$:4.9 nm). Such a difference in average Pt particle size represents a 40% loss of surface/volume ratio when comparing the 70:30 to the 50:50 Pt:C ratio samples. The Scherrer equation, however, provides a volume-weighted average size, while the TEM analysis performed provides an arithmetic mean size, which explains the higher values obtained through the former.

Several TEM images of the samples subjected to fuel cell standard operation conditions were used to characterize the changes in the Pt size distributions. Figure 40 shows representative TEM images of the 50:50 Pt:C sample before Figure 40 left) and after (Figure 40 right) FC operation. An evident increase of Pt size during FC operation can be observed in these images. Pt size distributions before (blue) and after (orange) FC operation for 30:70 Figure 37 A), 50:50 (Figure 37 B) and 70:30 (Figure 37 C) Pt:C cathodes are also shown, exhibiting a significant widening and a tendency towards higher Pt particle sizes. This behavior has been associated with the combination of two processes during FC operation: crystallite migration and coalescence, and Ostwald ripening.[41, 49] The former process promotes total surface energy minimization without involving particle dissolution, and is characterized by a Pt size distribution with peaks at small sizes, tailing toward larger sizes. The electrochemical Ostwald ripening effect involves the dissolution of smaller particles and its further redeposition on the larger particles surface, and it features an asymmetric particle size distribution with a tail toward a small particle end due to the smaller particles dissolution.[49]

Among all the samples, only the post-operation 50:50 Pt:C ratio sample produced skewness and kurtosis parameters within the range expected for a normal distribution. Given the non-normal distributions of the other samples, the KW test was also employed to compare the post-operation samples. A statistically significant difference was also established in this case at a 95% confidence level, and a similar trend to the one observed with the fresh samples was maintained.

Pore Size Distributions. The N_2 adsorption/desorption isotherms for the catalyst powder and the set of CLs are shown in Figure A. In general, all samples exhibit a similar hysteresis behavior. Hysteresis has been associated with the cavitation mechanism of condensed nitrogen in the

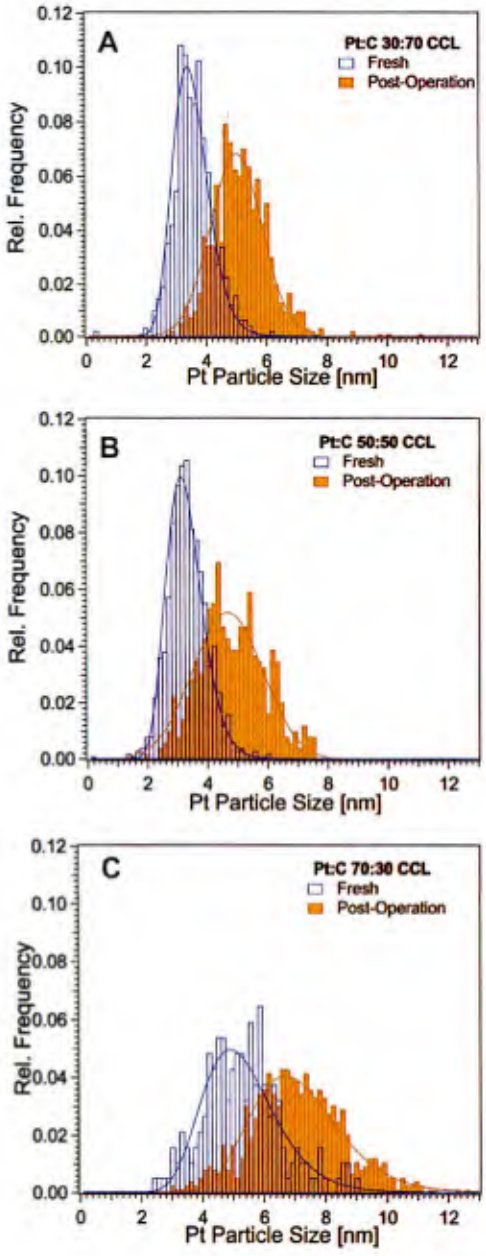

Figure 39. Pt particle size histograms for 30:70, 50:50 and 70:30 Pt:C ratio CLs before (blue) and after (orange) FC testing calculated from TEM micrograph processing.

pores, which shifts the desorption plot to lower relative pressures.[50] This suggests the presence of a porous structure on the carbon support that is maintained in the CL despite ionomer presence.

The pore size distributions shown in Figure 40B were calculated from the N_2 adsorption/desorption measurements using the BJH method.[51] The pore structure shows qualitatively similar features in all cases, exhibiting two characteristic peaks: wide in the

secondary pore region and sharp in the primary pore region. An evident pore volume decrease occurs for all CL samples when compared to the catalyst powder because of the ionomer

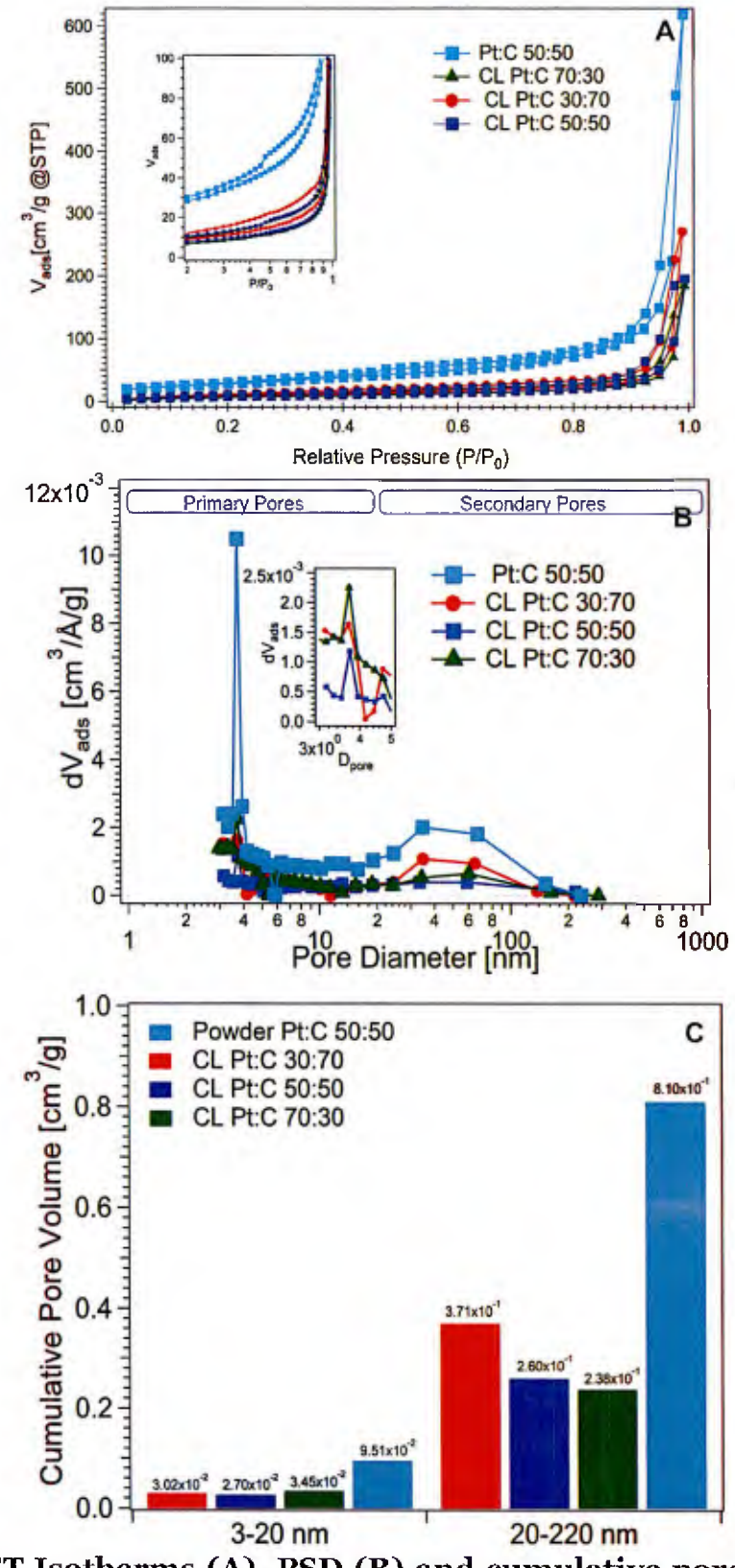

Figure 40. BET Isotherms (A), PSD (B) and cumulative pore volume (C) for the 50:50 catalyst powder, and the 30:70, 50:50 and 70:30 Pt:C ratio CLs showing a bimodal pore size distribution in all cases.

penetration into the pores, which has been assumed to occur mainly in the surface of carbon agglomerates (>20 nm diameter mesopores). [21, 34, 35]

Among the CL samples, the 70:30 Pt:C ratio presents a slightly higher primary pore (small pores) volume, and the 30:70 Pt:C ratio sample exhibits the highest secondary pore (large pores) volume as can be observed in Figure 40C, where the cumulative pore volume over the 3-20 nm and 20-220 nm ranges are presented for both the 50:50 Pt:C powder and the CL samples. Given that both the carbon support and the I:C ratio are fixed for the CL samples in this study, we can affirm that the Pt:C ratio has a significant influence on the ionomer distribution throughout the CL and, therefore, on the resultant CL pore network structure. A theoretical model developed by Ishikawa et al. showed that ionomer coverage on Pt surface decreases with an increase in the Pt:C ratio. [52] This behavior can be potentially caused by a higher affinity of the ionomer towards the carbon surface, which has been suggested by previous PFSA ionomer adsorption studies carried. [53, 54] This effect, along with the significant Pt particle agglomeration observed in the 70:30 Pt:C CL sample through TEM characterization (Figure 38) can lead to higher ionomer agglomeration on the >20 nm mesopores, thus reducing the available pore volume in this size range.

In Figure 41, schematics of the Pt:C ratio effect on the Pt and ionomer distributions on a graphitic carbon support are shown summarizing the information obtained from the TEM and BET studies. On this type of carbon, Pt particles typically exhibit a tendency to accumulate in the structure defects and edges, and the degree of particle agglomeration and sizes varies with the Pt:C ratio.

Several studies have shown that the ionomer distribution throughout the CL strongly depends on the overall ionomer content. [8,10, 35] Pt:C ratio also plays a significant role in defining the ionomer distribution. As illustrated in Figure 41 the results suggest that a lower Pt:C ratio promotes a more uniform distribution of the ionomer throughout the CL structure, providing a higher coverage and enabling the exposure of a higher inter-agglomerate pore volume (Figure 40C). Higher Pt:C ratio, on the other hand, can promote ionomer accumulation on the the >20 nm mesopores as suggested by BET results.

Water Uptake

The water sorption isotherms obtained with the CL samples, along with previous results for 3M 825 EW membrane, are shown in Figure 42A [55] The CL water uptake isotherms are similar in shape to that corresponding to the 3M bulk membrane and previous results from Nafion reports. [56, 57] The 3M bulk membrane exhibits higher uptake over the entire water vapor activity range, when compared to the 30:70 and 50:50 Pt:C CL samples; these results are in agreement with previously reported data on CL water uptake.[25,57] Swelling (□=6) behavior is only observed in the CLs at high RH (>0.95), and this swelling attenuation in the CL samples agrees with previous observations in recast ionomer films. [15, 35, 58, 59] A decrease in water uptake in these thin ionomer films has been associated with an increase in the Young's modulus caused by polymer confinement or, as also likely, the effect of interaction of the ionomer with the support.[60]

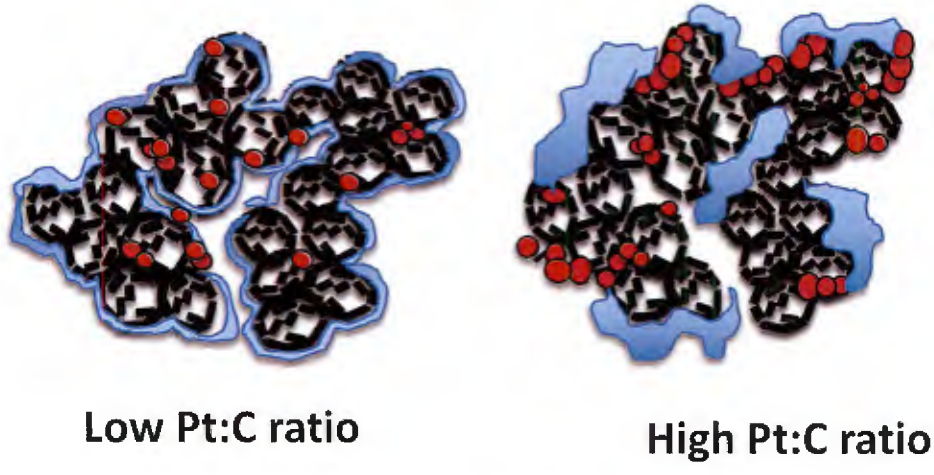

Figure 41. Schematic illustrating Pt and ionomer distribution as a function of Pt:C ratio at a fixed I:C ratio illustrating Pt particle (red), carbon agglomerates (black) and ionomer (blue) distribution.

On the other hand, the 70:30 Pt:C ratio sample exhibits higher water uptake values than the 30:70 and 50:50 Pt:C ratio CL materials over the entire water vapor activity range, and it also exhibits larger swelling at a lower RH. Previous studies have shown a strong influence of the presence of Pt on the water uptake by the CL. [57. 61] A higher Pt:C ratio involves the presence of larger Pt particle sizes and degree of agglomeration Figure 38 which can accentuate this effect. The higher uptake observed in the highest Pt:C ratio can be explained by two factors: (i) a higher primary pore (2-20 nm) volume (Figure 41B), where capillary condensation of water can take place, [34, 35, 62] and (ii) larger ionomer agglomeration suggested by the BET characterization Figure 41 which can enable more bulk-like ionomer behavior. Overall, we note that the water uptake data suggest that higher Pt loading is associated with weaker interactions, leading to a suggestion that the ionomer-carbon interaction is a significant factor.

Catalyst Layer Proton Conductivity

The σ_{CL,H^+} measurements are shown in Figure 42B, along with the bulk 825EW 3M ionomer results calculated elsewhere. [56] The CL samples and the bulk membrane exhibit a similar trend with RH: the proton conductivity increases with hydration, as reported in the literature for Nafion membranes. [63] Overall, this reflects, with increasing hydration, the gradual loosening of the proton interaction with sulfonate groups in which the environment of the proton hydrate 'complex' evolves from contact ion pairs to solvent-separated ion pairs and then to fully dissociated protons moving in a water-like medium. This has long been analyzed in studies of membranes. The change in average environment in the ionomer is associated with a variation in the proton transport mechanisms with the humidity level. In membranes equilibrated at lower RH, in the absence of a fully developed hydrogen-bond network in a 'watery' environment, the vehicular mechanism prevails. [64-66] When the RH increases, bulk water phase formation throughout the ionomer promotes proton transport through structural diffusion (Grotthuss hopping). In contrast to the vehicular mechanism, structural diffusion is not limited by the translational movement, which results in faster proton conduction. [15, 16, 67] As always for macroscopic measurements, all environments and mechanisms may be locally present and it is the difference in contribution of a given aspect to a population-weighted average that is actually observed.

However, the ionomer in the CL might be expected to be of a different character. Sun and Zawodzinski, in a study of water diffusion within a CL as a function of RH/water content,

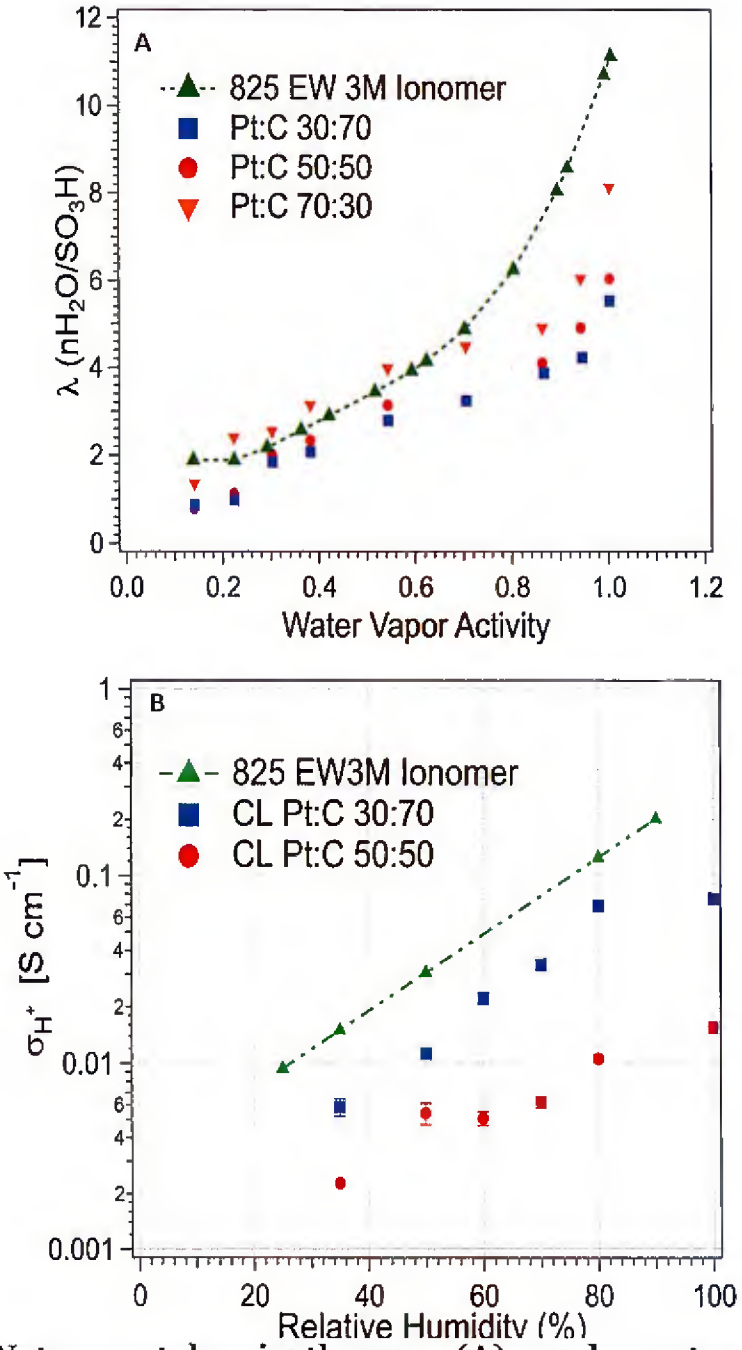

Figure 42. Water uptake isotherms (A) and proton conductivities measurements (B) for the set of CLs (30:70, 50:50 and 70:30 Pt:C ratios). The behavior for bulk 825 EW 3M ionomer obtained in previous studies have been included for comparison purposes. [55]

showed that local measures of mobility (NMR relaxation times) are similar to those in the bulk membrane for similar (low) λ values. (For low λ values we can safely assume that the water interacts with the sulfonic acid sites and does not condense in pores.) However, longer-range

mobility (as reflected in PGSE diffusion coefficients) differed dramatically. The continuity of the film, required for mass transport in the low λ regime, was suggested to be incomplete under such conditions. Similar effects would influence the proton conductivity of the CL.

Indeed, the CL samples exhibit a lower proton conductivity when compared to the bulk 3M membrane.[16, 63, 68, 69] This trend is ascribed to confinement and substrate interaction effects. [70] In the CL ionomer, the nature of the ionomer-Pt and ionomer-carbon interactions determine the resultant ionomer nanostructure (i.e. ordering, thickness etc.), affecting the water content and thereby transport properties of ions and water within it.

Among the CL samples, the lowest Pt:C (30:70) ratio exhibits higher σ_{CL,H^+} values Figure…B). This result is consistent with the physicochemical characterization result: the higher secondary pore volume obtained with the 30:70 Pt:C ratio sample suggests lower ionomer accumulation in the pores and a more homogeneous ionomer distribution throughout the CL. This result contrasts with the water uptake measurements, which showed an inverse trend with the Pt:C ratio. This result emphasizes the importance of the ionomer network connectivity throughout the CL to increase the ionic conductivity.

Thus, the increased ionic conductivity observed in CL samples with low Pt:C ratios can be related to the more continuous ionomer network that also promotes the structural diffusion mechanism. This is consistent with previous findings of Sun and Zawodzinski. [30]

To summarize this discussion, a significant influence of Pt particles and their size on the CL structure and properties was observed. In general, all CLs showed a significant deviation from the bulk-like ionomer behavior. Lower Pt content resulted in a lower Pt particle size, higher inter-particle distance, and a larger secondary pore (>20 nm) volume. The later has been associated with a more homogeneous ionomer distribution, given that the I:C ratio was fixed for all CLs in this study. The lowest Pt:C ratio, consequently, provided higher proton conductivity. Higher Pt content, on the other hand, presented a significantly higher Pt particle size and degree of agglomeration. In terms of pore networks, the 70:30 Pt:C ratio CL displayed a reduction in the secondary pore volume, but a slightly higher primary pore volume. These observations indicate a direct relationship between the Pt:C ratio, and the distribution of the individual components in the CL. This combination of data highlights the importance of microstructure on transport in the fuel cell CL.

References for Section II.3

1. J. Zhang, Ed., *PEM Fuel Cell Electrocatalysts and Catalyst Layers Fundamentals and Applications*, p. 1-1137, Springer London, (2008).
2. U.S. Department of Energy, *Multi-Year Research, Development, and Demonstration Plan: Fuel Cells*, (2016).
3. E. B. Yeager and A. J. Appleby, *Energy*, 11, 137–152 (1986).
4. M. S. Wilson and S. Gottesfeld, *J. Appl. Electrochem.*, 22, 1–7 (1992).
5. M. S. Wilson and S. Gottesfeld, *J. Electrochem. Soc.*, 139, L28–L30 (1992).
6. X. Cheng, B. Yi, M. Han, J. Zhang, Y. Qiao, and J. Yu, *J. Power Sources*, 79, 75–81 (1999).
7. C. Y. Ahn, J. Y. Cheon, S. H. Joo, and J. Kim, *J. Power Sources*, 222, 477–482 (2013).
8. X. Zhao, W. Li, Y. Fu, and A. Manthiram, *Int. J. Hydrogen Energy*, 37, 9845–9852 (2012).
9. E. Antolini, L. Giorgi, A. Pozio, and E. Passalacqua, *J. Power Sources*, 77, 136–142 (1999).
10. E. Passalacqua, F. Lufrano, G. Squadrito, A. Patti, and L. Giorgi, *Electrochim. Acta*, 46, 799–805 (2001).
11. J. Xie, F. Xu, D. L. Wood, K. L. More, T. A. Zawodzinski, and W. H. Smith, *Electrochim. Acta*, 55, 7404–7412 (2010).
12. Y. Liu, C. Ji, W. Gu, J. Jorne, and H. a. Gasteiger, *J. Electrochem. Soc.*, 158, B614 (2011).
13. K. A. Mauritz and R. B. Moore, *Chem. Rev.*, 104, 4535–4586 (2004).
14. S. Holdcroft, *Chem. Mater.*, 26, 381–393 (2014).
15. D. K. Paul, A. Fraser, and K. Karan, *Electrochem. commun.*, 13, 774–777 (2011).
16. Z. Siroma, R. Kakitsubo, N. Fujiwara, T. Ioroi, S. Yamazaki, and K. Yasuda, *J. Power Sources*, 189, 994–998 (2009).
17. R. Subbaraman, D. Strmcnik, V. R. Stamenkovic, and N. M. Markovic, *J. Phys. Chem. C*, 114, 8414–8422 (2010).
18. K. Kodama, R. Jinnouchi, T. Suzuki, H. Murata, T. Hatanaka, and Y. Morimoto, *Electrochem. commun.*, 36, 26–28 (2013).
19. A. P. Saab, F. H. Garzon, and T. A. Zawodzinski, *J. Electrochem. Soc.*, 149, A1541 (2002).
20. Y. Liu, M. W. Murphy, D. R. Baker, W. Gu, C. Ji, J. Jorne, and H. a. Gasteiger, *J. Electrochem. Soc.*, 156, B970 (2009).
21. M. Eikerling and A. . Kornyshev, *J. Electroanal. Chem.*, 475, 107–123 (1999).
22. M. C. Lefebvre, R. B. Martin, and P. G. Pickup, *Electrochem. Solid-State Lett.*, 2, 259–261 (1999).
23. H. Angerstein-Kozlowska, B. E. Conway, and W. B. A. Sharp, *J. Electroanal. Chem.*, 43, 9–36 (1973).
24. T. A. Zawodzinski, *J. Electrochem. Soc.*, 140, 1981 (1993).
25. H. Iden, K. Sato, A. Ohma, and K. Shinohara, *J. Electrochem. Soc.*, 158, B987 (2011).
26. J. Liu and M. Eikerling, *Electrochim. Acta*, 53, 4435–4446 (2008).
27. C.-N. Sun and T. A. Zawodzinski, *ECS Electrochem. Lett.*, 11, 36–39 (2012).
28. A. Kongkanand, *J. Phys. Chem. C*, 115, 11318–11325 (2011).
29. D. R. P. Morris, S. P. Liu, D. Villegas Gonzalez, and J. T. Gostick, *ACS Appl. Mater. Interfaces*, 6, 18609–18618 (2014).
30. C.-N. Sun, K. L. More, G. M. Veith, and T. A. Zawodzinski, *J. Electrochem. Soc.*, 160, F1000–F1005 (2013).
31. S. A. Eastman, S. Kim, K. A. Page, B. W. Rowe, S. Kang, C. L. Soles, and K. G. Yager, *Macromolecules*, 45, 7920–7930 (2012).
32. N. Zamel, *J. Power Sources*, 309, 141–159 (2016).

33. T. Shimura, K. Miyatake, and M. Watanabe, *Eur. Polym. J.*, 44, 4054–4062 (2008).
34. T. Soboleva, X. Zhao, K. Malek, Z. Xie, T. Navessin, and S. Holdcroft, *ACS Appl. Mater. Interfaces*, 2, 375–384 (2010).
35. T. Soboleva, K. Malek, Z. Xie, T. Navessin, and S. Holdcroft, *ACS Appl. Mater. Interfaces*, 3, 1827–1837 (2011).
36. M. Wissler, *J. Power Sources*, 156, 142–150 (2006).
37. L. Castanheira, L. Dubau, M. Mermoux, G. Berthome, N. Caque, E. Rossinot, M. Chatenet, and F. Maillard, *ACS Catal.*, 4, 2258–2267 (2014).
38. L. Castanheira, W. O. Silva, F. H. Lima, A. Crisci, L. Dubau, and F. Maillard, *ACS Catal.*, 5, 2184–2194 (2015).
39. A. Pebler, *J. Electrochem. Soc.*, 133, 9 (1986).
40. J. Aragane, *J. Electrochem. Soc.*, 135, 844 (1988).
41. K. L. More, R. Borup, and K. S. Reeves, *ECS Trans.*, 1, 717–733 (2006).
42. D. A. Blom, J. R. Dunlap, T. A. Nolan, and L. F. Allard, *J. Electrochem. Soc.*, 150, A414 (2003).
43. D. C. Montgomery, *Applied Statistics and Probability for Engineers Third Edition*, p. 455, (2003).
44. B. G. Tabachnick and L. Fidell, *Using multivariate statistics* L. S. Fidell, Editor, 5th Ed., Allyn & Bacon/Pearson Education, Boston, MA, (2007).
45. W. Trochim and J. P. Donnelly, *Research Methods Knowledge Base*, p. 361, (2006).
46. A. L. Patterson, *Phys. Rev.*, 56, 978–982 (1939).
47. X. Z. Yuan, C. Song, H. Wang, and Z. J., *Electrochemical Impedance Spectroscopy in PEM Fuel Cells: Fundamentals and Applications*, p. 1689-1699, Springer, (2010).
48. E. Theodorsson-Norheim, *Comput. Methods Programs Biomed.*, 23, 57–62 (1986).
49. K. Sasaki, M. Shao, and R. R. Adzic, in *Polymer Electrolyte Fuel Cell Durability*, F. N. Büchi, M. Inaba, and T. J. Schmidt, Editors, p. 7–27, Springer New York, New York, NY (2009).
50. Y.-C. Park, H. Tokiwa, K. Kakinuma, M. Watanabe, and M. Uchida, *J. Power Sources*, 315, 179–191 (2016).
51. E. P. Barrett, L. G. L. G. Joyner, and P. P. Halenda, *J. Am. Chem. Soc.*, 73, 373–380 (1951).
52. H. Ishikawa, Y. Sugawara, G. Inoue, and M. Kawase, *J. Power Sources*, 374, 196–204 (2018).
53. S. Ma, Q. Chen, F. H. Jogensen, P. C. Stein, and E. Skou, *Solid State Ionics*, 178, 1568–1575 (2007).
54. S. M. Andersen, *Appl. Catal. B Environ.*, 181, 146–155 (2016).
55. M. Maalouf, B. Pyle, C.-N. Sun, D. Wu, S. J. Paddison, M. Schaberg, M. Emery, K. H. Lochhaas, S. J. Hamrock, H. Ghassemi, and T. A. Zawodzinski, in *ECS Transactions*,, p. 1473–1481 (2009).
56. T. A. Zawodzinski, C. R. Derouin, S. Radzinski, R. J. Sherman, V. T. Smith, T. E. Springer, and S. Gottesfeld, *J. Electrochem. Soc.*, 140, 1041–1047 (1993).
57. A. Kusoglu, A. Kwong, K. T. Clark, H. P. Gunterman, and A. Z. Weber, *J. Electrochem. Soc.*, 159, 530–535 (2012).
58. M. A. Modestino, A. Kusoglu, A. Hexemer, A. Z. Weber, and R. A. Segalman, *Macromolecules*, 45, 4681–4688 (2012).
59. S. K. Dishari and M. A. Hickner, *ACS Macro Lett.*, 1, 291–295 (2012).

60. K. A. Page, A. Kusoglu, C. M. Stafford, S. Kim, R. J. Kline, and A. Z. Weber, *Nano Lett.*, 14, 2299–2304 (2014).
61. A. Kusoglu, D. Kushner, D. K. Paul, K. Karan, M. A. Hickner, and A. Z. Weber, *Adv. Funct. Mater.*, 24, 4763–4774 (2014).
62. M. Eikerling, *J. Electrochem. Soc.*, 153, E58 (2006).
63. A. Kusoglu and A. Z. Weber, *Chem. Rev.*, 117, 987–1104 (2017).
64. K. D. Kreuer, *J. Memb. Sci.*, 185, 29–39 (2001).
65. K. D. Kreuer, *Solid State Ionics*, 97, 1–15 (1997).
66. K. D. Kreuer, S. J. Paddison, E. Spohr, and M. Schuster, *Chem. Rev.*, 104, 4637–4678 (2004).
67. H. K. Shim, D. K. Paul, and K. Karan, *Macromolecules*, 48, 8394–8397 (2015).
68. M. A. Modestino, D. K. Paul, S. K. Dishari, S. A. Petrina, F. I. Allen, M. A. Hickner, K. Karan, R. A. Segalman, and A. Z. Weber, *Macromolecules*, 46, 867–873 (2013).
69. A. Kusoglu, T. J. Dursch, and A. Z. Weber, *Adv. Funct. Mater.*, 26, 4961–4975 (2016).
70. L. Cindrella, A. M. Kannan, J. F. Lin, K. Saminathan, Y. Ho, C. W. Lin, and J. Wertz, *J. Power Sources*, 194, 146–160 (2009).
71. K. Ikeda, N. Nonoyama, and Y. Ikogi, *216th ECS Meet.*, 9 (2009).
72. A. P. Young, J. Stumper, and E. Gyenge, *J. Electrochem. Soc.*, 156, B913 (2009).
73. A. Lasia, in *Modern Aspects of Electrochemistry*, B. E. Conway, J. O. Bockris, and R. E. White, Editors, vol. 32, p. 143–242, Kluwer Academic Publishers (2002).
74. E. A. Ticianelli, C. R. Derouin, and S. Srinivasan, *J. Electroanal. Chem. Interfacial Electrochem.*, 251, 275–295 (1988).
75. K. R. Cooper, *Fuel Cell Mag.*, 1–3 (2009).
76. T. Biegler, D. A. J. Rand, and R. Woods, *J. Electroanal. Chem. Interfacial Electrochem.*, 29, 269–277 (1971).

II.4 Multiscale Modeling of Catalyst Layers-Method Development

A one dimensional macrohomogeneous model of a Solid Acid Fuel Cell (SAFC) was developed to identify the dominant parameters affecting cell performance. The model parameters were estimated through a computational sensitivity analysis in which one model parameter was varied to assess the range of values of that parameter yielding convergence and qualitatively reasonable fits. Using this analysis to provide initial values, the model was used to simultaneous fit a set of polarization curves with physical input data (derived from measurements) and model parameters. The Tafel slopes obtained in the model agree with those calculated assuming a single-electron transfer rate-limiting step and a transfer coefficient of 0.5 at 250°C. The Open Circuit Voltage (OCV) drop agrees closely with the theoretical value at 250°C. Based on the sensitivity analysis, permeability and roughness factor are key parameters for higher performance. Calculated current density distribution and a breakdown of contributing overpotentials are calculated using the model parameters and presented. The results show the importance of limitations in available surface area and mass transport to the catalytic surface as the limiting processes in SAFC performance. This points to decreasing catalyst layer thickness and improved microstructural configuration as targets for SAFC performance improvement. More generally, this work showed a modeling approach for obtaining clear and statistically defensible parameter estimation using simple physics and a rigorous routine that demands upfront sensitivity analysis of parameter effects to minimize the ultimate number of modeling parameters. Simultaneous fits to multiple data sets obtained by varying a single experimental control parameter are then carried out using the minimal set of variable parameters.

Solid Acid Fuel Cells (SAFCs) employ proton conductors that become highly conductive above a certain temperature, referred to as the 'superprotonic' transition[1]. The most practical and developed of these is the CsH_2PO_4 (CDP) electrolyte, which undergoes this transition at 228°C. CDP-based SAFCs typically operate at 250°C. Operation at this temperature imparts tolerance to fuel stream impurities such as CO[2-4], which could enable SAFC systems to operate on minimally processed fuels such as natural gas or methanol. The solid nature of the electrolyte additionally renders the membrane particularly resistant to reactant crossover.

The unique characteristics of the CDP electrolyte pose several challenges to SAFC optimization, particularly in the area of cathode microstructure. The lack of oxygen solubility in CDP demands that an active site be located at the intersection of the electrolyte, catalyst, and pore.

To address this requirement, an approach in which electrolyte particles are coated evenly in catalyst material to maximize available electrochemical surface area was developed. In this catalyst layer construct, high Pt loading in needed since the Pt catalyst also acts as the electronic conductor and thus must form a contiguous path throughout the electrode. Though this configuration is an improvement over earlier approaches, the mass-normalized activity of Pt in SAFC cathodes remains unsatisfactory and high Pt loadings are needed.

In this contribution, we describe a model of the performance of an SAFC cathode. In SAFCs, several features of the electrode lend themselves to relatively simple modeling approaches. Most important among the simplifying features is the absence of liquid water, which significantly complicates the modeling of PEM fuel cells. A successful model must take into account the thermodynamics and kinetics of the electrode reactions, ohmic losses related to the resistance of the electronic and ionic species traveling through the catalyst layer and mass transfer limitations directly related to the reactants access to the electrocatalytic site [5-7]. Many modeling approaches are possible but given its relative simplicity and direct connection to physically meaningful parameters, that of Springer et al. [8] is used here as a framework. That model is isothermal and considers polarization and electrode effects only through a simple 0-D polarization equation in a 1-D model. Within the cathode, they examined utilization of the catalyst and the effects of performance on various parameters such as the diffusion-medium porosity and the inlet-gas composition. The cathode is treated as a uniformly distributed layer, and the model does not treat flooding [5, 8, 9]. These features are adequate representations of the SAFC case, in which liquid water is absent.

One feature of our study that is infrequently found in the modeling body of work is its close coupling to physical parameters, especially derived from measurements, available as input. Also, our emphasis is on the simultaneous description of multiple data sets tailored to provide maximum information. If we are to use models as a path to understanding, it is important to minimize the number of variables used in fitting and to use data sets that are sufficiently detailed to allow meaningful probes of the fit. An example of this is our treatment of the 'kinetic' region of the polarization curves. Typical polarization curves collect data points with spacing of ~20 to 50 mV. This provides only a few points in the kinetic region with the result that this aspect is rarely fit satisfactorily. Here we intentionally create data sets with many more points taken in that region, putting more emphasis on achieving a fit to the observed kinetics and thereby giving a higher level

of confidence in the result.

Our goal in modeling SAFC catalyst layers is to identify the main macroscopic parameters that affect the performance. By implementing extensive sensitivity tests of model parameters and selecting appropriate experimental data sets, a macroscopic modeling study can serve to reveal the physical basis of the important performance differences resulting from the use of given catalyst layer structures, on one hand, and different kinetics on the other.

Finally, we provide a few comments on the expectations regarding physical properties of the catalyst layer that shape our analysis and that are rather different from those encountered in analogous PEM fuel cells. First, the cell operates at high temperature, suggesting differences in kinetic and thermodynamic parameters but also in mass transport parameters. However, the catalyst layers used are quite thick. The CDP electrolyte is essentially impermeable to gases. Based on the latter two features, offset by higher intrinsic mass transport rates in the gas phase from the higher temperature, we are uncertain of the overall resulting effective transport rates but can reasonably expect them to be somewhat slow.

Model description

As noted above, we chose to represent the SAFC cathode with 1-D model that treats the fuel cell in varying degrees of complexity; modeling the different components of the fuel cell going from simple equations to complex expressions derived from physical models.

Springer-type model

The model is a 1D macrohomogeneous model operating at steady state. Any effects of the internal generation of liquid water, ionic conductivity variations within the catalyst layer, or local variations of the rate of the interfacial ORR process are not considered. In addition, the gas mixture was considered to be ideal, and delivered via single-phase flow with steady state and isothermal operation at T=523K. As noted above, it is a very good assumption to neglect liquid water and the lack of spatial variation of properties is implied in the term macrohomogeneous.

Model Equations

The cathode catalyst layer model highlights the effects of limited fluxes of oxygen in this layer coupled to the electrochemical reaction. Equations 1 through 4 are the basic equations given by Springer et al, which take into account variations of parameters along the x coordinate of the

catalyst layer, the direction normal to the planes of the flow channel and membrane. In the x-coordinate where $x = x_1$ specifies the catalyst layer/flow channel interface, and $x = x_{\delta CL}$ specifies the catalyst layer/membrane interface.

$$\frac{\partial \eta}{\partial x} = \frac{I\delta_{CL}}{\sigma} = IR_{CL} \qquad \textbf{Equation 6}$$

$$\frac{\partial I}{\partial x} = p_{O_2}\frac{C}{C^*}A_r i_0 exp\left[\left(\frac{\eta}{b}\right)\right] \qquad \textbf{Equation 7}$$

$$\frac{\partial \frac{C}{C^*}}{\partial x} = \frac{I - I_l}{p_{O_2} I_D} \qquad \textbf{Equation 8}$$

$$I_D = \frac{nFDC^*}{\delta_{CL}} \qquad \textbf{Equation 9}$$

Boundary conditions:

$$x = x_1 \qquad \frac{C}{C^*} = 1, \eta = E_{eq} - OCV \qquad \textbf{Equation 10}$$

$$x = x_3 = x_{\delta_{CL}} \qquad \frac{\partial \frac{C}{C^*}}{\partial x} = 0, \frac{\partial I}{\partial x} = 0 \qquad \textbf{Equation 11}$$

In these equations, R_{CL} represents the resistance through the cross-sectional area of the catalyst layer; I_D is a characteristic limiting diffusion current density. The experimentally controlled variables considered are the overpotential (η), the current density (I) and the oxygen partial pressure (p_{O2}). Equation 1 is an ohmic relationship between local current density and the local variation of η, determined by the protonic resistivity of the catalyst layer. Equation 2 describes the local rate of current generation within the catalyst layer in terms of the oxygen partial pressure at the catalyst layer/flow channel interface, the local concentration of oxygen relative to its concentration at the catalyst layer/gas interface, and the local overpotential. In this equation b represents the Tafel slope. Equation 3 describes the gradual transformation of the oxygen flux to a protonic current along x, such that the sum of the two fluxes is kept constant and equal to the oxygen flux at the catalyst layer/flow channel interface.

The remaining parameters, which define the behavior of the cell for each set of operating conditions, include the cathode inlet gas stream composition, flow rate, catalyst layer thickness

and back pressure on the cell.

Key model parameters

The model considers losses caused by the rate of the oxygen reduction reaction (ORR) process at the catalyst/proton-conductor interface, limited oxygen permeability and limited ionic conductivity within the catalyst layer. By using an extensive set of experimental data obtained for several values of oxygen partial pressure and different catalyst layer thicknesses, we were able to reduce the degrees of freedom for our fittings. The key model parameters that describe the losses in the PEMFC are as follow:

- i_o: exchange current density. In the original paper, this parameter was the current density calculated at 0.9V. For our approach, we decided to use the exchange current density, calculated from the Tafel plot, log i vs η as follows:

  Tafel equation:

  $$i = i = i_0 e^{-\alpha f \eta} \qquad \textbf{Equation 12}$$

  From here:

  $$\eta = \frac{2.3RT}{\alpha F} log i_0 - \frac{2.3RT}{\alpha F} log i \qquad \textbf{Equation 13}$$

  Where the Tafel slope is defined as:

  $$b = -\frac{2.3RT}{\alpha F} \qquad \textbf{Equation 14}$$

- A_r, the ratio of actual catalyst surface area per unit geometric surface area, essentially a 'roughness factor.' (We note that these first two terms are not introduced as separated parameters in the fits to follow.)
- DC*, the product of the effective diffusion coefficient of oxygen (cm^2/s) treated as the permeability of oxygen within the catalyst layer. To calculate the effective diffusion coefficient we used the equation for gas phase system in porous media as an Arrhenius type formula (well-known and widely used in literature)[10]:

  $$D_i = D_0 * \exp(-E/RT) \qquad \textbf{Equation 15}$$

As these values are not tabulated for CDP, our approach is to find the initial value for O_2, and air, then use the Bruggeman relation to calculate the effective diffusion coefficient[11]:

$$D_i^{eff} = \varepsilon^{1.5} D_i \qquad \textbf{Equation 16}$$

- C*, O_2 concentration C (0) at catalyst layer inlet per atm.
- Ari_0: Roughness-corrected current density (RCCD)

Model validation

For each set of experimental and fitted data, we performed two nonparametric statistical tests: Mann-Whitney U[12] and Kolmogorov-Smirnov[13]. For Mann-Whitney U test the null hypothesis is that two populations are the same for all data points. For a Two-sample Kolmogorov-Smirnov test the null hypothesis that the one-dimensional probability distributions of the data points do not differ one from the other. In both cases, the observations must be independent and the data nominal or ordinal. The null hypothesis is rejected if the p-value is smaller than the significance (See appendix – Statistical tests). Table I condenses the statistical test results for both fuel cell models showing that the modeled data represents the experimental with a 97% of confidence.

Table I. Statistical goodness of fit tests for SAFC system

% O2	Test	p-value	Statistic	Decision
O2_7mg	Mann-Whitney	0.957	-0.054	**Retain H_0**
	KS	1.000	0.031	**Retain H_0**
Air_7mg	Mann-Whitney	1.000	0.000	**Retain H_0**
	KS	1.000	0.032	**Retain H_0**
O2_3.5mg	Mann-Whitney	0.999	-0.001	**Retain H_0**
	KS	1.000	0.062	**Retain H_0**
Air_3.5mg	Mann-Whitney	1.000	0.000	**Retain H_0**
	KS	1.000	0.032	**Retain H_0**
O2_1.75mg	Mann-Whitney	1.000	0.000	**Retain H_0**

	KS	1.000	0.064	**Retain H_0**
Air_1.75mg	Mann-Whitney	1.000	0.000	**Retain H_0**
	KS	1.000	0.031	**Retain H_0**

Experimental

Cell Fabrication

Solid acid fuel cells were fabricated using an anode-supported configuration similar to those described previously [3]. Using a bilayer sintered stainless steel (grade 304) mesh disc (2.85 cm^2) as an anode current collector and structural support, anode, membrane, and cathode layers were sequentially formed by uniaxal compression of powdered composites in a stainless steel die.

Anodes were formed at 90 MPa from a mechanical mixture of CDP, 60wt%Pt supported on carbon black (Vulcan XC-72R, Cabot Corp.) and naphthalene (a fugitive binder) in a 3:1:1 ratio, respectively, by weight. The CDP membrane was applied to the anode at 125 MPa and was approximately 50 μm in thickness.

Cathode electrocatalyst powders were synthesized via a method described previously in the literature[14, 15]. CDP particles with a specific surface area of approximately 2 m^2/g were mechanically combined in a glass vial with an appropriate quantity of Pt(II)pentanedionate (Acros Organics). The coarse mixture was heat-treated at 210 C in a deoxygenated N_2-water vapor atmosphere, resulting in the vapor deposition of a conformal layer of Pt nanoparticles decorating all exposed surfaces of the CDP particles. The Pt precursor content was adjusted to arrive at 20wt% Pt^0 on CDP, which was validated gravimetrically.

From this common feedstock of cathode electrocatalyst powder, SAFCs of various cathode thickness (and thus Pt loading) were fabricated by laminating the powders to directly to the CDP membrane via uniaxial compression at 23 MPa. SAFCs were formed using 25 mg, 50 mg, and 100 mg of the 20wt% Pt@CDP catalyst powder, respectively yielding cathode Pt loadings of 1.75 mg_{Pt}/cm^2, 3.5 mg_{Pt}/cm^2, and 7.0 mg_{Pt}/cm^2. Cathode current collectors were comprised of a coarse single-layer stainless steel (grade 316) mesh and a carbon paper interlayer (SGL 34AA).

Microstructural Analysis

Freestanding SAFC cathodes were fabricated in a manner similar to the route detailed above, but densification of the dry cathode powders proceeded between two Kapton discs rather than atop the CDP membrane. The cathodes were easily separated from the Kapton for SEM and FIB-SEM analysis. The freestanding cathode samples were embedded in epoxy for FIB-SEM analysis in a Zeiss Auriga Dual Beam FIB/SEM. Image stacks were segmented using the Trainable Weka Segmentation plugin for Fiji/ImageJ and further analyzed using Fiji to derive electrode physical parameters. The full details of this work are the subject of a future contribution. Figure 43 shows the SEM images used to calculate the cathode thicknesses.

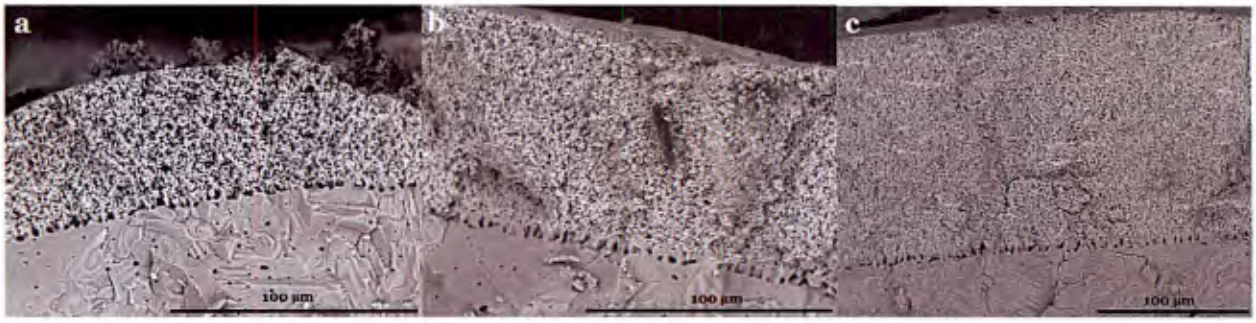

Figure 43 SEM images of the SAFC showing the cathode thickness. a) **1.75 mg/cm^2** b) **3.5 mg/cm^2** c) **7 mg/cm^2**

Electrochemical Testing

Fuel cell testing was conducted using stainless steel test rigs at a temperature of 250 °C with gases hydrated to a dew point of 75 °C (approximately 0.36 bar water partial pressure). Anodes were supplied ultrahigh-purity H_2 and cathodes were supplied either compressed air from a centralized compressor, or ultrahigh-purity O_2. Polarization curves were recorded with a Bio-Logic VSP potentiostat by scanning the working electrode potential at 10 mV s−1 from the open circuit potential to a cell potential of 0 V. Before and after the recording of the polarization curves, potentiostatic electrochemical impedance spectroscopy (EIS) was performed in a frequency range from 200 kHz to 200 mHz at 0.8 V cell voltage with a single sine perturbation amplitude of 10 mV. The high-frequency intercept of the EIS spectrum was used to eliminate the ohmic resistance of the cell from the polarization curves, yielding what we refer to as iR-free polarization curves. This protocol was repeated cyclically on an hourly basis, during which the cell was held at 0.6 V. Each cell was operated in an air atmosphere for several hours, and subsequently held at 0.6 V while

100% O2 was introduced to the cathode. The cyclic protocol was resumed after the current density in the new cathode atmosphere reached steady state.

After completion of testing, the cells were sectioned via fracture and samples were mounted for cross-sectional examination in a Hitachi TM-3000 SEM operating at 15 kV for determination of electrode thickness.

Results and Discussion

The experimental data to be fit consists of several polarization curves obtained for SAFCs. When compared to typical PEM cells modeled by Springer, the catalyst loading is quite high and catalyst layers are relatively thick.

The model requires multiple inputs. Table II presents the physical property values for the different MEAs and tests along with some determined in independent experiments. The mean porosity was determined to be 50% by analysis of FIB-SEM slices of a representative cathode sample. As expected, catalyst layer thickness (determined by SEM) increases roughly proportionally with Pt loading. The deviation from linearity may be attributed to the catalyst distribution on the carbon support along with slight differences in compression from the pressure applied during the electrode assembly. The Tafel slopes shown in table II are those derived from a fit of the Tafel equation to the polarization data for each case of air or oxygen at the various loadings.

Table II. Experimental values

Experimental Values	S1		S2		S3	
Temperature of operation [°C]	250		250		250	
Dew Point [°C]	75		75		75	
Mean porosity	50%		50%		50%	
Catalyst layer thickness [μm]	44+/-9		84+/-5		148+/-4	
Metal loading [mg/cm^2]	1.75		3.5		7	
	Air	O2	Air	O2	Air	O2
Catalyst Layer Resistance [Ωcm^2]	0.232	0.231	0.225	0.227	0.200	0.199
OCV	0.980	1.011	0.988	1.015	0.990	1.021
Limiting current [A/cm^2]	1.19	1.62	1.36	1.92	1.41	2.15
Tafel Slope [mV/dec]	209.5	206.5	211.7	203.3	200.5	221

The OCV is a function of the temperature and pressure variation. For our system at 250°C the OCV is equal to 1.12V which is equivalent to the reversible potential for the oxygen reduction reaction calculated as:

$$E_{rev}(T,P) = E_0(T) + \frac{RT}{2F} ln\left(\frac{\alpha\beta^{1/2}}{\lambda}\right) + \frac{RT}{2F} ln\left(P_{O_2}^{1/2}\right) \quad [12]$$

$$E_0(T) = -\frac{\Delta G^0(T)}{nF} = -\frac{\sum_i \nu_i \left(\bar{g}_{f,i}^0 - \Delta H(T) - T\Delta S(T)\right)_i}{nF} \quad [13]$$

$$E_0(T) = -\frac{\Delta G^0(T)}{nF} = -\frac{-217934.68}{2\times 96485} = \mathbf{1.13V} \quad [14]$$

Where E_0 represents the standard voltage for oxygen. $\bar{g}_{f,i}^0$, is the Gibbs formation energy of the i compound, ν_i the stoichiometry coefficients. α, β, λ represent the molar fraction of hydrogen, oxygen and water respectively. The molar fraction of the reactants is close to one, based on the high stoichiometry imposed by the fixed reactant flow rates of 40 sccm and 75 sccm for hydrogen and air/oxygen, respectively. The second term in equation 12 vanishes so we find the OCV from equation 12[16]:

$$OCV_{O_2} = E_0(T) + \frac{RT}{zF} ln\left(\frac{P_{H_2} P_{O_2}^{\frac{1}{2}}}{P_{H_2O}}\right) = \mathbf{1.12V} \quad [15]$$

To calculate the expected variation in OCV when we switch from oxygen to air, for the same hydrogen and relative humidity, equation 13 is reorganized to express the OCV as:

$$\Delta OCV = \frac{RT}{4F} ln\left(\frac{p_{O_2}}{p_{O_{2,air}}}\right) \approx \mathbf{0.018V} \quad [16]$$

$$OCV_{Air} = OCV_{O_2} - \Delta OCV = \mathbf{1.11V} \quad [17]$$

The observed OCV values obtained for air are within approximately 1% of those calculated. We also note that the water production relative to that carried into the cell in the gas stream is always smaller.

SAFC polarization curves do not exhibit a sharp limiting current, indicating that the slow mass transport in this system does not lead to reactant 'starvation' under the test conditions. The observed maximum current values decrease as a combination of oxygen concentration depletion and catalyst thickness increase.

Sensitivity analysis

Understanding the parameter sensitivity of our model is a key step in developing a base case for fitting to our experimental data. First, we calculated and selected the experimental Tafel slopes from log I vs. potential plot (table II). Then, using this value, we modified one parameter at a time per simulation to find the base case values as table III summarizes. Finally, the effects of varying each parameter individually are illustrated in Figures 44-46. In this preliminary step, we are seeking to define a range of each parameter value in which the model will converge and yield qualitatively reasonable behavior.

Figure 44 illustrates the sensitivity to the permeability parameter (DC) in air for each loading. The values yield satisfactory results over a specific range. For small values of DC, the simulations do not converge or the maximum current obtained is unrealistic. Permeability values (DC) modified the diffusion current obtained as equation 4 states. If the diffusion current is small (red lines in Figure 46), equation 3 is multiplied by a high order of magnitude constant, causing convergence under unrealistic conditions. When the diffusion current is higher than the maximum current, the calculation does not converge due to negative concentration values when equation 3 is solved. In summary of this effect, the permeability values modify the diffusion current behavior, making the model convergence sensitive to the selection of this parameter.

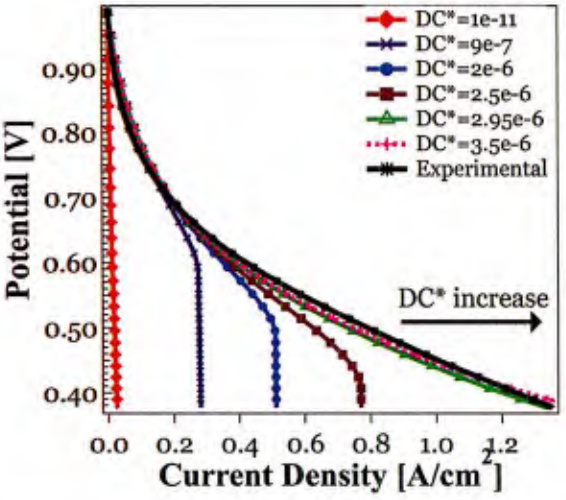

Figure 44 Active area sensitivity in air. Loading: 3.5 mg/cm^2 Pt. Tafel slope: 207 mv/dec.

Table III. Base case parameters

Parameter	Air	O_2
Roughness modified current density - $A_r i_0$ (A/cm^2)	25mg: $0.42*10^{-4}$ 50mg: $0.42*10^{-4}$ 100mg: $0.42*10^{-4}$	25mg: $0.42*10^{-4}$ 50mg: $0.42*10^{-4}$ 100mg: $0.42*10^{-4}$
Permeability – DC* (mol/cm-s-atm)	25mg: $2.9*10^{-6}$ 50mg: $2.9*10^{-6}$ 100mg: $2.9*10^{-6}$	25mg: $2.9*10^{-6}$ 50mg: $2.9*10^{-6}$ 100mg: $2.9*10^{-6}$
Tafel slope (mv/dec)	25mg: 209.5 50mg: 211.7 100mg: 200.5	25mg: 206.5 50mg: 202.6 100mg: 220.1
Limiting Current (mv/dec)	25mg: 1.2 50mg: 1.2 100mg: 1.2	25mg: 1.2 50mg: 1.2 100mg: 1.2

Figure 45 represents the model sensitivity to the RCCD term, $A_r i_0$, for each loading. The model will converge for any value of $A_r i_0$ lower than 1. This parameter is represented in equation 2 as the prefactor of the exponential kinetic behavior. It does not affect convergence unless the value reaches a point where the boundary conditions, equations 5 and 6, are not satisfied. In this case, the end of the dashed lane in Figure 45 represents the boundary condition satisfaction. The active area is not a sensitive parameter for model convergence but is critical to understanding the catalyst utilization within the layer and therefore it must be chosen within a rational range.

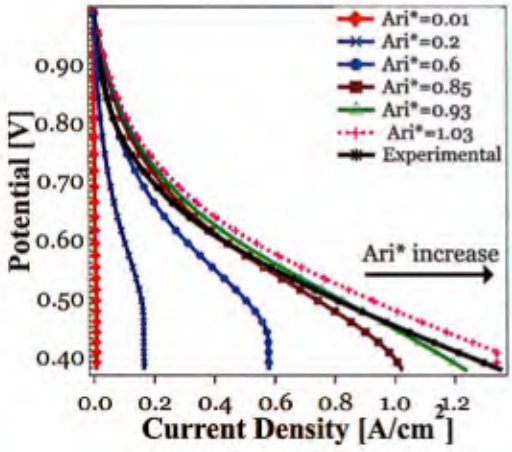

Figure 45 Permeability sensitivity values DC* = $1*10^{-11}$, $9*10^{-7}$, $2*10^{-6}$ - $7*10^{-6}$ [mol/cm-s-atm] Loading: 3.5 mg/cm^2 Pt. Tafel slope: 207 mv/dec.

Figure 46 shows the effect of varying limiting current (I_{lim}). As discussed above, SAFCs do not show the sharp decay typically found in mass transport limited systems. In our case, limiting current values are used to calculated the diffusion current and thus influence the concentration distribution within the catalyst layer. To obtain convergence, the value must be close to the maximum current. Otherwise the calculation does not converge. This parameter is remarkably sensitive because the range of variation has to be less than 2% to be within the convergence range. However, this is not a fitting parameter but rather provides a method to estimate the limiting current, which cannot be directly extracted from the polarization curve. Once the value is set, no further optimization is required.

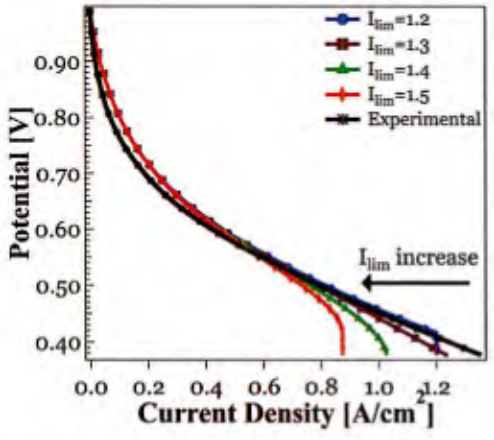

Figure 16 Limiting current sensitivity in airLoading: 3.5 mg/cm^2 Pt. Tafel slope: 207 mv/dec.

Modeling analysis

The sensitivity analysis provides a set of base case parameters to initialize the simulation, as shown in table III. We then performed a fit of the polarization curves by using finite differences and optimization tools within Matlab. Figure 47 illustrates the polarization curves fitting for the different loadings with a 97% of confidence for all of them. Table IV summarizes the main fitted and optimized parameters obtained from different configurations operating on air and oxygen. Once the values are defined, the model determines the RMS fit to calculate Tafel slopes, cathodic overpotential and polarization curve values.

Table IV. Optimized parameters

Parameter	Air	O_2
Roughness modified current density - $A_r i_o$ (A/cm^2)	25mg: $7.2*10^{-6}$	25mg: $1.60*10^{-6}$
	50mg: $7.4*10^{-6}$	50mg: $1.79*10^{-6}$
	100mg: $7.5*10^{-6}$	100mg: $2.18*10^{-6}$
Permeability – DC* (mol/cm-s-atm)	25mg: $5.53*10^{-7}$	25mg: $2.1*10^{-6}$
	50mg: $3.01*10^{-7}$	50mg: $1.97*10^{-6}$
	100mg: $7.58*10^{-7}$	100mg: $2.36*10^{-6}$
Tafel slope (mv/dec)	25mg: 200.5	25mg: 201.0
	50mg: 207	50mg: 202.6
	100mg: 212	100mg: 210.9

Figure 47 shows the fitted polarization curves. In general, the fits are excellent. Comparing air vs. oxygen curves, the performance decreases around 30% with oxygen dilution. The OCV is higher with pure oxygen as a result of the OCV dependence on oxygen partial pressure and it is also higher with higher loading. Moreover, the current decrease between air and oxygen is more severe at higher loadings. These phenomena are consequences of the significant additional mass transport limitations in the air case, especially through a thick catalyst layer with modest porosity.

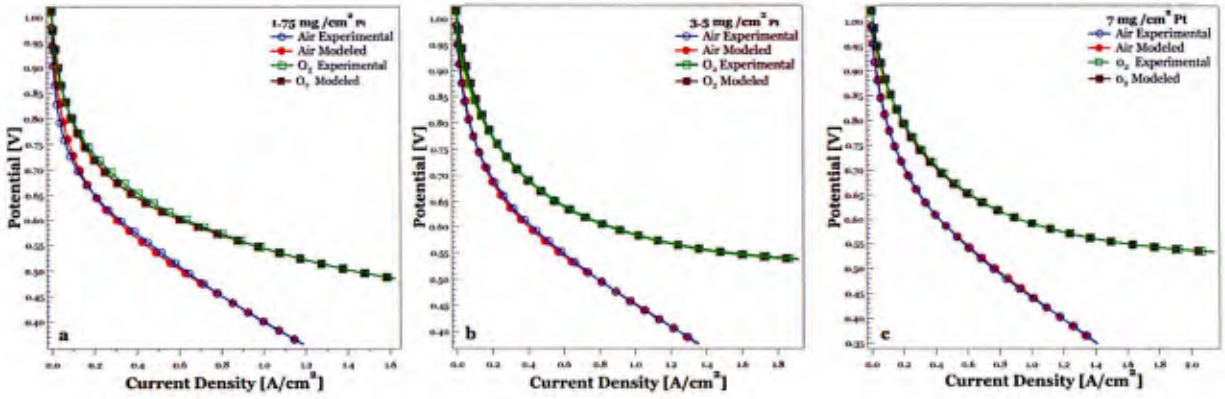

Figure 47 Polarization curves fitting for air and oxygen at different loadings. a) 1.75 mg/cm² b) 3.5 mg/cm² c) 7mg/cm²

The Tafel slopes obtained are summarized in Table IV. In both cases, the standard deviation is lower than 3mv/dec, so we can conclude that the kinetic parameters can be considered constant. These Tafel results are in agreement with those calculated at this temperature assuming a rate-limiting step with 1 e- and α of 0.5. The limited variation of the Tafel slope values from the base parameters suggests that the Tafel slope values determined initially would suffice to capture the catalysis behavior.

Figure 48 illustrates the RCCD behavior compared to that calculated by Springer et. al for Pt at 80°C. The RCCD factor is the product of a term that corrects the geometric area to yield the real active area (A_r) and a current density term. RCCD plays the role of the i_o in a Butler-Volmer analysis. As has been discussed, the determination of a true value of i_o for the ORR is difficult because the state fo the Pt surface changes (between a bare and oxidized surface) as one extrapolates toward zero overpotential, the conventional way to determine i_o. Gottesfeld and Springer have suggested using $i_{0.9V}$ as a proxy for i_o. In our case, much less can be inferred regarding the ORR nor can we truly estimate the true surface area (e.g. from a hydrogen adsorption peak) and thus we do not try to separate these parameters. For each condition (O_2 vs, air) the values are approximately constant, and the ratio of the values obtained from the fits of curves from cells operating on air and oxygen differs by a factor of roughly 2.5. This term is in essence a reflection of the kinetics of the ORR. Inspection of the sensitivity analysis for this parameter (Figure 44) shows that the RCCD term has a strong influence. The fits shown are quite sensitive to the parameter, with implications throughout the curve. From this we conclude that this is a critical parameter for cell operation. Also, we should note that the observed parameters are

substantially lower in value than the corresponding term in the Springer model, which was based on data acquired at 80°C. (See below for a discussion of this point.)

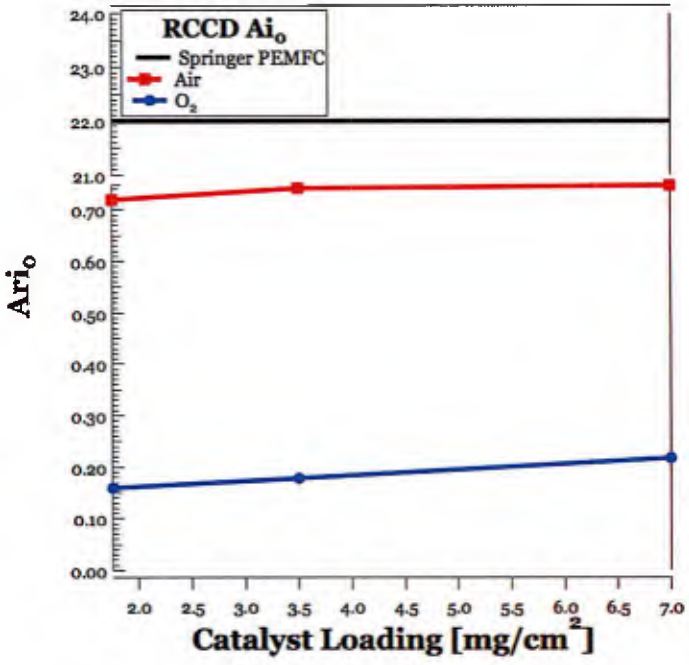

Figure 48. Calculated RCCD for different loadings

Table IV shows the permeability (DC) values, which are fairly similar for a given gas. The difference in values between air and oxygen for the SAFC fits is roughly a factor of 4 on average and is therefore likely to be a direct consequence of the difference in concentration of the gas being transported (O_2 vs air) across the catalyst layer. Note that the difference is slightly less than the theoretical factor of 5, perhaps reflecting effects of porosity on mass transport. Compared with PEM Fuel Cells, the permeability values are significantly higher due to the high diffusion rates at high temperature.

Figure 49 shows the calculated distribution of local current density across the catalyst layer at different voltages (0.6V, 07V, 0.8V) for oxygen and air. The behavior presented for the oxygen case (Figure 49a, 49c and 49e) and the air case (Figure 49b, 49d and 49f). The reaction rates for oxygen are roughly two times higher than those for air at every potential due to higher reactant concentration. Moreover, the air case shows a limiting situation with respect to gas transport, indicated by the inflections in the curves, as the local current density drops close to the CL/membrane interface (x=1). The modeling results show decay in current density near this

boundary as consequence of the interplay between charge and reactant transport through the catalyst layer. The non-uniformity of the current density profile throughout the catalyst layer suggests that the transport is an important factor at all voltages probed. This is even the case for oxygen-fed cathodes. As we increase the loadings, the conversion at higher overpotential seems to become less homogenous across the layer. This is consistent with strong mass transport control, increasing with thicker layers.

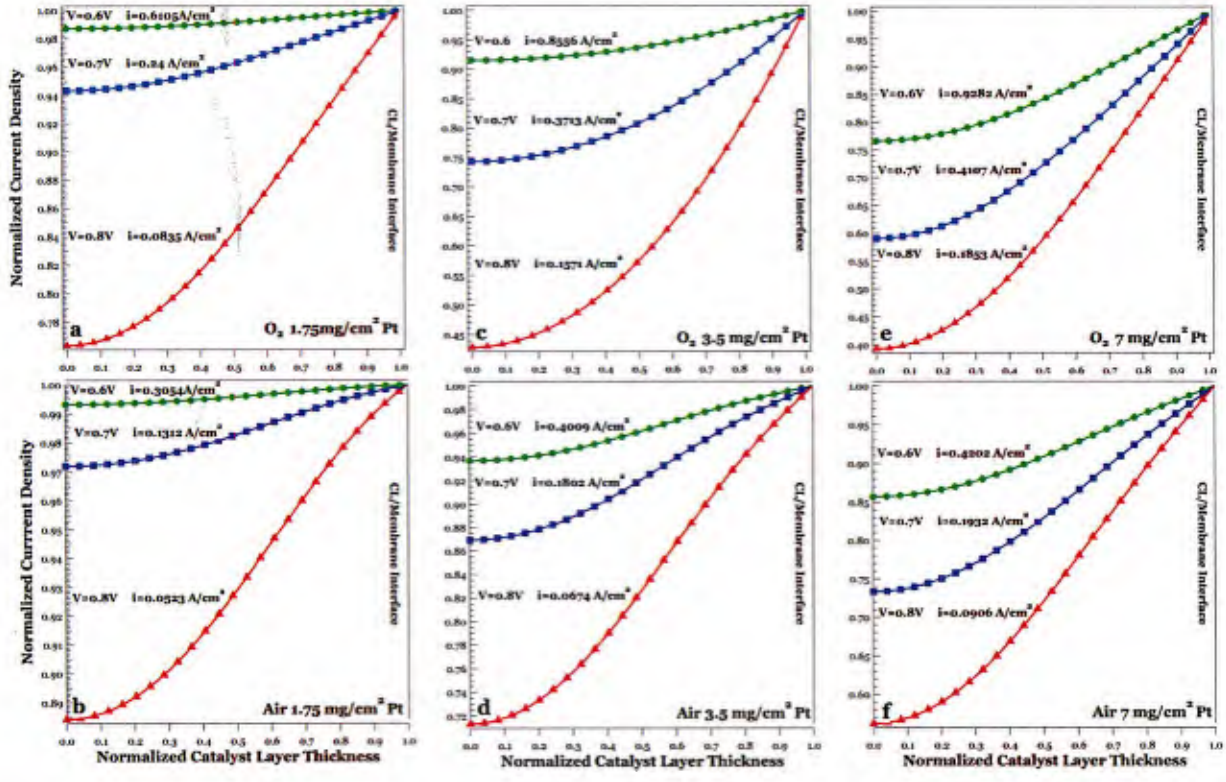

Figure 49. Normalized oxygen current distribution at different potential values V=0.8, 0.7 and 0.6V a) 1.75 mg/cm^2 O_2 b) 1.75 mg/cm^2 Air c) 3.5 mg/cm^2 O_2 d) 3.5 mg/cm^2 Air e) 7 mg/cm^2 O_2 f) 7 mg/cm^2 Air.

Overpotential analysis. Based on the fitted parameters and the current distribution we calculated the losses to verify the validity of our arguments in terms of transport and charge transfer within the catalyst layer as well as kinetic behavior. The cell potential is calculated as[16]:

$$E_{cell} = E_{rev}(p_{H_2}, p_{O_2}, T) - \eta_{act} - \eta_{ohm} - \eta_{con} \qquad [18]$$

Where $E_{rev}(p_{H_2}, p_{O_2}, T)$, represents the reversible electrode potential at the temperature and operation pressure and is calculated with equation 12. η_{act}, represents the activation

overpotential and can be calculated with equation 8 for ORR due to its sluggish kinetics compare with hydrogen. η_{ohm}, is the ohmic overpotential associated with the catalyst layer resistance and can be calculated as:

$$\eta_{ohm,i} = iR_i \qquad [19]$$

R_i, represents the MEA resistance obtained from the in-situ measurements. These values are tabulated in table II. η_{con} represents the mass transfer overpotential, which can be calculated from equation 18.

Figure 50 graphically shows the contribution of the various overpotential loss terms to the polarization curves. Blue, green and grey areas represent the concentration, ohmic and activation polarization respectively. For convenience, we also extract values of the overpotentials at several current density values for the various cases, tabulated in table V.

Table V. Activation, Ohmic and Concentration overpotentials at i≅0.2 A/cm²

Loading [mg/cm²]	Thickness [μm]	η_{act} [mV]		η_{ohm} [mV]		η_{mt} [mV]	
		Air	O2	Air	O2	Air	O2
1.75	44	205.15	235.87	60.31	59.99	250.94	158.85
		39.7%	51.9%	11.7%	13.2%	48.6%	34.9%
3.5	84	211.33	235.80	56.06	56.19	203.18	114.11
		44.9%	58.1%	11.9%	13.8%	43.2%	28.1%
7	148	216.02	240.90	49.51	49.53	184.31	87.37
		48.0%	63.8%	11.0%	13.1%	41.0%	23.1%

Based on Figure 8 and table V, we can draw a few basic conclusions. For all cases, there is substantial mass transfer loss even at modest current density. Remarkably, even at 200 mA/cm², mass transport losses are the major polarization source for air systems with values higher than 40% as table V illustrates. For oxygen systems, the main source is the activation losses with values higher than 50% and the mass transport losses represent the second larger losses with a contribution higher than 23%.

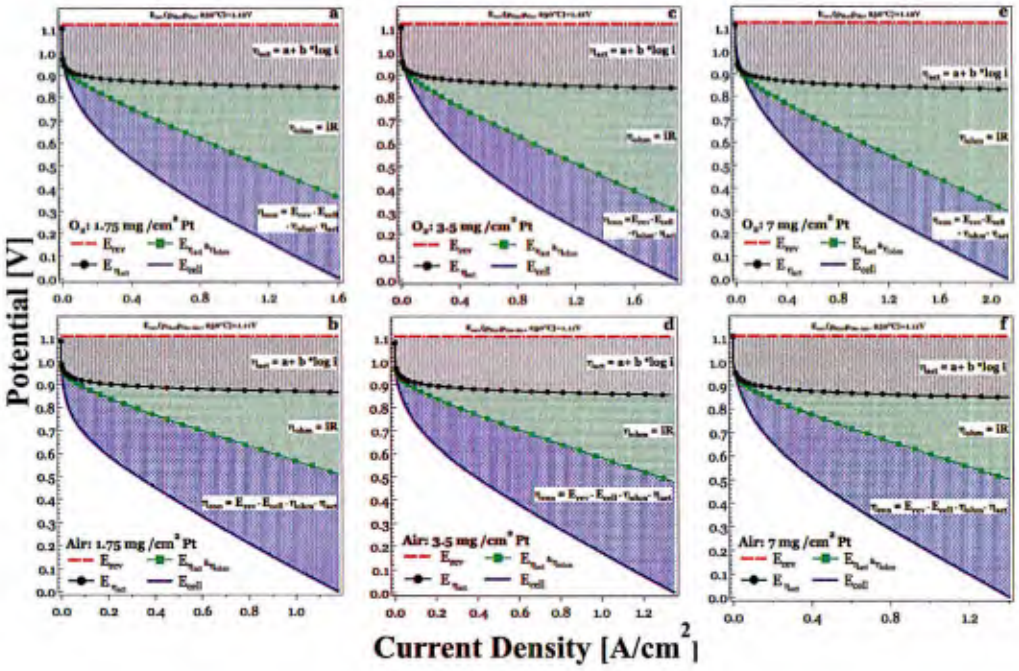

Figure 50: 8 Polarization curves with activation and ohmic overpotentials calculation from optimized Tafel parameters a) 1.75 mg/cm² O_2 b) 1.75 mg/cm² Air c) 3.5 mg/cm² O_2 d) 3.5 mg/cm² Air e) 7 mg/cm² O_2 f) 7 mg/cm² Air g) Activation, Ohmic and Concentration Overpotentials at i≅0.2 (PEMFC values from Arisetty et. Al [17])

The large contribution from mass transport losses is somewhat expected due to the large catalyst layer thickness relative to its low temperature counterparts. Moreover, it is higher as a proportion of limiting current for air as a consequence of the mass transport effects discussed above. The catalyst layer thickness and limited accessible area negates the benefits of larger diffusion coefficients at higher temperatures. Ohmic losses and activation are bigger in the oxygen case as a consequence of the higher current densities obtained in comparison with the air systems.

SAFC activation losses decrease with higher temperatures, in contrast with the PEM counterparts based on the work from Arisetty and collaborators [17]. For our system, the activation overpotential is reduced 35% as a direct consequence of faster kinetics enhanced with temperature. Ohmic losses are six times and mass transfer losses are two hundred times bigger than for PEM in air at 80°C. Therefore, the presence of large ohmic and mass transfer losses at lower current densities points toward. decreasing catalyst layer thickness and improved microstructural configuration as targets for SAFCs performance improvement.

It is instructive to compare the physical parameters emerging from the model of the SAFC system to corresponding results in PEMFC systems. The difference in Tafel slope values, as noted above, reflects the temperature change between the two technologies. One striking difference is the much lower value of the $A_r i_0$ in the SAFC relative to that calculated by Springer et al. In our judgment, both area and current density terms contribute to this difference. In an SAFC, the available active catalyst surface is the perimeter circumscribed by the Pt contact at an air-CDP interface. This is a key limitation of the catalyst layer design used in this work. It is reasonable to assume that the available surface area is a small fraction of that expected based on fully divided nanoparticles of Pt. In spite of the high loading of Pt, the occlusion of the surface by CDP leads to much lower effective surface area contributing to the 'roughness' term, i.e. the ratio of real to geometric area. It is perhaps surprising to think that i_0, the exchange current density 'proxy,' could be lower at the substantially higher temperature. However, it should be kept in mind that the rate-limiting step for the ORR likely includes the initial chemisorption of oxygen. This is a rather weak process and is therefore significantly less favorable at the elevated temperature of the SAFC. Indeed, even hydrogen chemisorption can be difficult to observe under SAFC conditions.

In this study we developed and evaluated a macrohomogeneous model of SAFCs, Through several steps, we obtained excellent fits with errors less than 3%. This demonstrates that our methodology of linking quality experimental data and simultaneous fitting can lead to useful information about the physical parameters of the system and allow us to use model predictions to better understand polarization phenomena. We calculated the polarization phenomena in solid acid fuel cells in successive steps. This modeling study provides us with a basis for considering cells employing Pt coated CDP particles in the catalyst layers. Sensitivity Analysis provided us with a suitable set of initial parameters to enhance agreement between experimental and modeled data. Moreover, it shows us that permeability and limiting current selection are crucial to describe our system. Active area is not as sensitive, but its values must be selected properly to be able to describe the phenomena inside the cathode. OCV and Tafel results are in agreement with the theoretical values, which validates our kinetics argument to describe the model and the necessity of robust experimental design to feed the model. The limiting processes in SAFC performance arise from limitations in available surface area and the difficulty of mass transport to this surface.

Permeability values shown here are higher than for a low temperature counterpart as a

result of higher diffusion coefficients as a consequence of temperature increased. The difference between air and oxygen is directly related to the concentration depletion and mass transport effects. We introduced the RCCD factor as a key operation parameter that corrects the geometric area to yield the real active area (Ar) and with a current density term. We did not attempt to separate Ari* mainly because of the unknown Pt surface structural changes (between a bare and oxidized surface) when extrapolating Tafel plots toward zero overpotential. Low values of this parameter reflect a decrease in the accessible electrochemically active area most likely due to the constraints of the SAFC electrode architecture employed, in which the impermeable CDP coats much of the catalyst.

Concentration polarization losses in SAFCs represent the major polarization source when operating on air across the entire current density range. Activation losses represent a major source of loss in oxygen, but mass transfer is also important. Thus, we conclude that in order to improve performance and be competitive against its low temperature counterparts, we need to decrease the thickness and improve the microstructural configuration of the catalyst layer.

References

[1] Haile, S.M., et al., *Solid acid proton conductors: from laboratory curiosities to fuel cell electrolytes.* Faraday Discussions, 2007. 134(0): p. 17-39.

[2] Papandrew, A.B., et al., *Ruthenium as a CO-tolerant hydrogen oxidation catalyst for solid acid fuel cells.* Journal of Materials Chemistry A, 2015. 3(7): p. 3984-3987.

[3] Papandrew, A.B., et al., *Electrochemical Hydrogen Separation via Solid Acid Membranes.* Journal of The Electrochemical Society, 2014. 161(5): p. F679-F685.

[4] C.RI Chisholm, D.B., AB Papandrew, SK Zecevic, SY Cha, KA Sasaki, A Varga, KP Glapis, SM Haile, *From Laboratory Breakthrough to Technological Realization: The Development Path for Solid Acid Fuel Cells.* The Electrochemical Society interface, 2009. 18(3): p. 53 - 59.

[5] Weber, A.Z. and J. Newman, *Modeling Transport in Polymer-Electrolyte Fuel Cells.* Chemical Reviews, 2004. 104(10): p. 4679-4726.

[6] Gasteiger, H.A., et al., *Activity benchmarks and requirements for Pt, Pt-alloy, and non-Pt oxygen reduction catalysts for PEMFCs.* Applied Catalysis B: Environmental, 2005. 56(1–2): p. 9-35.

[7] Stephens, I.E.L., et al., *Understanding the electrocatalysis of oxygen reduction on platinum and its alloys.* Energy & Environmental Science, 2012. 5(5): p. 6744-6762.

[8] Springer, T.E., M.S. Wilson, and S. Gottesfeld, *Modeling and Experimental Diagnostics in Polymer Electrolyte Fuel Cells.* Journal of The Electrochemical Society, 1993. 140(12): p. 3513-3526.

[9] Springer, T.E., T.A. Zawodzinski, and S. Gottesfeld, *Polymer Electrolyte Fuel Cell Model.* Journal of The Electrochemical Society, 1991. 138(8): p. 2334-2342.

[10] Bear, J. and Y. Bachmat, *Transport Phenomena in Porous Media — Basic Equations*, in *Fundamentals of Transport Phenomena in Porous Media*, J. Bear and M.Y. Corapcioglu, Editors. 1984, Springer Netherlands: Dordrecht. p. 3-61.

[11] Choy, T.C., *Chapter 1. Essentials*, in *Effective Medium Theory : Principles and Applications*. 1999, Oxford Science Publications. p. 10-23.
[12] Mann, H.B. and D.R. Whitney, *On a Test of Whether one of Two Random Variables is Stochastically Larger than the Other.* The Annals of Mathematical Statistics, 1947. 18(1): p. 50-60.
[13] Pratt, J.W., *Concepts of Nonparametric Theory*, J.D. Gibbons and SpringerLink, Editors. 1981, New York, NY : Springer New York. p. 318-336.
[14] Papandrew, A.B., et al., *Activity and Evolution of Vapor Deposited Pt-Pd Oxygen Reduction Catalysts for Solid Acid Fuel Cells.* Journal of The Electrochemical Society, 2013. 160(2): p. F175-F182.
[15] Papandrew, A.B., et al., *Advanced Electrodes for Solid Acid Fuel Cells by Platinum Deposition on CsH2PO4.* Chemistry of Materials, 2011. 23(7): p. 1659-1667.
[16] Bard, A.J. and L.R. Faulkner, *Electrochemical Methods: fundamentals and applications*. Second ed. 2001: John Wiley & Sons, Inc.
[17 Arisetty, S., et al., *Effect of Platinum Loading on Catalyst Stability under Cyclic Potentials.* ECS Transactions, 2011. 41(1): p. 797-809.

Primary Personnel

Name	Position
Nelly Cantillo	Graduate Student
Brian Fane	Graduate Student
Diana Orozco	Graduate Student
Zhijiang Tang	Graduate Student
Gabriel Goenaga	Senior Scientist
Ramez Elgammal	Senior Scientist
Shane Foister	Senior Scientist